ARSENIC UPTAKE AND SPECIATION

IN SELECTED SULFATE AND PHOSPHATE MINERALS

A Thesis Submitted to the College of Graduate Studies and Research

in Partial Fulfillment of the Requirements for the Degree of Doctor of Philosophy

in the Department of Geological Sciences

University of Saskatchewan

Saskatoon

by

Jinru Lin

2014

Permission to use

In presenting this thesis in partial fulfillment of the requirements for a Postgraduate degree in Science from the University of Saskatchewan, I agree that the Libraries of this University may make it freely available for inspection. I further agree that permission for copying of this thesis in any manner, in whole or in part, for scholarly purposes may be granted by the professors who supervised my thesis work, or, in their absence, by the Head of the Department of Geological Sciences or the Dean of the College of Graduate Studies and Research, in which my thesis work was done. It is understood that any copying or publication or use of this thesis or parts thereof for financial gain shall not be allowed without my written permission. It is also understood that due recognition shall be given to me and to the University of Saskatchewan in any scholarly use which may be made of any material in my thesis.

Request for permission to copy or to make other use of material in this thesis, in whole or in part, should be address to:

Head of the Department of Geological Sciences

University of Saskatchewan

114 Science Place

Saskatoon, Saskatchewan,

S7N 5E2 CANADA

Abstract

Widespread arsenic contamination with adverse effects to human health is a global problem. Most previous studies on arsenic contamination in natural environments and those associated with mining and agricultural activities focused largely on arsenic-rich minerals such as arsenates, arsenites, sulfarsenides, and sulfides. Rock-forming minerals generally contain only minor or trace amounts of arsenic but, owing to their sheer abundances, are potentially important (and sometimes dominant) sources of this metalloid and can play significant roles in the attenuation and sequestration of arsenic in various environments. However, there remains a significant gap in my knowledge about the uptake and speciation of arsenic in rock-forming minerals. This thesis research is intended to bridge this gap by investigating the uptake and speciation of arsenic in selected rock-forming sulfate and phosphate minerals (i.e., gypsum, struvite and newberyite).

Gypsum ($CaSO_4 \bullet 2H_2O$) is a major by-product of mining and milling processes of borate, phosphate and uranium deposits worldwide and, therefore, potentially plays an important role in the stability and bioavailability of heavy metalloids, including As, in tailings and surrounding areas. Gypsum containing 1,900 and 185 ppm As, synthesized with $Na_2HAsO_4 \bullet 7H_2O$ and $NaAsO_2$ in the starting materials, respectively, has been investigated by synchrotron X-ray absorption spectroscopy (XAS), single-crystal electron paramagnetic resonance spectroscopy (EPR), and pulsed electron nuclear double resonance spectroscopy (ENDOR). Quantitative analyses of As K edge X-ray absorption near edge structure (XANES) and extended X-ray absorption fine structure (EXAFS) spectra show that arsenic occurs in both +3 and +5 oxidation states and the As^{3+}/As^{5+} value varies from 0.35 to 0.79. Single-crystal EPR spectra of gamma-ray-irradiated gypsum reveal two types of arsenic-associated oxyradicals: $[AsO_3]^{2-}$ and an $[AsO_2]^{2-}$. The $[AsO_3]^{2-}$ center is characterized by principal ^{75}As hyperfine coupling constants of A_1 = 1952.0(2) MHz, A_2 = 1492.6(2) MHz and A_3 = 1488.7(2) MHz, with the unique A axis along the S-O1 bond direction, and contains complex ^{1}H superhyperfine structures that have been determined by pulsed ENDOR. These results suggest that the $[AsO_3]^{2-}$ center formed from electron trapping on the central As^{5+} ion of a substitutional $(AsO_4)^{3-}$ group after removal of an O1 atom. The $[AsO_2]^{2-}$ center is characterized by its unique A(^{75}As) axis approximately perpendicular to the O1-S-O2 plane and the A_2 axis along the S-O2 bond direction, consistent

with electron trapping on the central As^{3+} ion of a substitutional $(AsO_3)^{3-}$ group after removal of an O2 atom. These results confirm lattice-bound As^{5+} and As^{3+} in gypsum and point to potential application of this mineral for immobilization and removal of arsenic pollution. EPR spectra show that another sulfate boussingaultite is also sequestering both As^{5+} and As^{3+} at its S site. Synthesis experiments at pH from 2 to 14 also show that arsenic uptake in gypsum is pH dependent.

Struvite and newberyite, common biominerals and increasingly important green fertilizers recovered from wastewater treatment plants, are capable of sequestering a wide range of heavy metals and metalloids, including arsenic. Inductively coupled plasma mass spectrometric (ICPMS) analyses show that struvite formed under ambient conditions contains up to 547±15 ppm As and that the uptake of As is controlled by pH. Synchrotron As K-edge XANES spectra measured at 20 K show that As^{5+} is the predominant oxidation state in struvite, irrespective of $Na_2HAsO_4{\cdot}7H_2O$ or $NaAsO_2$ as the source for As. Modeling of As K-edge EXAFS data suggest that local structural distortion associated with the substitution of As^{5+} for P^{5+} in struvite reaches up to 3.75 Å. Single-crystal electron paramagnetic resonance (EPR) spectra of gamma-ray-irradiated struvite disclose five $[AsO_3]^{2-}$ radicals and one $[AsO_4]^{2-}$ radical. These arsenic-centered oxyradicals are all readily attributed to form from diamagnetic $[AsO_4]^{3-}$ precursors during irradiation, providing further support for exclusive incorporation and local structural expansion beyond the first shell of As^{5+} at the P site in struvite.

Arsenic doped newberyite ($MgHPO_4{\cdot}3H_2O$) obtained from the gel diffusion method has investigated by synchrotron XAS at the As K-edge (11,867 eV) at 8 K and single-crystal EPR spectroscopy at room temperature. XANES data show that As^{5+} is dominant and EXAFS analysis reveals a local environment typical of the arsenate species as well. Single-crystal EPR spectra of gamma-ray-irradiated newberyite contain two arsenic-associated oxyradicals: $[AsO_3]^{2-}$ and $[AsO_2]^{2-}$ derived from As^{5+} and As^{3+}, respectively, at the P site in the newberyite structure. Elevated concentrations of arsenic have also been observed in natural newberyite from guano deposits and reflect the accumulation of this metalloid in the food chain. Therefore, struvite and newberyite can both sequester significant amounts of arsenic, and their direct use as fertilizers (irrespective of origins from guano deposits or wastewaters) is a potential source of arsenic contamination. On the other hand, the capacities of struvite and newberyite for accommodating

significant amounts of arsenic in crystal lattices coupled with their simple chemistry and crystallization under ambient conditions make them attractive materials for immobilization and removal of arsenic contamination in aqueous environments.

Acknowledgements

First and foremost, I would like to express my deepest gratitude to my supervisor Dr. Yuanming Pan for his continuous support and great guidance during my graduate study. I am grateful for his scientific expertise, insightful advice, and outstanding mentorship during all phases of this Ph.D. degree. I would not have made it through this process without his guidance.

I am immensely thankful to Dr. Ning Chen since he has given me so much help in my study and work. His help and support greatly helped to shape up this research project. I am deeply thankful to the members of my supervisory committee Drs. Chris Hawkes, Tom Kotzer Chris Weisener, and Jim Merriam.

Also, I would like to express my gratitude to Tom Bonli, Jim Rosen, Blane Novakovski, Jianzhong Fan, Ngat Mee Choo and Sammynaiken Ramaswami, who provide analytical assistances as well as a friendly and cooperative work environment during my research.

I would like to thank Rong Li and Dr. Zucheng Li for the help in my study and I wish to thank my family members and friends for their support and encouragement. They have always been there for me.

Finally, I gratefully acknowledge the Natural Science and Engineering Research Council (NSERC) of Canada for financial support through research grants to Dr. Yuanming Pan. My study is also supported by the Dr. Rui Feng Geological Sciences Award from the University of Saskatchewan.

TABLE OF CONTENTS

List of Tables

List of Figures

CHAPTER 1
Introduction

1.1 Background

The element arsenic (As), is of concern due to its high toxicity forming a number of poisonous compounds and wide distribution throughout the Earth's crust and ground water (Drahota and Filippi, 2009; Smedley and Kinniburgh, 2002; Bowell and Parshley, 2001). Specifically, arsenic contamination of ground water has been characterized as one of the major threats to human health, reportedly responsible for lung and skin cancers and so on (Bates et al., 1992; Berg et al., 2001; Chakraborti et al., 2004; Chen et al., 1992; Chen et al., 1988; Chen et al., 2007). The accepted level for maximum concentration of arsenic as defined by World Health Organization (WHO) drinking water guideline in safe drinking water is 10 ppb (0.01 mg/L) (WHO, 2001). However, severe drinking water problems with concentration of arsenic exceeding the guideline have affected millions of people in many countries throughout the world, including Bangladesh, India, China, Canada, Australia, United States, and several other countries (Ashley and Lottermoser, 1999; Guillot and Charlet, 2007; Rahman et al., 2009; Smith et al., 2000; Ujevic et al., 2010; Wang and Mulligan, 2006; Welch et al., 1988).

The occurrence of arsenic contamination derives from both natural geological processes and anthropogenic influences. Most environmental arsenic problems are associated with mobilization under natural conditions. The primary arsenic contamination derives naturally from the locations, such as Bangladesh and West Bengal, where the dissolution or desorption of arsenic-bearing rocks (e.g., arsenic-bearing sulfide minerals, arsenic-rich iron oxyhydroxides) occurs (Smedley and Kinniburgh, 2002; Garelick et al., 2009; Ravenscroft et al., 2005; Welch et al., 1988; Das et al., 1996). Nevertheless, a variety of human activities (e.g., mining, agriculture) are believed to have an important impact on the mobilization and elevation of arsenic concentrations to levels of concern in some areas (Wang and Mulligan, 2006; Ashley and Lottermoser, 1999; Camm et al., 2004; Foster et al., 2010; Garelick et al., 2008; Bhattacharya et al., 2007; Arslan et al., 1999). Mining, in particular, introduces the most significant amount of arsenic in associated areas. For example, high concentration of arsenic reaching up to 3000 mg/L in ground water samples was

observed in the borate mines at the Bigadiç borate deposits (Western Turkey) (Gemici et al., 2008) and approximately 3.5 tons of fluvial input of arsenic annually is found in Moira Lake, Ontario, resulting from local gold-mining and mineral processing (Azcue and Nriagu, 1995). Similarly, at the Key Lake uranium mine, Saskatchewan, arsenic concentration up to 10,000 mg/L has been observed in raffinate (Donahue and Hendry, 2003).

In the natural environment, arsenic exists in several oxidation states including the -3, 0, +1, +3 and +5 valences forming as inorganic and organic compounds (Welch et al., 1988). However, in natural waters, dissolved trivalent arsenite [As(III)] and pentavalent arsenate [As(V)] are predominant (Smedley and Kinniburgh, 2002). The forms of arsenic are dependent on pH and redox potential (Eh). Generally, arsenic in ground water is present as an oxyanion, such as arsenate (AsO_4^{3-}, $HAsO_4^{2-}$ and $H_2AsO_4^-$) or arsenite ($As(OH)_3$, $As(OH)_4^-$, $AsO_2(OH)^{2-}$ and AsO_3^{3-}), or both. As(V) usually dominates under oxidizing conditions, and As(III) is stable at intermediate to reducing conditions (Smedley and Kinniburgh, 2002).

In natural systems, the mobility and distribution of arsenic species are largely controlled by adsorption on and incorporation in mineral phases. Thus, attention has been paid to adsorption and incorporation reactions between arsenic and minerals. Surface adsorption and incorporation with common minerals can reduce the leachate concentration of arsenic and increase the possibility in controlling the bioavailability and mobilization of arsenic in the environment, but due to the similar geometry between phosphate, sulfate and arsenate, more detailed mechanisms regulating replacement remain largely obscure for sulfate and phosphate minerals, in particular, which are known to be abundant in the Earth' crust and contain certain non-negligible amount of arsenic (Smedley and Kinniburgh, 2002).

(1) Arsenic and sulfate minerals

Sulfate minerals are ubiquitous in many arsenic contaminated aquifers including common minerals such as schwertmannite, jarosite and gypsum.

Schwertmannite, a poorly crystalline iron oxyhydroxysulfate, distributes widely in acid sulfate soil and sulfate-rich acid mine drainage (Collins et al., 2010; Regenspurg et al., 2004; Johnston et al., 2011; Sullivan and Bush, 2004; Fukushi et al., 2003a; Blgham et al., 1990;

Parafiniuk and Siuda, 2006, Burton et al., 2006). In some landscapes, schwertmannite may retard the mobility of arsenic. Arsenic concentration decreases with the presence of schwertmannite and up to 60 mg-As/g in nature was reported, suggesting that schwertmannite is a natural attenuator of arsenic in drainage (Fukushi et al., 2003a). Fukushi et al. (2003b) examined the sorption behavior of As(V) onto synthesized schwertmannite under acidic conditions for different As(V) concentrations and interpreted the results in terms of solid-solution reactions involving exchange between SO_4^{2-} and $H_2AsO_4^-$ together with OH^- on the surface of schwertmannite (Fukushi et al., 2003b). However, understanding of the mechanism of As(V) sorption is limited to the macroscopic level. Therefore, they further investigated at the molecular level by crystallographic consideration of the surface structure of schwertmannite. These results suggest that the reactive sites for As(V) sorption are surface coordinated ligand exchange with surface-adsorbed and structural SO_4, rather than surface hydroxyl groups (Fukushi et al., 2004). Structural analysis of As(V) to schwertmannite binding modes are still poorly documented as well. Waychunas et al. (1995) used X-ray absorption spectroscopy and concluded that arsenate appeared mainly as a bidentate sorption complex to the outside of crystallites, destabilizing the structure (Waychunas et al., 1995). Sakamaki et al. (2007) further reported that arsenate is bound to one or two iron octahedra with an increase of disorder in polymeric chains of iron octahedra (Sakamaki et al., 2007). On the other hand, the occurrence of significant amounts of sulfate ions upon sorption of arsenate on schwertmannite has led to the suggestion that arsenate could substitute for sulfate in the structure (Burton et al., 2009; Regenspurg and Peiffer, 2005; Burton et al., 2013). However, this kind of report is very limited. For example, Regenspurg and Peiffer (2005) have investigated synthetic schwertmannite and conducted that it could host up to 10.3 wt% arsenate without detectable structural changes as demonstrated by XRD (Regenspurg and Peiffer, 2005). Nevertheless, no other detailed mechanism was investigated. Despite this existing knowledge concerning the reactivity of As(III) with respect to schwertmannite in the laboratory, the mechanisms of As(III) scavenging by schwertmannite in AMD systems is still poorly documented (Maillot et al., 2013; Burton et al., 2009).

Jarosite, $KFe_3(SO_4)_2(OH)_6$, is a common Fe(III)-mineral in acid mine drainage and acid sulfate soils (Johnston et al., 2011; Roger and Herbert, 1997). It is believed that jarosite can co-precipitate with As(V) in the acid environment from tailings samples (Slowey et al., 2007; Nakazawa et al., 2009). In order to figure out how arsenic is incorporated in the structure,

Paktunc and Dutrizac (2003) and Savage et al. (2005) both investigated the speciation of arsenic in synthetic jarosite, confirming that AsO_4 substitution for SO_4 occurs in synthetic jarosite by XAS study (Savage et al., 2005; Paktunc and Dutrizac, 2003) with the amount up to 14.8 wt.% by XRD analyses (Paktunc and Dutrizac, 2003). Meanwhile, other studies have been made on As(V) mobilization by jarosite under different conditions, such as dissolution rates, sulfidation, decomposition (Johnston et al., 2013; Kendall et al. 2013; Patiño et al., 2013). Despite the fact that jarosite is known to incorporate As(V) to some extent, it is not an efficient sink for As(III) (Egal et al., 2009).

Gypsum, on the other hand, is one of the most abundant sulfate minerals and is often found in arsenic-contaminated tailings and waste water. For example, a large mass of gypsum was found in uranium tailings that have high concentrations of arsenic in Saskatchewan, Canada (Donahue and Hendry, 2003). Moreover, in Bigadiç borate deposits (Western Turkey), the waters are partially dominated by the $Ca–SO_4$ type in the mines, and high arsenic concentration is related to the leaching of the borate-bearing rocks (Gemici et al., 2008). Therefore, many studies have focused on the interaction between arsenic and gypsum. For example, Rodríguez-Blanco et al. (2007) reported that the interaction of dissolved As(V) and gypsum could result in surface precipitation of pharmacolite at pH 7 (Rodríguez-Blanco et al., 2007). Moreover, Rodríguez et al. (2008) investigated the condition at a starting pH 9 with other arsenates (e.g., guerinite, sainfeldite) on the surface of gypsum. These studies suggest that As(V) could be absorbed onto gypsum by forming a Ca-arsenate-sulfate solid solution. Apart from surface precipitation, Roman-Ross and co-workers have studied the precipitation of gypsum by mixing $CaCl_2$ and Na_2SO_4 in the presence of As(V) and they concluded that the replacement of sulfate SO_4^{2-} by arsenates AsO_4^{3-} (or $HAsO_4^{2-}$) in the gypsum structure supported by an increase of the unit-cell parameters (Roman-Ross et al., 2003; Fernández-Martínez et al., 2006; Fernández-Martínez et al., 2008).

(2) Arsenic and phosphate minerals

Studies have been carried out to explore the interaction between arsenic and phosphorus on the removal of arsenic. Due to similarities between phosphate and arsenate, phosphorus (P) can compete with arsenic for adsorption sites in soils. For instance, phosphate-induced release of

arsenic has been found to occur from lead arsenate contaminated soils with specific PO_4-AsO_4 exchange (Peryea, 1991) and it has a different influence on arsenate adsorption by soils because of the variation of the P/As molar ratio (Zeng et al., 2012). Moreover, a significant reduction in arsenate and arsenite adsorption onto ferrihydrite by the presence of phosphate, with a strong dependence on pH and phosphate concentration, was found by Jain and Loeppert (2000). Due to competing oxyanions, natural attenuation of arsenic by simple adsorption on phosphate is limited, but uptake by co-precipitation may sequester arsenic. Phosphate plays a role in arsenic extraction. Alam et al. (2001) used phosphate for arsenic extraction from synthetic arsenic-contaminated soils and found that phosphate could effectively attain arsenic with more than 40% extraction in the pH range of 6-8 (Alam et al., 2001). Zeng et al. (2008) showed that both H_3PO_4 and KH_2PO_4 can reduce the content of arsenic in soil and attributed it to the replacement of arsenic by PO_4^{3-}, attaining more than 20% arsenic removal at the concentration of 200 mmol/L (Zeng et al., 2008).

Among phosphate minerals, apatite, being stable in the natural environment, has received most attention for its potential to be used as an additive to water for decreasing the concentrations of toxic elements and as a soil amendment due to its ability for multiple ionic substitutions (Pan and Fleet, 2002; Thomson et al., 2003). Meanwhile, Bangladesh groundwater composition is found to be supersaturated with respect to hydroxylapatite (Ciardelli, 2006). Thus, on the basis of the existence of johnbaumite, an arsenate analog of hydroxylapatite, the anticipated ability to co-precipitate arsenic as a mixed HAP-johnbaumite-like phase has been documented (Zhu et al., 2009; Lee et al., 2009; Twidwell et al., 2005). For instance, Lee et al. (2009) investigated arsenate (As^{5+}) substitution in the hydroxylapatite structure by using a combination of crystallographic and spectroscopic method (Lee et al., 2009). Nakahira et al. (2006) reported the removal of arsenic in geothermal water by using hydroxyapatite-based materials including industrial waste with the replacement of PO_4^{3-} by $H_2AsO_4^-$ or $HAsO_4^{2-}$ in the apatite structure (Nakahira et al., 2006). However, knowledge about the mechanisms of replacement is limited.

Moreover, despite the abundance and diverse usage of phosphates such as struvite and newberyite as fertilizers in agriculture all over the world, relatively little is known about their interaction with arsenic. Struvite, in particular, has been reported to occur in arsenic-rich wastewaters (Sohel et al., 2010; Arai et al., 2003; Hunger et. al., 2008; Aguilera et al., 2010).

Limited attention has been paid on the mechanism of removal of arsenic by these phosphates (Ma and Rouff, 2012).

In summary, previous studies on arsenic contamination in natural environment and those associated with mining and agricultural activities focused largely on arsenic-rich minerals such as arsenates, arsenites, sulfarsenides, and sulfides. Rock-forming minerals albeit generally containing only minor or trace amounts of arsenic, owing to their sheer abundances are potentially important (and sometimes dominant) sources of this metalloid and can play significant roles in the attenuation and sequestration of arsenic in various environments. However, there remains a significant gap in my knowledge about arsenic speciation and uptake mechanisms in rock-forming minerals. This gap, at least partly, stems from the fact that most commonly used structural techniques (e.g., X-ray diffraction analysis, nuclear magnetic resonance spectroscopy, and Mössbauer spectroscopy) are incapable of studying dilute arsenic species (and other trace elements) in rock-forming minerals. This thesis research is intended to narrow this gap and to test the hypothesis that rock-form minerals, especially certain sulfates and phosphates, can accommodate significant amounts of arsenic and, therefore, exert profound impacts on the source, transport and bioavailability of this metalloid in the environment. Specifically, this research uses two highly sensitive structural techniques (i.e., synchrotron X-ray absorption spectroscopy and single-crystal electron paramagnetic resonance spectroscopy) to investigate arsenic speciation and uptake in selected rock-forming minerals (i.e., gypsum and struvite/newberyite). Gypsum is chosen in this study because it is a common secondary mineral in solid mine wastes (Jamieson, 2011). Billions of tones of gypsum are found as major by-product in borate deposits, uranium mine tailings, and phosphate fertilizer industry. Thus, study of arsenic speciation in gypsum is necessary which will potentially point to understanding arsenic mobilization in mine tailings. Struvite and newberyite, common biominerals and increasingly important green fertilizers, might contain a certain amount of metalloids while recovering phosphorus from wastewaters. Therefore, arsenic speciation in the two phosphate minerals are investigated which is relevant not only to the manufacture of green fertilizers from wastewaters but also to understanding arsenic in soils and removal of arsenic contamination in aqueous systems.

1.2 Thesis outline

The thesis is divided into six chapters. Chapter 2 provides background information about analytical techniques used in this work. Chapter 3 investigates the uptake and speciation of arsenic in both single crystals and crystalline powders of gypsum. Most of the materials in Chapter 3 have been published in a paper in Geochimica et Cosmochimica Acta (Lin, Chen, Nilges and Pan, 2013, Geochim. Cosmochim. Acta, Vol. 106: 524-540), with my co-authors Drs. Ning Chen and Mark J. Nilges assisted in synchrotron X-ray absorption and pulsed electron spin echo envelope modulation spectroscopic analyses, respectively. Chapter 4 reports on arsenic incorporation in struvite ($NH_4MgPO_4 \cdot 6H_2O$), with direct relevance to this material recovered from wastewaters as a green fertilizer. This chapter is adapted from a paper published in Environmental Science & Technology (Lin, Chen and Pan, 2013, Environ. Sci. Tech., Vol. 47: 12728-12735). Chapter 5 probes the speciation of As^{3+} and As^{5+} in arsenate-doped newberyite, in comparison with arsenic in struvite, and stems from a manuscript that is in preparation for submission. Chapter 6 summarizes the major conclusions obtained from this study and discusses problems encountered in this study and possible directions for future research in this area.

1.3 References

Aguilera, I., Daponte, A., Gil, F., HernÃ¡ndez, A. F., Godoy, P., Pla, A., and Ramos, J. L. (2010) Urinary levels of arsenic and heavy metals in children and adolescents living in the industrialised area of Ria of Huelva (SW Spain). *Environment International* **36**, 563-569.

Alam, M. G. M., Tokunaga, S., and Maekawa, T. (2001) Extraction of arsenic in a synthetic arsenic-contaminated soil using phosphate. *Chemosphere* **43**, 1035-1041.

Arai, Y., Lanzirotti, A., Sutton, S., Davis, J. A., and Sparks, D. L. (2003) Arsenic Speciation and Reactivity in Poultry Litter. *Environmental Science & Technology* **37**, 4083-4090.

Arslan, F., Arslan, C., and Çelik, M. S. (1999) Arsenic removal through the decrepitation of colemanite ores. *Powder Technology* **103**, 260-264.

Ashley, P. M. and Lottermoser, B. G. (1999) Arsenic contamination at the Mole River mine, northern New South Wales. *Australian Journal of Earth Sciences* **46**, 861-874.

Azcue, J. M. and Nriagu, J. O. (1995) Impact of abandoned mine tailings on the arsenic

concentrations in Moira Lake, Ontario. *Journal of Geochemical Exploration* **52**, 81-89.

Bates, M. N., Smith, A. H., and Hopenhayn-Rich, C. (1992) Arsenic ingestion and internal cancers: A review. *American Journal of Epidemiology* **135**, 462-476.

Berg, M., Tran, H. C., Nguyen, T. C., Pham, H. V., Schertenleib, R., and Giger, W. (2001) Arsenic contamination of groundwater and drinking water in Vietnam: A human health threat. *Environmental Science and Technology* **35**, 2621-2626.

Bhattacharya, P., Welch, A. H., Stollenwerk, K. G., McLaughlin, M. J., Bundschuh, J., and Panaullah, G. (2007) Arsenic in the environment: biology and chemistry. *Science of The Total Environment* **379**, 109-120.

Blgham, J. M., Schwertmann, U., Carlson, L., and Murad, E. (1990) A poorly crystallized oxyhydroxysulfate of iron formed by bacterial oxidation of Fe(II) in acid mine waters. *Geochimica et Cosmochimica Acta* **54**, 2743-2758.

Bowell, R. J. and Parshley, J. (2001) Characterization of waste, chemistry, and treatment and disposal, proceedings and summary report on U.S. EPA workshop on managing arsenic risks to the environment, May 1-3, Denver, Colorado, USA.

Burton, E. D., Bush, R. T., Johnston, S. G., Watling, K. M., Hocking, R. K., Sullivan, L. A., and Parker, G. K. (2009) Sorption of arsenic(V) and arsenic(III) to schwertmannite. *Environmental Science and Technology* **43**, 9202-9207.

Burton, E. D., Bush, R. T., and Sullivan, L. A. (2006) Sedimentary iron geochemistry in acidic waterways associated with coastal lowland acid sulfate soils. *Geochimica et Cosmochimica Acta* **70**, 5455-5468.

Burton, E. D., Johnston, S. G., Kraal, P., Bush, R. T., and Claff, S. (2013) Sulfate availability drives divergent evolution of arsenic speciation during microbially mediated reductive transformation of schwertmannite. *Environmental Science and Technology* **47**, 2221-2229.

Camm, G. S., Glass, H. J., Bryce, D. W., and Butcher, A. R. (2004) Characterisation of a mining-related arsenic-contaminated site, Cornwall, UK. *Journal of Geochemical Exploration* **82**, 1-15.

Chakraborti, D., Sengupta, M. K., Rahman, M. M., Ahamed, S., Chowdhury, U. K., Hossain, M. A., Mukherjee, S. C., Pati, S., Saha, K. C., Dutta, R. N., and Quamruzzaman, Q. (2004) Groundwater arsenic contamination and its health effects in the Ganga-Meghna-Brahmaputra plain. *Journal of environmental monitoring : JEM* **6(6)**, 74N-83N.

Chen, C. J., Chen, C. W., Wu, M. M., and Kuo, T. L. (1992) Cancer potential in liver, lung, bladder and kidney due to ingested inorganic arsenic in drinking water. *British Journal of Cancer* **66**, 888-892.

Chen, C. J., Kuo, T. L., and Wu, M. M. (1988) Arsenic and cancers. *Lancet* **1**, 414-415.

Chen, C. J., Wang, S. L., Chiou, J. M., Tseng, C. H., Chiou, H. Y., Hsueh, Y. M., Chen, S. Y., Wu, M. M., and Lai, M. S. (2007) Arsenic and diabetes and hypertension in human populations: A review. *Toxicology and Applied Pharmacology* **222**, 298-304.

Ciardelli, M. C. (2006) Arsenic uptake by coprecipitation in synthetic and natural Bangladesh groundwater: effect of oxyanions, heating, and seed crystals. *M.S. Thesis, University of Wisconsin-Madison*.

Collins, R. N., Jones, A. M., and Waite, T. D. (2010) Schwertmannite stability in acidified coastal environments. *Geochimica et Cosmochimica Acta* **74**, 482-496.

Das, D., Samanta, G., Mandal, B. K., Roy Chowdhury, T., Chanda, C. R., Chowdhury, P. P., Basu, G. K., and Chakraborti, D. (1996) Arsenic in groundwater in six districts of West Bengal, India. *Environmental Geochemistry and Health* **18**, 5-15.

Donahue, R. and Hendry, M. J. (2003) Geochemistry of arsenic in uranium mine mill tailings, Saskatchewan, Canada. *Applied Geochemistry* **18**, 1733-1750.

Drahota, P. and Filippi, M. (2009) Secondary arsenic minerals in the environment: A review. *Environment International* **35**, 1243-1255.

Egal, M., Casiot, C., Morin, G., Parmentier, M., Bruneel, O., Lebrun, S., and Elbaz-Poulichet, F. (2009) Kinetic control on the formation of tooeleite, schwertmannite and jarosite by Acidithiobacillus ferrooxidans strains in an As(III)-rich acid mine water. *Chemical Geology* **265**, 432-441.

Fernández-Martínez, A., Cuello, G. J., Johnson, M. R., Bardelli, F., Román-Ross, G., Charlet, L., and Turrillas, X. (2008) Arsenate incorporation in gypsum probed by neutron, X-ray scattering and density functional theory modeling. *Journal of Physical Chemistry A* **112**, 5159-5166.

Fernández-Martínez, A., Román-Ross, G., Cuello, G. J., Turrillas, X., Charlet, L., Johnson, M. R., and Bardelli, F. (2006) Arsenic uptake by gypsum and calcite: Modelling and probing by neutron and X-ray scattering. *Physica B: Condensed Matter* **385-386**, 935-937.

Foster, A., Ashley, R., and Rytuba, J. (2011) Arsenic species in weathering mine tailings and

biogenic solids at the Lava Cap Mine Superfund Site, Nevada City, CA. *Geochemical Transactions* **12**, 1-21.

Fukushi, K., Sasaki, M., Sato, T., Yanase, N., Amano, H., and Ikeda, H. (2003a) A natural attenuation of arsenic in drainage from an abandoned arsenic mine dump. *Applied Geochemistry* **18**, 1267-1278.

Fukushi, K., Sato, T., and Yanase, N. (2003b) Solid-solution reactions in As(V) sorption by schwertmannite. *Environmental Science & Technology* **37**, 3581-3586.

Fukushi, K., Sato, T., Yanase, N., Minato, J., and Yamada, H. (2004) Arsenate sorption on schwertmannite. *American Mineralogist* **89**, 1728-1734.

Garelick, H., Jones, H., Dybowska, A., and Valsami-Jones, E. (2008) Arsenic pollution sources. *Reviews of Environmental Contamination and Toxicology* **197**, 17-60.

Garelick, H., Jones, H., Dybowska, A., and Valsami-Jones, E. (2009) Arsenic Pollution Sources, *Reviews of Environmental Contamination Volume* **197**. Springer New York.

Gemici, Ü., Tarcan, G., HelvacI, C., and Somay, A. M. (2008) High arsenic and boron concentrations in groundwaters related to mining activity in the Bigadiç borate deposits (Western Turkey). *Applied Geochemistry* **23**, 2462-2476.

Guillot, S. and Charlet, L. (2007) Bengal arsenic, an archive of Himalaya orogeny and paleohydrology. *Journal of Environmental Science and Health - Part A Toxic/Hazardous Substances and Environmental Engineering* **42**, 1785-1794.

Hunger, S., Sims, J. T., and Sparks, D. L. (2008) Evidence for Struvite in Poultry Litter: Effect of Storage and Drying. *Journal of environmental quality* **37**, 1617-1625.

Jain, A. and Loeppert, R. H. (2000) Effect of competing anions on the adsorption of arsenate and arsenite by ferrihydrite. *Journal of Environmental Quality* **29**, 1422-1430.

Jamieson H. E (2011) Geochemistry and mineralogy of solid mine waste: Essential knowledge for predicting environmental impact. *Elements* **7**, 381-386.

Johnston, S. G., Burton, E. D., Keene, A. F., Planer-Friedrich, B., Voegelin, A., Blackford, M. G., and Lumpkin, G. R. (2013) Arsenic mobilization and iron transformations during sulfidization of As(V)-bearing jarosite. *Chemical Geology* **334**, 9-24.

Johnston, S. G., Keene, A. F., Bush, R. T., Burton, E. D., Sullivan, L. A., Isaacson, L., McElnea, A. E., Ahern, C. R., Smith, C. D., and Powell, B. (2011) Iron geochemical zonation in a tidally inundated acid sulfate soil wetland. *Chemical Geology* **280**, 257-270.

Kendall, M. R., Madden, A. S., Elwood Madden, M. E., and Hu, Q. (2013) Effects of arsenic incorporation on jarosite dissolution rates and reaction products. *Geochimica et Cosmochimica Acta* **112**, 192-207.

Lee, Y. J., Stephens, P. W., Tang, Y., Li, W., Phillips, B. L., Parise, J. B., and Reeder, R. J. (2009) Arsenate substitution in hydroxylapatite: Structural characterization of the $Ca_5(P_xAs_{1-x}O_4)_3OH$ solid solution. *American Mineralogist* **94**, 666-675.

Ma, N. and Rouff, A. A. (2012) Influence of pH and oxidation state on the interaction of arsenic with struvite during mineral formation. *Environmental Science & Technology* **46**, 8791-8798.

Maillot, F., Morin, G., Juillot, F., Bruneel, O., Casiot, C., Ona-Nguema, G., Wang, Y., Lebrun, S., Aubry, E., Vlaic, G., and Brown, G. E. (2013) Structure and reactivity of As(III)- and As(V)-rich schwertmannites and amorphous ferric arsenate sulfate from the Carnoulès acid mine drainage, France: Comparison with biotic and abiotic model compounds and implications for As remediation. *Geochimica et Cosmochimica Acta* **104**, 310-329.

Nakahira, A., Okajima, T., Honma, T., Yoshioka, S., and Tanaka, I. (2006) Arsenic removal by hydroxyapatite-based ceramics. *Chemistry Letters* **35**, 856-857.

Nakazawa, H., Haruysama, W., and Shinohe, T. (2009) Removal of aresenic with jarosite in acid mine drainage. *The Minerals, Metals and Materials Society - 3rd International Conference on Processing Materials for Properties 2008, PMP III* **1**, 327-332.

Paktunc, D. and Dutrizac, J. E. (2003) Characterization of arsenate-for-sulfate substitution in synthetic jarosite using X-ray diffraction and X-ray absorption spectroscopy. *The Canadian Mineralogist* **41**, 905-919.

Pan, Y. and Fleet, M. E. (2002) Compositions of the apatite-group minerals: substitution mechanisms and controlling factors. *Reviews in Mineralogy and Geochemistry* **48**, 13-49.

Parafiniuk, J. and Siuda, R. (2006) Schwertmannite precipitated from acid mine drainage in the Western Sudetes (SW Poland) and its arsenate sorption capacity. *Geological Quarterly* **50**, 475-486.

Patiño, F., Flores, M., Reyes, I., Reyes, M., Hernández, J., Rivera, I., and Juárez, J. (2013) Alkaline decomposition of synthetic jarosite with arsenic. *Geochem Trans* **14**, 1-9.

Peryea, F. J. (1991) Phosphate-induced release of arsenic from soils contaminated with lead arsenate. *Soil Science Society of America Journal* **55**, 1301-1306.

Rahman, M., Naidu, R., and Bhattacharya, P. (2009) Arsenic contamination in groundwater in the Southeast Asia region. *Environmental Geochemistry and Health* **31**, 9-21.

Ravenscroft, P., Burgess, W., Ahmed, K., Burren, M., and Perrin, J. (2005) Arsenic in groundwater of the Bengal Basin, Bangladesh:distribution, field relations, and hydrogeological setting. *Hydrogeol J* **13**, 727-751.

Regenspurg, S., Brand, A., and Peiffer, S. (2004) Formation and stability of schwertmannite in acidic mining lakes. *Geochimica et Cosmochimica Acta* **68**, 1185-1197.

Regenspurg, S. and Peiffer, S. (2005) Arsenate and chromate incorporation in schwertmannite. *Applied Geochemistry* **20**, 1226-1239.

Rodríguez-Blanco, J. D., Jiménez, A., and Prieto, M. (2007) Oriented Overgrowth of Pharmacolite ($CaHAsO_4 \cdot 2H_2O$) on Gypsum ($CaSO_4 \cdot 2H_2O$). *Crystal Growth and Design* **7**, 2756-2763.

Roger, B. and Herbert, J., 1997. Properties of goethite and jarosite precipitated from acidic groundwater, Dalarna, Sweden. *Clays and Clay Minerals* **45**, 261-273.

Roman-Ross, G., Charlet, L., Cuello, G. J., and Tisserand, D. (2003) Arsenic removal by gypsum and calcite in lacustrine environments. *Journal De Physique, IV : JP* **107**, 1153-1156.

Sakamaki, M., Takahashi, H., Konishi, T., Inoue, A., and Fujikawa, T. (2007) X-ray absorption fine structure spectroscopy study of arsenate adsorption on schwertmannite.

Savage, K. S., Bird, D. K., and O'Day, P. A. (2005) Arsenic speciation in synthetic jarosite. *Chemical Geology* **215**, 473-498.

Slowey, A. J., Johnson, S. B., Newville, M., and Brown Jr, G. E. (2007) Speciation and colloid transport of arsenic from mine tailings. *Applied Geochemistry* **22**, 1884-1898.

Smedley, P. L. and Kinniburgh, D. G. (2002) A review of the source, behaviour and distribution of arsenic in natural waters. *Applied Geochemistry* **17**, 517-568.

Smith, A. H., Lingas, E. O., and Rahman, M. (2000) Contamination of drinking-water by arsenic in Bangladesh: a public health emergency. *Bulletin of the World Health Organization* **78**, 1093-1103.

Sohel, N., Kanaroglou, P. S., Persson, L. A., Haq, M. Z., Rahman, M., and Vahter, M. (2010) Spatial modelling of individual arsenic exposure via well water: evaluation of arsenic in urine, main water source and influence of neighbourhood water sources in rural Bangladesh. *Journal of Environmental Monitoring* **12**, 1341-1348.

Stafilov, T., Aliu, M., and Sajn, R. (2010) Arsenic in surface soilsmffected by mining and metallurgical processing in K. Mitrovica Region, Kosovo. *Int J Environ Res Public Health* **7**, 4050-4061.

Sullivan, L. A. and Bush, R. T. (2004) Iron precipitate accumulations associated with waterways in drained coastal acid sulfate landscapes of eastern Australia. *Marine and Freshwater Research* **55**, 727-736.

Thomson, B., Smith, C., Busch, R., Siegel, M., and Baldwin, C. (2003) Removal of metals and radionuclides using apatite and other natural sorbents. *Journal of Environmental Engineering* **129**, 492-499.

Twidwell, L. G., Mccloskey, J., Lee, M. G., and Saran, J. (2005) Arsenic removal from mine and process waters by lime/phosphate precipitation. *The Minerals, Metals & Materials Society*.

Ujevic, M., Duic, Z., Casiot, C., Sipos, L., Santo, V., Dadic, Z., and Halamic, J. (2010) Occurrence and geochemistry of arsenic in the groundwater of Eastern Croatia. *Applied Geochemistry* **25**, 1017-1029.

Wang, S. and Mulligan, C. N., 2006. Occurrence of arsenic contamination in Canada: Sources, behavior and distribution. *Science of The Total Environment* **366**, 701-721

Waychunas, G. A., Xu, N., Fuller, C. C., Davis, J. A., and Bigham, J. M. (1995) XAS study of AsO_4^{3-} and SeO_4^{2-} substituted schwertmannites. *Physica B: Condensed Matter* **208–209**, 481-483.

Welch, A. H., Lico, M. S., and Hughes, J. L. (1988) Arsenic in ground water of the western United States. *Ground Water* **26**, 333-347.

WHO. (2001) Environmental health criteria 224, arsenic and arsenic compounds. Inter-organization programme for the sound management of chemicals. Geneva.

Zeng, M., Liao, B., Lei, M., Zhang, Y., Zeng, Q., and Ouyang, B. (2008) Arsenic removal from contaminated soil using phosphoric acid and phosphate. *Journal of environmental sciences (China* **20**, 75-79.

Zeng, X., Wu, P., Su, S., Bai, L., and Feng, Q. (2012) Phosphate has a differential influence on arsenate adsorption by soils with different properties *Plant, Soil and Environment - UZEI* **58**, 405-411

Zhu, Y., Zhang, X., Long, F., Liu, H., Qian, M., and He, N., 2009. Synthesis and characterization

of arsenate/phosphate hydroxyapatite solid solution. *Materials Letters* **63**, 1185-1188.

CHAPTER 2

Analytical techniques

The major techniques used in this study include electron paramagnetic resonance (EPR) spectroscopy, synchrotron X-ray absorption spectroscopy (XAS), and powder X-ray diffraction (PXRD) analysis. Other analytical techniques used for the characterization include pulsed electron nuclear double resonance spectroscopy (ENDOR), scanning electron microscopy (SEM), inductively coupled plasma mass spectrometry (ICPMS), and microbeam synchrotron X-ray fluorescence imaging (μ-SXRF).

Electron paramagnetic resonance (EPR) has superior sensitivity over other structural techniques and is capable of identifying and characterizing As^{3+} and As^{5+} species as well as determining the site occupancies and local environments of arsenic. It can detect extremely dilute paramagnetic centers which contain an unpaired electron(s) (0.0001%, Weil and Bolton 2007). Synchrotron X-ray absorption spectroscopy (XAS) can detect the oxidation states and local structural environments of arsenic in my arsenic-doped minerals. Powder X-ray diffraction (PXRD) is used for the identification of the synthetic minerals obtained in this thesis.

2.1 Electron paramagnetic resonance (EPR)

Electron paramagnetic resonance (EPR), often called electron spin resonance (ESR) as well, is a spectroscopic method for studying materials with at least one unpaired electron based on the observation of resonance absorption of microwave power. When placed in an external magnetic field, unpaired electrons will produce specific EPR signals that can be interpreted quantitatively and qualitatively. By using the obtained spectral parameters, not only the presence of a free radical can be proven, but also detailed chemical structure information can be detected, e.g., the presence and local structure of certain atoms. A large number of materials including free radicals, many transition metal ions and some defects are known to have unpaired electrons. Therefore, EPR has proven to be an indispensable tool in a large range of applications in physics, materials science, chemistry, biology, and geology, including studies of impurity states,

molecular clusters, antiferromagnetic, ferromagnetic, thin film compounds, and natural or induced radicals (Rieger, 2007; Weil and Bolton, 2007). In particular, EPR can readily distinguish the various paramagnetic As-associated oxyradicals to identify As^{3+} and As^{5+} species in arsenic-doped samples, on the basis of diagnostic ^{75}As hyperfine coupling constants.

2.1.1 EPR spin Hamiltonian

Spin Hamiltonian is the description of EPR line positions and relative intensities of paramagnetic species in samples. The spin Hamiltonian for arsenic radicals involving a single unpaired electron (S = 1/2) and a ^{75}As nuclear spin (I = 3/2), can be described as:

$$H_s = \beta_e \mathbf{S}\cdot\mathbf{g}\cdot\mathbf{B} + \mathbf{I}\cdot\mathbf{A}\cdot\mathbf{S} + \mathbf{I}\cdot\mathbf{P}\cdot\mathbf{I} - \beta_n \mathbf{I}\cdot g_n\cdot\mathbf{B} \qquad (2.1)$$

The first term is the electron Zeeman interaction, where $\beta_e = 9.27400899*10^{-24}$ $J\cdot T^{-1}$ is the Bohr magneton, **B** is the external magnetic field vector, **g** is the g tensor, and **S** the electronic spin vector operator.

The g tensor is a complicated function of the frontier orbitals of the molecule. It is sufficiently distinctive, so that it can be used as fingerprint information for the identification of paramagnetic centers.

In a simple case of a single free electron, the unpaired electron has a spin quantum number S = 1/2, which gives it a magnetic property known as a magnetic moment with two quantum states. This magnetic moment makes the electron behave like a tiny bar magnet. When an external magnetic field is applied, the two states orient in opposite directions parallel and antiparallel to the direction of the applied magnetic field. The energy separation between the two spin states is

$$\Delta U = g_e \beta_e B_0 \qquad (2.2)$$

where g-value (or g-factor) of a free electron is a dimensionless fundamental constant, g_e = 2.002316. β_e is the Bohr magneton (a fundamental constant) and B_0 is the strength of applied magnetic field. The magnitude of the splitting is dependent on the strength of the applied

magnetic field. By absorbing a quantum of electromagnetic radiation *hν*, the lower energy state can be excited to an upper state. When satisfying the resonance conditions, $g_e\beta_e B_0 = h\nu$, EPR absorption is observed (Fig. 2-1) (Weil and Bolton, 2007; Brustolon and Giamello, 2009). The process is called the electronic Zeeman effect.

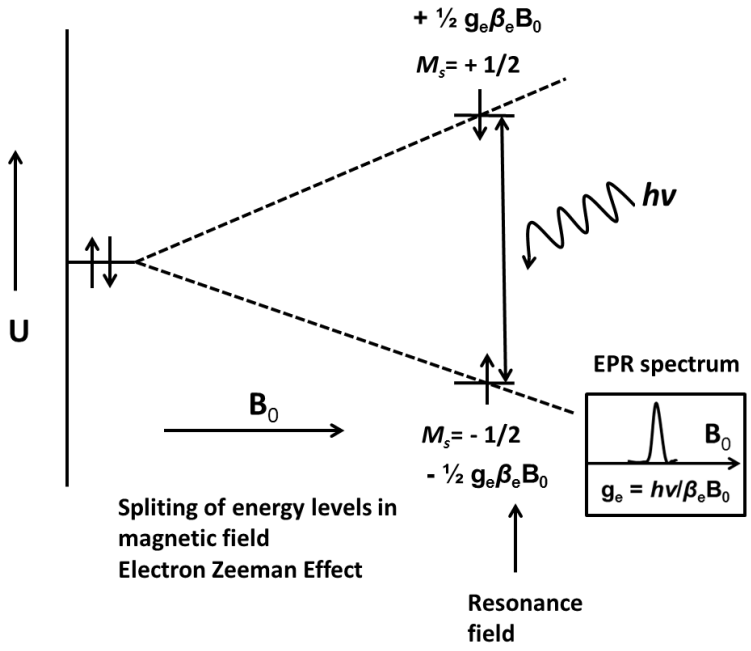

Figure 2-1 The Zeeman splitting for a $S = 1/2$ system with one unpaired electron in an external magnetic field $\mathbf{B}_0$.

In the solid states, a paramagnetic ion is not free, but is surrounded by other ions. These neighboring ions have strong interactions with the paramagnetic ion, thus producing a strong electric field or "crystal field" in addition to the existing local field created by the paramagnetic ion. Therefore, the quantization axis of the electron spin is not necessarily parallel to the applied magnetic field but can have different directions for different orientations of the molecule. In the anisotropic system, the resonance field B is a function of the orientation of the field relative to a crystal or molecular axis in the applied magnetic field and a variation in g with orientation is required with the contribution of angular dependence (Wertz and Bolton, 1972; Weil and Bolton, 2007). The principal components are g_{xx}, g_{yy} and g_{zz}. The isotropic g-value is defined as $g_{iso}=(g_{xx}+g_{yy}+g_{zz})/3$.

The second term in the Eq (2.1) corresponds to the hyperfine interaction which is used for

the interaction of the electronic spin **S** with the nuclear spin **I** through the hyperfine coupling tensor **A**, with three principal components A_{xx}, A_{yy}, A_{zz} along the principal axis system X, Y, Z. Without the additional energy level splitting arising from the interaction of the nuclear and electron magnetic moments, only one line would be observed for single electron spin systems.

There are two contributions to the hyperfine coupling of the electron spin to the nuclear spin: Fermi-contact interaction and dipole-dipole coupling between the two magnetic moments. The Fermi-contact is resulted from non-zero electron spin probability density at the nucleus. This only occurs in the s-orbitals of the atoms, as s orbitals are spherically symmetric. Fermi-contact interaction gives rise to the isotropic (orientation-independent) hyperfine coupling with $A_{iso}= (A_{xx}+ A_{yy}+ A_{zz})/3$. The dipolar interaction derives from unpaired electron from p, d, f, etc., orbitals, because in these orbitals all of them have a node at the nucleus. This non-spherical symmetry in these orbitals leads to unequal dipole-dipole coupling between the magnetic moments of the electron and nuclear spin, resulting in an anisotropic (dependent on the orientation of **B** with respect to a molecular axis) hyperfine coupling (Atherton, 1993; Brustolon and Giamello, 2009).

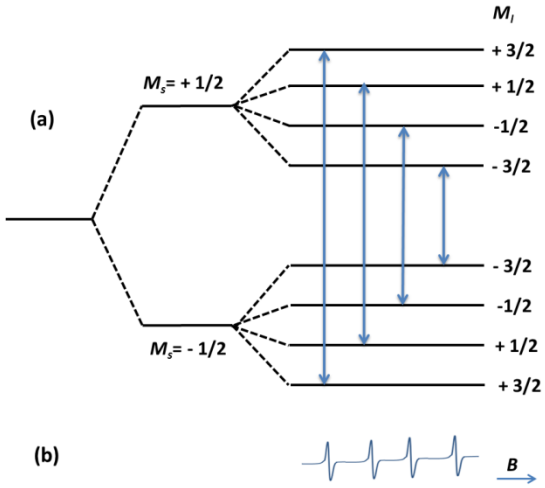

Figure 2-2 (a) Energy levels and allowed EPR transitions at constant field for ^{75}As with S = 1/2, I = 3/2. (b) simulated spectrum at a constant frequency.

^{75}As has a single unpaired electron (S = 1/2) with hyperfine interaction with nuclear spin I = 3/2. States with S = 1/2 are referred as doublet states since the multiplicity 2S+1 is equal to 2

and the nuclear spin quantum number $I = 3/2$ is corresponding to four multiplicity of nuclear spin states given by $2I+1$. Thus the energy level of this system consists of four transition lines separated by the hyperfine splitting. Figure 2-2 shows the energy levels and transitions for ^{75}As with $S = 1/2$ and $I = 3/2$ as a function of magnetic field and spectrum at a constant frequency (Wertz and Bolton, 1972).

The third term is the nuclear quadrupole interaction describing an interaction between the nuclear spin and local electric-field gradients acting on it due to the electron distribution in the immediate neighborhood. The electric-field gradients can orient the charge ellipsoid of the nucleus, with energy of alignment called nuclear quadrupole energy. Usually this happens when a nuclear spin $I > 1/2$ characterized by a non-spherical charge distribution, such as p and d orbitals.

In EPR spectra, nuclear quadrupole interactions might cause the allowed transitions to shift in position and vary in intensity, and cause the appearance of forbidden transitions. Both contributions caused by the small second-order effects are hard to observe (Atherton, 1993; Schweiger and Jeschke, 2001; Weil and Bolton, 2007).

The fourth term is the nuclear Zeeman interaction. It is an analogue of the electronic Zeeman interaction with nuclear spins coupled to the external magnetic field. The spin quantum number I and the g_n factor are inherent properties of a nucleus. Here g_n is the dimensionless nuclear g-factor, which is a constant depending on the type of nucleus, and β_n is the nuclear magneton (Schweiger and Jeschke, 2001).

2.2 Synchrotron X-ray absorption spectroscopy (XAS)

Synchrotron X-ray absorption spectroscopy, a local structure probe, is a unique technique providing reliable information concerning the local atomic arrangement around the selected elements that are contained within a material as well as the electronic structure. It can be applied not only to crystalline samples, but also to non-crystalline samples. Both kinds of samples are treated on the same basis as no long-range order is required. Therefore, X-ray absorption

spectroscopy is broadly used in physics, biology, geochemistry, medicine, environmental science and material science (Koningsberger, 1988; Bunker, 2010). This technique is used in this thesis for identifying the oxidation states and local structural environments of arsenic in arsenic-doped minerals.

In X-ray absorption experiments, when an incident X-ray hits a sample, the energy of an X-ray photon is absorbed by an atom and gives rise to the transition of an electron from inner atomic orbital to an unoccupied state. This absorption is dependent on the energy and the atoms. At specific energies where the absorption suddenly increases dramatically, it will produce an edge called an X-ray absorption edge. Such an edge only occurs when the incident photon energy is sufficient to excite a core electron from low-energy bound state in an atom to a continuum state, i.e., to produce a photoelectron. Thus the energies of absorption edges are corresponding to the electron binding energies that are characteristic of each element in materials (Bunker, 2010).

X-ray absorption spectroscopy is a technique of measuring the variations of μ as a function of X-ray energy E with the corresponding absorption spectrum as a plot of μ(E). Practically, the absorption coefficient μ(E) can be measured in two ways: one is in transmission mode, where the absorption is measured directly by measuring the number of photons transmitted through the sample. The second way is in fluorescence mode, the intensity of the emitted fluorescent X-rays.

When transmitting through a sample, an X-ray becomes attenuated. The absorption of the incident X-rays made in a transmission experiment may be described:

$$\mu x = \ln (I_0 / I_1) \qquad (2.3)$$

where μ is the absorption coefficient depending on the types of atoms (i.e., atomic number Z, the atomic mass A) and the density of the material as well. And x is the thickness of the sample. I_0 and I_1 are the intensities of the incoming and transmitted beams, respectively (Koningsberger, 1988).

In the XAS measurements made by fluorescence mode, the X-rays produced by filling the core hole generating by the absorption of X-ray photon are measured. Since this produced fluorescent X-ray (I_f) is proportional to the amount of absorbed X-rays directly, the fluorescence yield (I_f/I_0) is proportional to the absorption by using the equation:

$$\mu x \approx I_f/I_0 \quad (2.4)$$

Generally, X-ray absorption spectra discern two main regions: the X-ray absorption near edge structure (XANES) and the extended X-ray absorption fine structure (EXAFS) (Fig. 2-3). Both of them provide valuable information about a sample.

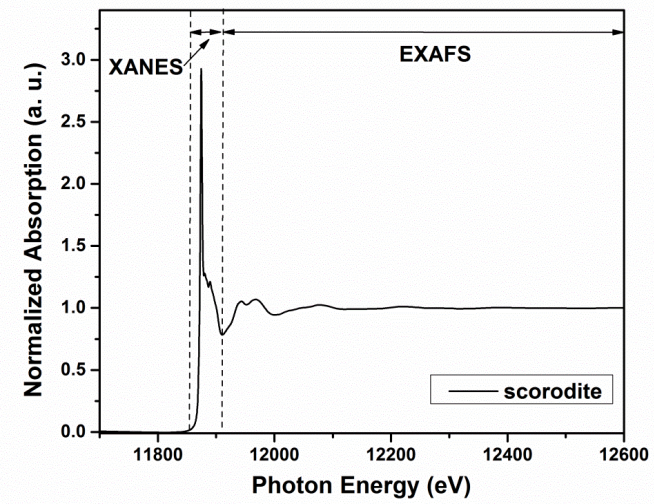

Figure 2-3 Definition of the XANES and EXAFS regions of As K-edge X-ray absorption spectra in scorodite.

2.2.1 X-ray absorption near edge structure (XANES)

The X-ray absorption near edge structure (XANES) provides information about the feature immediately adjacent to the edge. There are three parts concerned: the pre-edge region, the edge region and the near-edge region which may contain important information such as the oxidation state, local site symmetry, and bonding characteristics of specific elements in a sample.

The pre-edge feature is dominated by the electron transitions to higher unoccupied or half-occupied orbitals. These transitions are usually found in transition metal XANES spectra which perform as an indicator of local site symmetry and orbit occupancy (Bunker, 2010).

In the edge region, a sudden increase in absorption is observed which is related to the binding energies in K, L, M, etc. shells (based on the Bohr atomic model, n=1 for K edges, n=2 for L edges, n=3 for M etc.) that are characteristic of each element in materials. The K-edge refers to the excitation of 1s ($^2S_{½}$) electrons, whereas, the L1-edge is related to excitation of 2s

($^2S_{½}$) electrons, and the L2- and L3-edges are about the excitation 2p($^2P_{½}$), and 2p($^2P_{3/2}$), respectively (Hippert et al., 2006; Bunker, 2010). The position of absorption edges may be shifted corresponding to the change of oxidation-state of the absorption atoms. The absorption edge energy increases correspondingly with increasing the oxidation-state of the absorption atoms. Thus, these shifts can be helpful in determining the valence state of an unknown sample by using standard compounds. Moreover, the coordination and bond lengths can have impact on the absorption edge energy as well (Azaroff, 1974; Bunker, 2010).

The near-edge region refers to the energy range from a few eV to 50 eV above the absorption edge. In this region, the energy of the ejected photoelectrons is relatively low as E-E0 is low. Thus, multiple scatterings are dominant. These scattering resonances are dependent on the atomic position of neighboring atoms. Therefore, the information of the geometry of the arrangement of surrounding atoms is detectable through this region (Azaroff, 1974; Agarwal, 1991).

2.2.2 Extended X-ray absorption fine structure (EXAFS)

Extended X-ray absorption fine structure is generally starting at roughly 50 eV and extending to about 1000 eV or further above the absorption edge E0 (Agarwal, 1991). In this region, local structural information for an atom: i.e., bond distances, coordination number and type of neighbor atoms can be obtained (Koningsberger, 1988).

In EXAFS data analysis, the data usually is reduced to a χ function, a normalized oscillatory part of the linear absorption coefficient. Theoretically, the function χ can be roughly defined in terms of the absorption coefficient as a function of energy.

$$\chi(E) = \frac{\mu(E) - \mu_o(E)}{\Delta\mu_o(E)} \qquad (2.5)$$

where $\mu_o(E)$ is a smooth background function referring to the absorption of the absorption coefficient of the central atom without any scattering by other atoms located in the vicinity of the central atom. $\Delta\mu_0(E)$ represents a normalization function measuring the edge jump.

The EXAFS data is obtained from the interference between the photoelectron emitted from the absorbing atom and the backscattered photoelectron from the neighboring atoms. In the

absorption process, the photoelectron ejects as a spherical wave centered at the absorber atom. The photoelectron can be scattered by other atoms located in the vicinity of this absorber. The interference between the outgoing and the scattered waves can be either constructive or destructive depending on the different ratios between the distance to the neighbor atom and the wavelength of the photoelectron (Hippert, 2006). Therefore, when interpreting data for the EXAFS, it is generally practical to use the photoelectron wave vector, *k*, an independent variable, that is proportional to momentum rather than energy. The conversion from E to *k* is:

$$k = \sqrt{\frac{2m_e(E-E_0)}{\hbar^2}} \qquad (2.6)$$

In order to amplify the oscillations graphically for a suitable power of *k* weighing for $\chi(k)$, *k* is often plotted as k^3. Standard EXAFS equation can be recorded as:

$$\chi(k) = \sum_j \frac{N_j f_j(k) S_0^2 \exp\left[-2k^2\sigma_j^2\right]\exp[-2R_j/\lambda(k)]}{kR_j^2}\sin[2kR_j + \delta_j(k)] \qquad (2.7)$$

$f_j(k)$ is the effective backscattering amplitude function. $\delta_j(k)$ is the phase shift. S_0^2 represents the amplitude reduction function referring to the reduction of signal due to inelastic losses within the absorbing atom. It is intrinsic but weakly energy dependent which is usually approximated by a constant. Debye-Waller term $\exp\left[-2k^2\sigma_j^2\right]$ refers to the mean-square disorder in both static and thermal. σ is the half width maximum for a Gaussian distribution. σ_j^2 ($Å^2$) represents the mean square-displacement (known as the Debye-Waller factor as well) in the bond distance R. Most parameters in the equation can be calculated for a certain *k* value; however, R, N, and σ are remaining unknowns which are related to radius, coordination number, and the measure of disorder in neighboring atoms, respectively (Azaroff, 1974; Koningsberger, 1988; Rehr and Albers, 2000).

Fourier transformation is introduced in EXAFS data analysis due to containing different frequencies corresponding to different distances from the absorbing atom for coordination shell in the EXAFS oscillations. A Fourier transform of the EXAFS function in *k*-space, $\chi(k)$, gives a radial distribution function, providing meaningful visual representation of the electron density around the absorbing atom in a one dimensional R-space (Bunker, 2010).

2.3 Powder X-ray diffraction (PXRD)

X-ray diffraction (XRD), a widely used technique, has contributed to a large extent to the determination of the structure of crystalline solids.

When an X-ray beam enters the crystal, the photons can be diffracted with many specific directions which can be described by Bragg's Law:

$$2d \sin\theta = n\lambda \quad (2.8)$$

d is the spacing between crystal planes, θ is the incident angle, n is any integer, and λ is the wavelength of the incident beam.

By measuring the angles and intensities of these diffracted beams, the crystal structure could be determined. Each crystalline sample has its unique characteristic X-ray powder pattern, thus, it may be used as a "fingerprint" for its identification (Guinier, 1963; Liang, 2011). All my arsenic-doped samples are synthetic crystalline samples, therefore, this technique is helpful for identification the phases.

2.4 References

Agarwal B.K. (1991) X-ray spectroscopy, 2nd edition, Springer-verlag, Berlin.

Atherton N. M. (1993) Principles of electron spin resonance. Ellis Horwood, Chichester.

Azaroff L. V. (1974) X-ray spectroscopy. McGraw-Hill, New York.

Brustolon M. and Giamello E. (2009) Electron paramagnetic resonance: a practitioner's toolkit. John Wiley & Sons, New Jersey.

Bunker G. (2010) Introduction to XAFS: a practical guide to X-ray absorption fine structure spectroscopy. Cambridge University Press, New York.

Koningsberger D. C. (1988) X-Ray Absorption: principles, applications, techniques of EXAFS, SEXAFS and XANES. John Wiley and Sons, New York.

Guinier A. (1963) X-ray diffraction: in Crystals, imperfect crystals, and amorphous bodies. V. H. Freeman & Company, San Francisco.

Liang D. (2011) Fundamentals of X-ray crystallography. Science Press/Oxford: Alpha Science International Ltd.

Hippert F., Geissler E., Hodeau J. L., Lelièvre-Berna E. and Regnard J.-R. (2006) Neutron and X-ray spectroscopy. Springer, Netherlands.

Rehr J. J. and Albers R.C. (2000) Theoretical approaches to X-ray absorption fine structure. *Reviews of Modern Physics*, **72**, 621-654.

Rieger P. H. (2007) Electron spin resonance: analysis and interpretation. RSC Publishing, Cambridge, UK.

Schweiger A. and Jeschke G. (2001) Principles of pulse electron paramagnetic resonance. Oxford University Press, Oxford.

Weil J. A. and Bolton J. R. (2007) Electron paramagnetic resonance: elementary theory and practical applications, 2nd Edition. John Wiley& Sons, New Jersey.

Wertz J. E. and Bolton J. R. (1972) Electron spin resonance: elementary theory and practical applications. McGraw-Hill, New York.

CHAPTER 3

Arsenic uptake and speciation in synthetic gypsum

3.1 Introduction

Widespread arsenic contaminations with adverse effects to human health are known in many parts of the world, particularly those associated with mining and milling processes of mineral deposits (Foster et al., 1998; Vaughan, 2006; Ravenscroft et al., 2009; Majzlan et al., 2011). One such example is from Anatoly plateau of Turkey, concentrations up to 3000 ppm As exist in shallow aquifers related to borate deposits, and episodes of arsenic poisoning have been reported (Çolak et al., 2003; Delfini et al., 2003; Gemici et al., 2008). Turkish borate deposits, similar to their counterparts elsewhere, contain abundant sulfarsenides (realgar, orpiment and arsenopyrite; Helvaci and Alonso, 2000). The principal by-product from the milling processes of borate deposits, which involves dissolution of calcium borates in sulfuric acid to produce boric acids, is gypsum (Delfini et al., 2003). This gypsum sludge, which contains ~2,000 ppm As and is known as "arsenical borogypsum wastes", represents a major source of arsenic contamination, because of its enormous quantity formed from the annual production of ~2.5 billion tons of borate ores in Turkey (Delfini et al., 2003; Alp et al., 2009).

Similarly, large quantities of gypsum or "phosphogypsum" accumulated from the production of phosphate fertilizer are known to contain a variety of heavy metalloids, including As. In addition, gypsum is a major constituent in many uranium mine tailings, because of the common use of sulfuric acid and lime in the extraction of uranium. Uranium mine tailings are known to contain elevated levels of As (up to 12,700 ppm in the Key Lake mine tailings, Donahue and Hendry, 2003; Moldovan et al., 2003). Therefore, gypsum as one of the most common and abundant secondary minerals (Jamieson, 2011) is expected to exert important influences on the stability and bioavailability of arsenic in these mine tailings and surrounding areas.

Several previous studies (Roman-Ross et al., 2003; Fernandez-Martinez et al., 2006, 2008; Rodriguez-Blanco et al., 2007; Rodriguez et al., 2008) investigated incorporation of arsenic in

gypsum but reported contradictory results. For example, Rodriguez-Blanco et al. (2007), in a SEM-EDS study of co-crystallized pharmacolite ($CaHAsO_4 \bullet 2H_2O$) and gypsum, did not detect any substitution between As^{5+} and S^{6+}. On the other hand, Fernandez-Martinez et al. (2006, 2008), in their studies of synthetic gypsum by combined neutron and X-ray diffraction analyses, synchrotron X-ray absorption spectroscopy (XAS) and density functional theory (DFT) modeling, reported substitution of As^{5+} for S^{6+} at the tetrahedral site (Fig. 3-1). This discrepancy most likely stems from different sensitivities of analytical techniques employed in these previous studies (Fernandez-Martinez et al., 2006, 2008; Rodriguez-Blanco et al., 2007). Also, Rodriguez-Blanco et al. (2007) determined the solubility constant for pharmacolite and noted that pharmacolite is less soluble than gypsum. Therefore, kinetic factors may be important in the formation of pharmacolite instead of As-bearing gypsum in As-rich systems.

In this contribution, I investigate arsenic-bearing synthetic gypsum by use of synchrotron XAS, electron paramagnetic resonance spectroscopy (EPR), and pulsed electron nuclear double resonance spectroscopy (ENDOR). The main advantages of the EPR technique are 1) its superior sensitivity over other analytical techniques such as neutron and X-ray diffraction analysis (Pan et al., 2002) and 2) ability to identify and quantitatively characterize various As^{3+} and As^{5+} species (Mao et al., 2010; Di Benedetto et al., 2011). In particular, quantitative analysis of single-crystal EPR and ENDOR spectra allows determination of orientations of paramagnetic centers, which can be used to establish site occupancies and local structural environments by comparison with

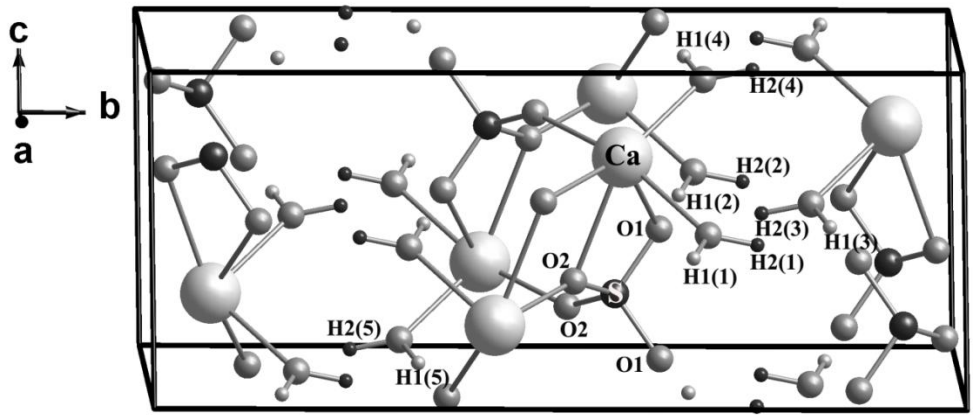

Figure 3-1 Crystal structure of gypsum (data from Schofield et al. 1996) showing the local structural environment of the S site, with the hydrogen atoms of five closest water molecules labeled.

the symmetry and bond directions of the host phase. My synchrotron XAS, single-crystal EPR and ENDOR results reported herein confirm previous suggestions of Roman-Ross et al. (2003) and Fernandez-Martinez et al. (2006, 2008) for lattice-bound As^{5+} in gypsum. Moreover, my data demonstrate incorporation of As^{3+} in gypsum for the first time. Furthermore, results from crystalline powder samples with different pH values show that uptake of arsenic in gypsum is pH dependent. These results not only shed new light on the effect of gypsum on the stability of arsenic in mine tailings but point to potential application of this mineral for immobilization and removal of arsenic contamination in aqueous environments.

3.2 Arsenic speciation in single-crystal samples of synthetic gypsum

3.2.1 Synthesis experiments and analytical techniques

3.2.1.1 Gel growth and characterization of As-doped gypsum

Two experiments using the sodium metasilicate gel method (Raju, 1983a, b) have been made to synthesize As-doped gypsum. Both experiments used ~40 ml sodium metasilicate (Na_2SiO_3) solution with a density of 1.05 g/cm^3, which was first adjusted to pH = 7.5 by using acetic acid and then poured into a U-tube. In the first experiment, 10 ml solution of mixed 1 M ammonium sulfate [$(NH_4)_2SO_4$, 99% pure] and 0.02 M sodium hydrogen arsenate heptahydrate ($Na_2HAsO_4 \bullet 7H_2O$, 98%) was poured into one limb of the U tube, and 10 ml of 1 M calcium chloride ($CaCl_2$, 97%) was added to the other limb. The second experiment used the same procedure and similar chemicals, except for a 0.07 M $NaAsO_2$ standard solution as the source for As. All chemicals from Alfa Aesar were used without any further purification. The addition of solutions to the two limbs of the U-tubes was done slowly to minimize disturbance of the sodium metasilicate gel. The U-tubes for two experiments were left at room temperature for three and five months, respectively.

Crystals of gypsum from these two experiments, denoted as Samples #1 and #2 hereafter, were first examined by optical microscopy and were then confirmed by powder X-ray diffraction analysis. Crystals (up to 1 mm x 1 mm x 3 mm) of Sample #1 have similar morphologies to those

described in Raju (1983b), including the characteristic twin with the twin plane parallel to ($\bar{1}01$). Crystals of Sample #2 have similar sizes but do not have any evidence of twinning. Chemical analyses using inductively coupled plasma mass spectrometry (ICP-MS), with the standard HF-HNO_3 dissolution method, showed that Samples #1 and #2 contains 1,900 and 185 ppm As, respectively.

3.2.1.2 Arsenic K edge XAS measurements

Arsenic K edge XAS data were collected at the HXMA beamline, Canadian Light Source (Jiang et al., 2007). Experimental data for seven model compounds (arsenopyrite, realgar, orpiment, arsenolite, synthetic scorodite, and As_2O_3 and As_2O_5 from Alfa Aesar) and the two gypsum samples after being pulverized to powder were measured as pressed pellets at room temperature in transmission and fluorescence modes, respectively. Mixed properly with boron nitride, the model compounds were diluted, thus roughly have edge jump of unity. The straight ion chamber detectors were used in the transmission mode experiment, whereas a 32 element Ge detector was used for the fluorescence mode data collection. Multi-scan data were collected during all experiments: i.e., 3 scans for each model compound, and 3 and 22 scans for Samples #1 and #2, respectively. A Si(111) monochromator crystal and Rh mirrors (collimating and focusing mirrors) were used during data collection. The sizes of scan steps for the pre-edge, XANES, and EXAFS regions were 10 eV/step, 0.25 eV/step, and 0.05 $Å^{-1}$/step, respectively.

3.2.1.3 Single-crystal X-band EPR measurements

Single-crystal X-band EPR measurements at room temperature (~294 K) were made on a Bruker EMX instrument at the Saskatchewan Structure Sciences Centre, University of Saskatchewan, equipped with an automatic frequency controller, a high-sensitivity ER4119 cavity, and a home-made goniometer with a precision of ~0.2º. Calibration of the magnetic field was made by use of the free radical α,γ-bis-diphenylene-β-phenyl allyl (BDPA) in benzene (g = 2.0027).

Several gypsum crystals from both synthesis experiments were first examined by

reconnaissance single-crystal EPR measurements without any irradiation. Subsequently, one crystal from each synthesis experiment was irradiated at room temperature in a ^{60}Co cell, with a dose rate of ~460 Gy/h, for 5 days, yielding a total dose of ~5.5 kGy. The irradiated crystal of Sample #1 was then used for single-crystal EPR measurements at room temperature in two rotation planes. Experimental conditions included microwave frequency of ~9.386 GHz, microwave power of ~20 mW, modulation frequency of 100 kHz, and modulation amplitude of 0.1 mT, and a constant angle interval of 5º. At each crystal orientation, three spectra of different scan ranges and spectral resolutions were collected. They include one wide scan from 215 mT to 445 mT with a spectral resolution of ~0.112 mT (i.e., 2,048 field data points over 230 mT) and two narrow scans from 225 to 245 mT and from 328 to 340 mT, with spectral resolutions of ~0.019 mT and 0.012 mT (1,024 points over 20 mT and 12 mT), respectively.

Single-crystal EPR measurements for the gamma-ray-irradiated crystal of Sample #2 were made at 85K in two rotation planes: one parallel to the (100) crystal face and another along the {010} cleavage. Other experimental conditions were similar to those described above, except that only one wide-scan spectrum from 215 mT to 465 mT with a spectral resolution of ~0.061 mT (i.e., 4,096 data points over 250 mT) was collected at each crystal orientation.

3.2.1.4 Single-crystal Q-band EPR measurements

The irradiated crystal of Sample #1 was also measured at Q-band frequencies (~34.7 GHz) at the Illinois EPR Research Center (IERC), University of Illinois at Urbana-Champaign. Q-band spectra were collected in two rotation planes parallel to the ($\bar{1}$01) twin plane and the {010} cleavage plane. Experimental conditions included modulation amplitude of 0.1 mT, microwave power of 15 dB, scan range from 1,185 mT to 1,285 mT, spectral resolution of 0.024 mT (4,096 data points over 100 mT), and angle intervals of 10º to 15º.

3.2.1.5 Pulsed ENDOR measurements

Pulsed ENDOR spectra at 60 K were collected on a Bruker E580-10 Elexsys with a liquid He Oxford CF935 cryostat, at IERC. ENDOR experiments were made using a Mims three-

pulse scheme ($\pi/2 - \tau - \pi/2 - T - \pi/2 - \tau -$ echo, with the RF pulse applied during time T and the frequency of which is varied in time). Because Mims ENDOR gives rise to blind-spots that originate from an oscillating τ dependence, ENDOR spectra were also recorded as a function of τ and later summed (32 spectra @ 16ns steps).

All ENDOR spectra were measured on a twinned crystal from Sample #1, which was also measured by X-band (~9.6 GHz) EPR at 60 K. Sets of EPR and pulsed ENDOR data were first obtained for one plane within a degree of the twin plane ($\bar{1}01$). A second plane that is approximately normal to both the ($\bar{1}01$) and (010) planes was also run. This plane was found to be tilted away from the b-axis by 14.6° and as such as many as four sites per orientation can be observed (effective D2 symmetry). Angle corrections were calculated from the fitting of the EPR spectra of the $[AsO_3]^{2-}$ center. ENDOR spectra were then simulated using SIMEND, which is a version of SIMPIP that calculates a frequency swept ENDOR spectrum and includes an intensity weighting function for the Boltzman population and angle-selection (Andruzzi et al., 2005; Barqueara et al., 2006). All 56 ENDOR spectra from the two planes were fitted simultaneously. A non-standard τ dependent Mims ENDOR efficiency factor was used (Nilges et al., 2009).

3.2.2 Results and discussion

3.2.2.1 Arsenic K edge XANES and EXAFS spectra

The main peak in the As K edge XANES spectrum of gypsum at 11,874.4 eV (Fig. 3-2a) is similar to those of scorodite and As_2O_5, indicative of the As^{5+}oxidation state. The shoulder at 11,870.7 eV (marked by a vertical line, Fig. 3-2a) is same to those of arsenolite and As_2O_3, suggesting the presence of As^{3+}. The presence of both As^{3+} and As^{5+} is also evident in the first-derivative XANES spectrum, indicated by the two peaks at 11,869.2 eV and 11,872.9 eV that are observed in arsenolite and scorodite, respectively (Fig. 3-2b). Comparison of these XANES spectra shows that Sample #1 has a notably lower As^{3+}/As^{5+} value than Sample #2. Also, the line shapes of both Samples #1 and #2 remain unchanged during the multi-scan experiments, suggesting that the oxidation states of As in these samples were not affected significantly by the

incident X-ray beam.

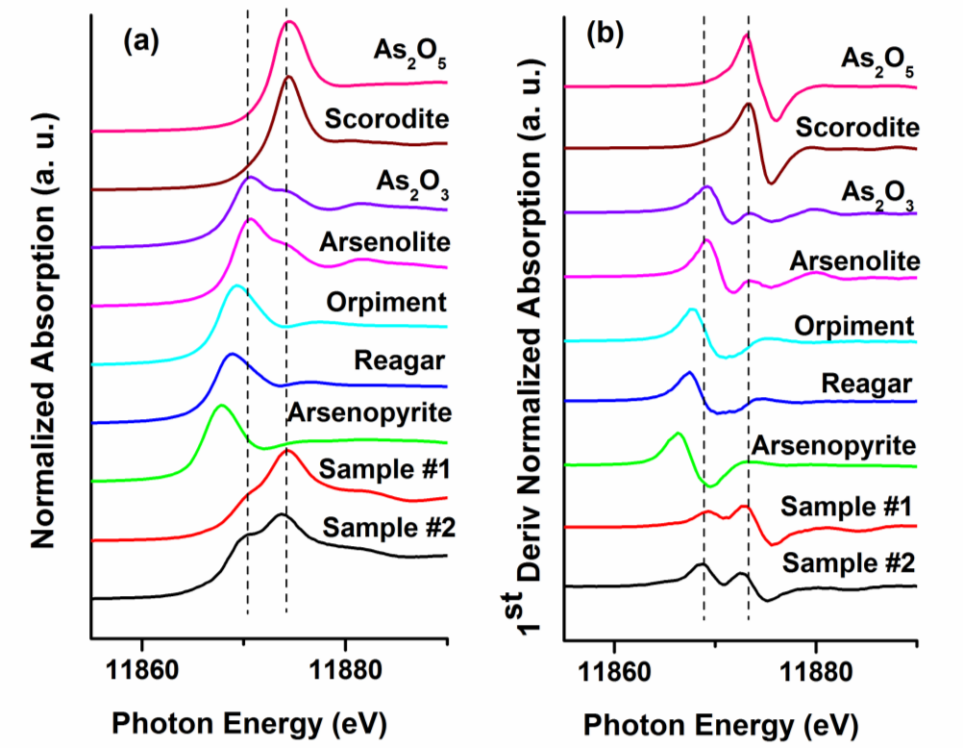

Figure 3-2 (a) As K edge XANES spectra of model compounds and synthetic gypsum Samples #1 and 2; and (b) corresponding first-derivative XANES spectra.

Table 3-1 Results of As^{3+} and As^{5+} from As K edge XANES and EXAFS data

Sample	Data	Fittings	As^{3+}	As^{5+}	As^{3+}/As^{5+}
#1	XANES	FDMNES	0.26	0.74	0.35
	XANES	orpiment+scorodite	0.24	0.76	0.32
	XANES	arsenolite+scorodite	0.34	0.67	0.51
	EXAFS		0.28	0.72	0.39
#2	XANES	FDMNES	0.40	0.60	0.67
	XANES	orpiment+scorodite	0.48	0.52	0.92
	XANES	arsenolite+scorodite	0.60	0.40	1.5
	EXAFS		0.44	0.56	0.79

The As K edge XANES spectra of Samples #1 and #2 have been further analyzed by using linear combination fits (Ravel and Newville, 2005; Ravel, 2009). Specifically, two linear combination fits were made with the experimental spectra of two model compounds each to account for the observed As^{3+} and As^{5+} species: 1) orpiment and scorodite and 2) arsenolite and scorodite (Table 3-1). A third linear combination fit used theoretical As^{3+} and As^{5+} spectra calculated with the finite difference method (FDM) by using the FDMNES code of Joly (2001) (Table 3-1). My FDMNES calculations were based on the assumption that both As^{5+} and As^{3+} occupy the S^{6+} site in gypsum. Note that the average As-O interatomic distances of typical As^{5+} species (1.66 Å; Kitahama et al., 1975; Fendorf et al., 1977, Waychunas et al., 1993; Foster et al., 1998; Moldovan et al., 2003; Paktunc et al., 2004, 2008; Suess et al., 2009; Chen et al., 2009) and As^{3+} species (1.78 Å; Suess et al., 2009; Lin et al., 2011) are significantly larger than the average S-O bond distance of 1.47 Å in gypsum (Schofield et al., 1996**)**. Therefore, my FDMNES calculations included an increase of 13% and 21% from the ideal gypsum structure to account for the local expansion expected from the accommodation of As^{5+} and As^{3+} at the S site, respectively. The residual error in the As-O interatomic distance was compensated by floating ΔE_0 during fittings. Figure 3-3 shows that the fitted spectra from the FDMNES method match the experimental spectra better than those using the model compounds [i.e., a decrease in the root-mean-square-deviation (RMSD) value by 5% and 27% for Samples #1 and #2, respectively], indicating that the local structural environments of As in gypsum are probably different from those in scorodite, orpiment and arsenolite. Also, the As^{3+}/As^{5+} values of 0.35 and 0.67 for Samples #1 and #2, estimated from the FDMNES method (Table 3-1), are in better agreement with those from EXAFS (see below). FDMNES calculations for As^{3+} coordinated with 3 oxygen atoms (i.e., removing an O1 atom; see EPR results below) had been made as well and yielded similar results. However, my FDMNES modeling does not reproduce the broad peak at 11183 eV, which is known to arise from structural perturbation beyond the first-shell As-O coordination or long-range order (Chen et al., 2009).

Figure 3-4 shows the As K edge EXAFS spectra $k^3 \bullet \chi(k)$ of Samples #1 and #2 and the R-space curve fits of their Fourier transform using FEFF7 (Rehr and Albers, 2000). My R-space curve fittings were done for both a single As-O path and two As-O paths, but the latter is favored for the following two reasons: 1) the presence of two distinct S-O bonds in the host lattice (i.e.,

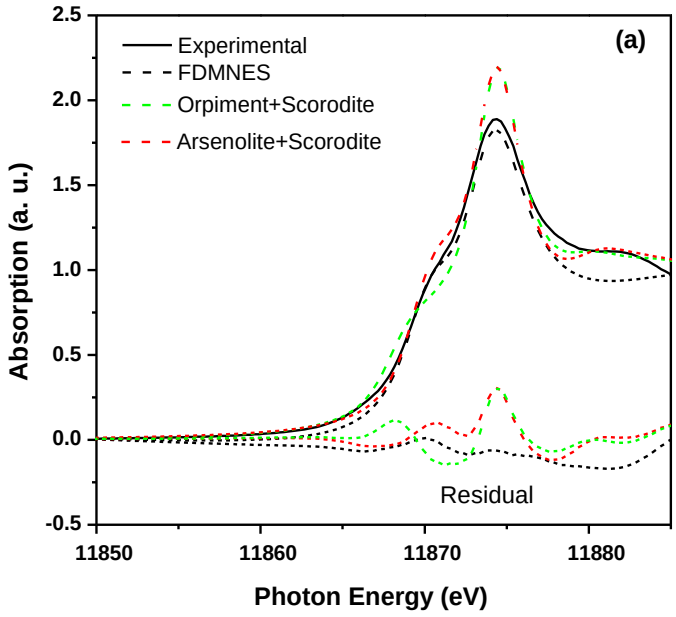

Figure 3-3a Comparison of experimental As K edge XANES spectra (solid lines) of Sample #1 with those from linear combination fits (dotted lines).

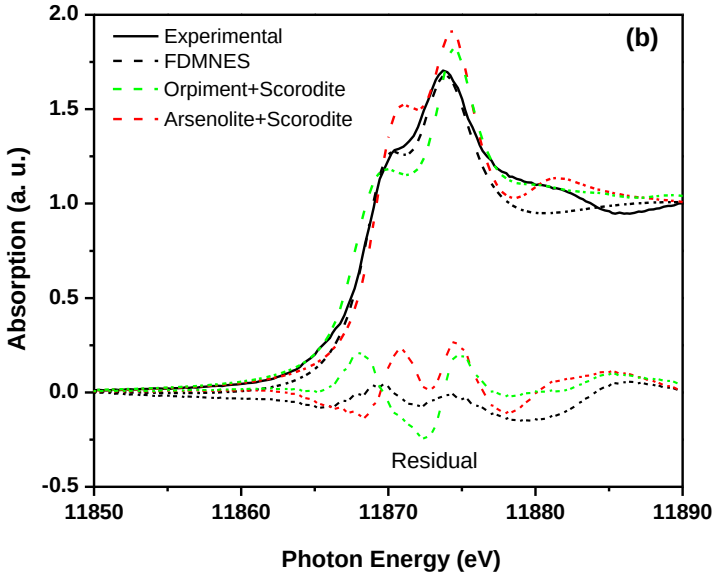

Figure 3-3b Comparison of experimental As K edge XANES spectra (solid lines) of Sample #2 with those from linear combination fits (dotted lines).

Table 3-2 Local environments of As from R-space fittings of As K edge EXAFS data

Sample	Species	CN	R_{As-O}(Å)	σ^2(Å^2)	Residual
#1	As^{5+}	2.8(±0.4)	1.67(±0.02)	0.0034(±0.0007)	4.86
	As^{3+}	1.6(±0.5)	1.76(±0.02)	0.0053(±0.0047)	
#2	As^{5+}	1.7(±0.6)	1.66(±0.02)	0.0023(±0.0027)	12.6
	As^{3+}	2.2(±1.3)	1.78(±0.02)	0.0052(±0.0032)	

Error estimations follow the recommendation by Lytle et al. (1989).

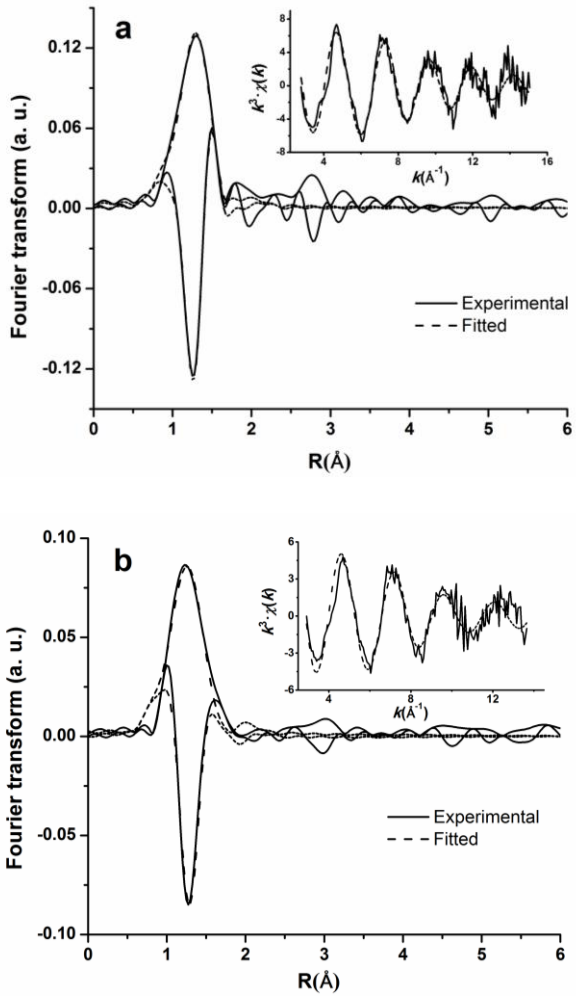

Figure 3-4 R-space curve fittings for As K edge EXAFS spectra of a) Sample #1 and b) Sample #2. The Fourier transforms of $k^3\chi(k)$ spectra were performed over the k ranges of 2.8-15.1 and 2.9-13.7 Å^{-1} and R-space fitting windows of 0.8-1.6 and 0.8-1.8 Å for Samples #1 and #2, respectively. Both the magnitude (positive envelopes) and the imaginary (oscillating parts) of the Fourier transforms are shown. Also included in inserts are the $k^3\chi(k)$ spectra in comparison with those from R-space fittings.

local symmetry constraint; Schofield et al., 1996) and 2) ~20% reduction in the calculated residual for both samples. The best-fit interatomic distances for the two arsenic species at 1.66-1.67 and 1.76-1.78 Å (Table 3-2) match closely to those of typical As^{5+} and As^{3+} (Suess et al., 2009). Also the fitted areas under the EXAFS paths for the two arsenic species at 0.39 and 0.79 for Samples #1 and #2, respectively (Table 3-1) are similar to the As^{3+}/As^{5+} values estimated from the XANES spectra (Table 3-1). Unfortunately, because of the strong correlation between the coordination number (CN) and the Debye-Waller effect (σ^2), the calculated CN and σ^2 values (Table 3-2) may not have any physical significance. Interestingly, the R-space data reveal a double peak structure between ~2.7 to 3.5 Å for both Samples #1 and #2 (Fig. 3-4), which is attributable at least partly to the As-Ca backscattering (Fernandez-Martinez et al., 2008). However, the presence of both As^{3+} and As^{5+} as well as interferences from other contributors (i.e., As-O-O, As-O-As-O, and As-O1-As-O2) make a quantitative analysis of the As-Ca backscattering difficult in this specific case.

3.2.2.2 Single-crystal X- and Q-band EPR spectra

Single-crystal EPR spectra of as-is gypsum from both samples do not have any resonance signals. EPR spectra of gamma-ray-irradiated Sample #1 reveal three sets of signals: one set of strong but complexly overlapping peaks centered at the g value of ~2.00, a second set consisting of a quartet with wide separations between ~50 and ~70 mT (Center I in Fig. 3-5a), and a third set of two quartets that have much weaker intensities and narrower separations ($\leq$~20 mT) than Center I (labeled II and III; Fig. 3-5a). The first set, confirmed by quantitative analyses of well-resolved Q-band spectra, corresponds to three previously studied paramagnetic centers: namely the SO_3^- radical with an isotropic g = 2.0025(1), the CO_3^- radical with an almost axial g [g_1 = 2.01864(1), g_2 = 2.00861(2) and g_3 = 2.00774(1)], and the O_2H^- center with its characteristic proton hyperfine structure (Alburquerque and Isotani, 1981; Kasuya et al., 1991; Ikeda and Ikeya, 1991).

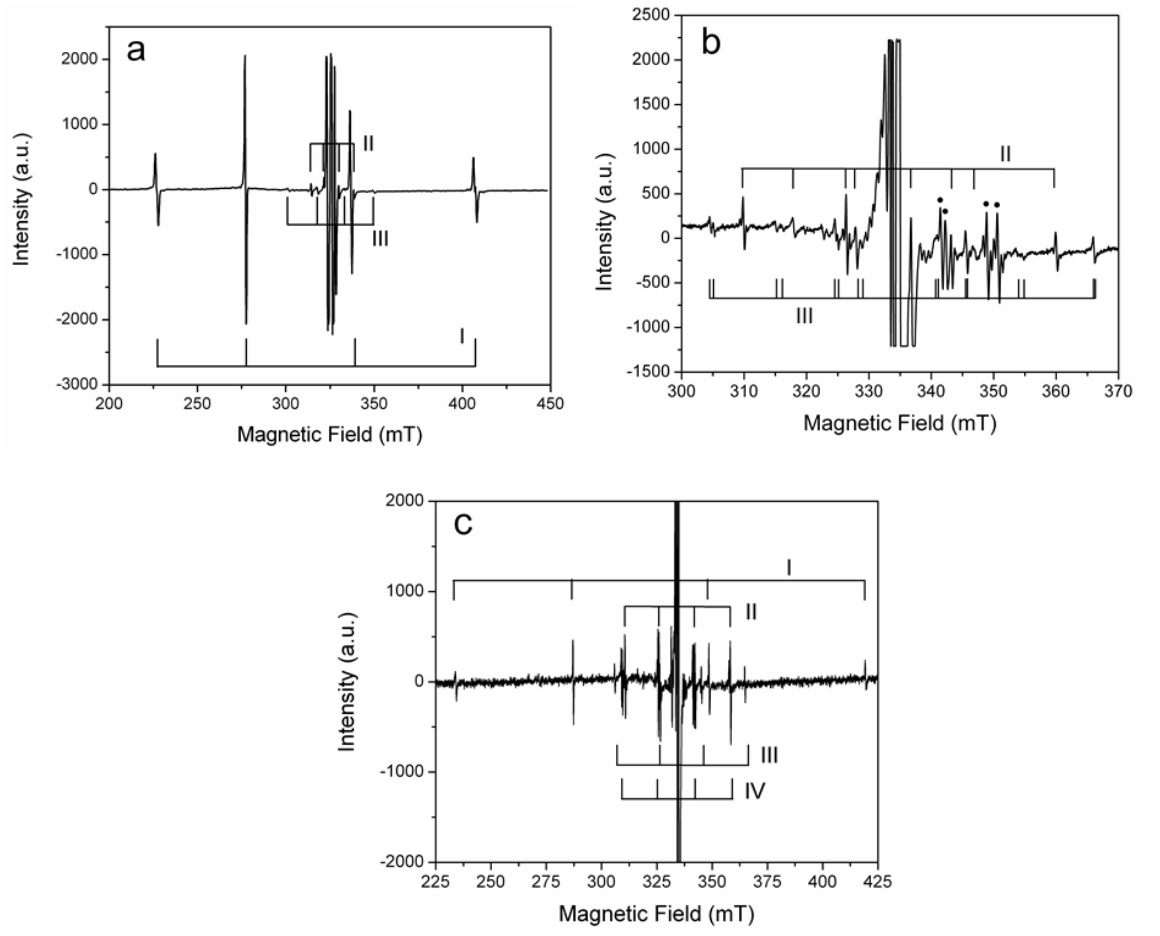

Figure 3-5 Representative single-crystal EPR spectra of gamma-ray-irradiated gypsum: (a) X-band spectrum of Sample #1 measured at **B**//**b**, illustrating the three arsenic-associated oxyradicals (labeled I, II and III); (b) X-band spectrum of Sample #1 at **B**∧**b** = ~10° showing "site" splittings of Centers II and III. Note that the lines of Center I (marked by solid circles) are accompanied by complex satellites arising from interactions with neighboring protons; and (c) X-band spectrum of Sample #2 showing the presence of an additional arsenic-associated oxyradical (IV). Also note that the intensity of Center I in Sample #2 is significantly lower than that in Sample #1.

Table 3-3 Spin Hamiltonian parameters of arsenic-associated oxyradicals in gypsum

	Matrix (Y)			k	Principal value/direction			RMSD
					Y_k	θ_k(°)	ϕ_k(°)	(mT)
Center I ($[AsO_3]^{2-}$) from X-band (~9.385 GHz) EPR at 294 K								
	2.00260(3)	0.00066(4)	0.00107(3)	1	2.00537(4)	37.1(8)	286(2)	
g		2.00367(4)	–0.00137(6)	2	2.00371(5)	71(1)	42(1)	
			2.00414(4)	3	2.00134(3)	59.1(6)	144(1)	
A(^{75}As)	1618.1(1)	–146.2(1)	–147.5(1)	1	1952.0(2)	52.7(2)	131.5(2)	
(MHz)		1654.4(2)	165.1(2)	2	1492.6(2)	39.5(6)	288(3)	0.083
			1660.7(2)	3	1488.7(2)	78.5(7)	32.7(6)	
P(^{75}As)	–2(2)	1(1)	6(1)	1	7(1)	42(3)	308(14)	
(MHz)		1(2)	–4(1)	2	2(2)	79(8)	49(6)	
			0(2)	3	–9(1)	49(2)	148(3)	
Center I ($[AsO_3]^{2-}$) from Q-band (~34.76 GHz) EPR at 294 K								
	2.00270(2)	0.00060(2)	0.00100(2)	1	2.00581(2)	33.8(2)	287(1)	
g		2.00395(2)	–0.00131(1)	2	2.00389(2)	70.9(9)	48.0(7)	
			2.00477(2)	3	2.00173(2)	63.0(5)	148.0(5)	
A(^{75}As)	1621.5(9)	–146.7(7)	–147(1)	1	1954.5(8)	52.7(2)	131.7(2)	0.111
(MHz)		1655.3(7)	165.2(6)	2	1494.6(8)	37.2(9)	308(32)	
			1663.0(8)	3	1490.7(8)	88(15)	40(11)	
Center I ($[AsO_3]^{2-}$) from X-band (~9.6 GHz) EPR at 60 K								
	2.00263	0.00045	0.00111	1	2.00552	40.5	287.5	
g		2.00372	–0.00158	2	2.00347	72.1	39.8	
			2.00395	3	2.00131	55.2	142.8	
A(^{75}As)	1591.05	–150.98	–142.70	1	1928.43	53.4	130.8	na*
(MHz)		1633.55	167.64	2	1469.01	38.1	329.3	
			1632.30	3	1459.47	99.0	47.6	
Center II ($[AsO_2^{2-}]$) from X-band (~9.386 GHz) EPR at 294 K								
	2.00765(2)	–0.00001(5)	0.00759(2)	1	2.01484(2)	46.5(2)	0.0(5)	
g		1.9958(1)	–0.0001(1)	2	1.99962(2)	43.4(2)	181(1)	
			2.00681(2)	3	1.9958(1)	90(1)	270.4(7)	
A(^{75}As)	69.5(2)	0.4(8)	–337.5(1)	1	475.5(2)	39.7(2)	180.0(2)	
(MHz)		–222.9(5)	0.0(3)	2	–211.1 (2)	50.2(2)	2.1(9)	
			194.7(2)	3	–222.9(5)	88.9(4)	271.3(5)	0.047
P(^{75}As)	6.7(3)	2.3(6)	13.4(1)	1	18.2(1)	49.7(1)	3.1(6)	
(MHz)		–9.1(4)	–0.9(4)	2	–6.9(3)	55(1)	237(1)	
			2.4(2)	3	–11.3(4)	59(1)	123(1)	

θ and ϕ are tilting angles relative to the axes z and x, respectively. (θ, ϕ) and (180-θ, 180+ϕ) are equivalent. *, RMSD is not available where spin Hamiltonian parameters were obtained by spectral simulations.

Table 3-4 Spin Hamiltonian parameters of $[AsO_3]^{2-}$ and $[AsO_2]^{2-}$ in crystalline hosts

Host	g_1	g_2	g_3	A_1/h (MHz)	A_2/h(MHz)	A_3/h(MHz)	Ref
$[AsO_3]^{2-}$							
calcite	2.00162(5)	2.00195(5)	2.00195(5)	2626.7(1)	2108.8(2)	2108.8(2)	1
$Na_2HAsO_4.7H_2O$	2.004(2)	2.005(2)	2.005(2)	2033(2)	1590(2)	1590(2)	2
KH_2AsO_4 (K)	1.996(5)	1.996(5)	1.996(5)	2573	2102	2079	3
KH_2AsO_4 (L)	1.999(5)	1.999(5)	1.999(5)	2145	1704	1693	3
KH_2AsO_4 (M)	2.000(5)	2.000(5)	2.000(5)	1852	1401	1391	3
KH_2PO_4 (b)	2.005(5)	2.005(5)	2.005(5)	2121(14)	2018(14)	2018(14)	4
KH_2PO_4 (c)	2.005(5)	2.005(5)	2.005(5)	2654(14)	2475(14)	2475(14)	4
struvite (I)	2.0064(2)	2.0085(2)	2.0058(2)	1694(6)	1523(6)	1378(6)	5
struvite (II)	2.0070(2)	2.0076(2)	2.0058(2)	1697(6)	1525(6)	1366(6)	5
betaine arsenate	2.001(4)	1.998(4)	1.998(4)	1848(10)	1447(10)	1447(10)	6
gypsum (I)	2.000134	2.00371	2.00537	1952.0	1492.6	1488.7	7
$[AsO_2]^{2-}$							
calcite	1.9910	1.9991	2.0150	614	–152	–173	8
$C_2H_6AsNaO_2$	1.967	1.995	2.012	513	–210	–238	9
gypsum (II)	1.9958	1.99962	2.01484	475.5	–211.2	–222.9	7

Reference 1, Serway and Marshall, (1966); 2, Lin and McDowell, (1964); 3, Dalal et al., (1972); 4, Murty et al., (1977); 5, Xu, (1992); 6, Pöppl et al., (1994), and 7, this study; 8, Marshall and Serway, (1969); 9, Geoffroy and Llinares, (1979).

The X- and Q-band spectra of Center I indicate a S=1/2 species involving a I=3/2 nucleus with a natural isotope abundance of ~100%. The presence of As in my gypsum crystals, together with characteristic hyperfine coupling constants (see below), allows us to identify this center as an arsenic-associated radical (Tables 3-4). The observed splitting into four lines at each nuclear transition (Fig. 3-5b) is attributed to a combination of the monoclinic crystal symmetry and twinning (i.e., an effective rotation group *D*2). The X-band spectra of Center I have an average linewidth of ~0.5 mT wide and, sometimes, are further resolved into complex multiplets (Fig. 3-5b), attributable to superhyperfine interactions with neighboring protons (see pulsed ENDOR results below).

The EPR spectra of Centers II and III are S=1/2 arsenic-associated radicals as well. Centers II and III are resolved into at most two and four lines (Fig. 3-5b), suggesting locations at a special position and a general position, respectively. The average linewidths of Centers II and III in both X- and Q-band spectra are at ~0.5 mT, similar to that of Center I. In a few orientations, Center II is accompanied by weak satellites as well (Fig. 3-5b), indicative of incompletely resolved ^{1}H superhyperfine structures similar to those of Center I. The sum of the integrated intensities of Centers II and III is ~30% of that of Center I. Unfortunately; Center III is not detectable at numerous orientations.

Single-crystal EPR spectra confirm that the gamma-ray-irradiated Sample #2 is not twinned but contains another arsenic-associated radical (IV), in addition to Centers I, II and III (Fig. 3-5c). It is noteworthy that Center I is now lower in the integrated intensity than Centers II, III and IV (Fig. 3-5c), opposite of that observed in Sample #1 (Fig. 3-5a). However, Center III remains poorly resolved at most orientations, making its quantitative analysis impossible. Similarly, Center IV, characterized by a proton superhyperfine structure (Fig. 3-5c), is not resolved at most orientations and, therefore, cannot be quantitatively analyzed either.

3.2.2.3 Spin-Hamiltonian parameters of As-associated radicals

The spin Hamiltonian for the two S=1/2 arsenic-associated radicals (I and II), ignoring the poorly resolved ^{1}H hyperfine structure, can be written as:

$$H_s = \beta_e \mathbf{S}\cdot g \cdot \mathbf{B} + \mathbf{I}\cdot\mathbf{A}\cdot\mathbf{S} + \mathbf{I}\cdot\mathbf{P}\cdot\mathbf{I} - \beta_n \mathbf{I}\cdot\mathbf{g_n}\cdot\mathbf{B}$$

Where β_e and β_n are the electronic (Bohr) and nuclear magnetons, respectively; **S** and **I** are the electron spin and nuclear spin operators, respectively; **g** is the Zeeman electron term; **B** is the external magnetic field; and **A** and **P** are the hyperfine and quadrupole terms for the ^{75}As nucleus with an isotropic g_n value of 0.959647. All data analyses, including angle corrections, optimization of spin-Hamiltonian parameters and spectral simulations, were made by use of the EPR-NMR software package of Mombourquette et al. (1996).

Optimizations of spin Hamiltonian parameters for Centers I and II were based on spectral data from Sample #1, whereas those of Sample #2 were used for verification only. The fact that Sample #1 is twinned doubles the number of experimental data points and allows us to carry out all data analyses in the effective rotation group *D*2. The selected coordinate system has the z-axis along the b-axis, while the x-axis lies in the twin plane ($\bar{1}01$) and the y-axis is normal to the twin plane. The total numbers of line-position data points for Center I were 884 and 288 at X- and Q-band frequencies, respectively. The former was reduced to 870.5 after a weighing factor of 0.1 was assigned to 15 data points involving peak overlapping. The final values of the root-mean-squares of weighed differences (RMSD) between the calculated and observed line positions for Center I were 0.083 and 0.109 mT (Table 3-3), both less than a quarter of the line widths. It is interesting to note that the data points from X-band spectra excluded one central hyperfine transition with severe overlapping (Fig. 3-6a, b), whereas my Q-band spectra measured the two central hyperfine transitions only. The fitted matrices **g** and **A** from X- and Q-band spectra are in excellent agreement (Table 3-3). The signs of the hyperfine coupling constants cannot be determined from EPR data alone. Following previous experimental studies (Serway and Marshall, 1966), I adopted a positive sign for the isotropic part of ^{75}As hyperfine for Center I (Table 3-3). Inclusion of the nuclear quadrupole tensor P resulted in minimal reduction in the RMSD value for Center I, hence a negligible effect (Table 3-3).

The total numbers of line-position data points for Center II from X-band spectra are 636 (and summer of weighing factors = 632.6). The final RMSD value is 0.047 mT (Table 3-3), also less than a quarter of the average linewidth. Following previous experimental studies (Marshall and Serway, 1969), I adopted mixed signs for the principal A values of Center II. Unlike Center I, the best-fitted nuclear quadrupole parameter for Center II is considerable (Table 3-3). Unfortunately, this center is not resolved in most Q-band spectra; hence fitting of its spin

Hamiltonian parameters on the basis of Q-band data was not possible.

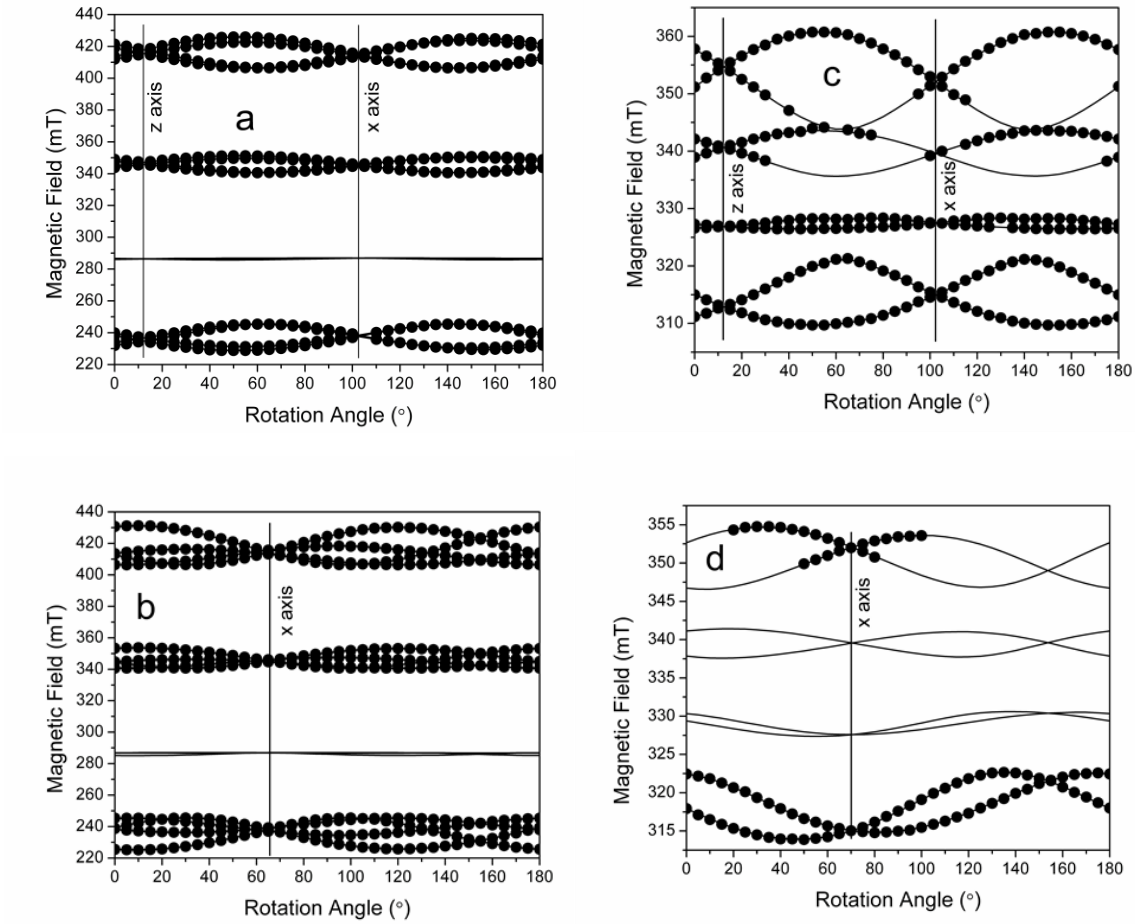

Figure 3-6 Representative angular dependences of line positions (i.e., roadmaps) of Centers I (a and b) and II (c and d) in the twinned crystal of Sample #1: a and c) approximately parallel to the {010} cleavage plane, and b and d) approximately parallel to the (100) crystal face. Experimental axes are located only approximately. Note that data points for the lower central hyperfine transition of Center I in a) and b) are not included owing to severe overlapping among themselves and that data points for both central hyperfine transitions of Centre II in d) are not available owing to overlapping with those of other centers.

The fitted principle g values and A(^{75}As) hyperfine constants identify Centers I and II as the $[AsO_3]^{2-}$ radical and the $[AsO_2]^{2-}$ radical, respectively (Table 3-4). The most salient feature of the $[AsO_3]^{2-}$ radical is that the orientations of the g_2 and A_1 axes are only slightly non-coincident, with the latter being approximately along the S-O1 bond direction (55.9º, 136.1º). The $[AsO_2]^{2-}$ radical has the g_1, A_2 and P_1 axes approximately coincident along the S-O2 bond direction (55.9º, 1.1º), and the g_2 and A_1 axes approximately perpendicular to an O1-S-O2 plane.

3.2.2.4 Proton superhyperfine structures from pulsed ENDOR

Mims ENDOR spectra (Fig. 3-7) show the presence of numerous small proton splittings, of which four have A_{major} >4 MHz (Table 3-5). Each S atom in gypsum has five pairs of nearby water molecules, with distances from 3.493 to 3.835, 4.030, 4.368, and 4.385 Å, respectively (Fig. 3-1; Schofield et al., 1996). Each water molecule has two non-equivalent protons, H1 and H2, resulting in a total of 10 distinct hyperfine couplings. Moreover, the $[AsO_3]^{2-}$ center (Center I) is expected to break the C_2 symmetry of the S site and thus, one expects to see 20 distinct proton couplings for the ten water molecules. Simulation of Mims ENDOR spectra first only included the four protons with the largest couplings and assumed axially symmetric hyperfine couplings. This was found to give rather poor fits unless a rhombic component was included (Table 3-5). Also, the splitting of one or more of the four protons at many orientations is less than a couple of MHz. To confirm the fit of these four protons, 16 smaller couplings were added with initial axial hyperfine matrices calculated using the point dipole model. This produced only a rough fit for the ENDOR patterns. This could be improved by allowing the 16 smaller couplings to vary, first assuming axial hyperfine matrices and then allowing a rhombic component for protons with the expected A_{major} >1.5 MHz.

Table 3-5 summarized the best-fit hyperfine coupling constants for the 10 pairs of protons. The C_2 symmetry is clearly broken; however, the direction of A_{major} is rotated approximately 180° around the b-axis for each pair. For the $[AsO_3]^{2-}$ center this loss of the C_2 symmetry can be attributed to the removal of an O1 atom of the SO_4 tetrahedron, with the unpaired spin occupying the p orbital oriented along the original S-O1 bond. Not only is the unpaired spin distributed asymmetrically with respect to the C_2 axis for Center I, but the removal of an O1 atom is

Table 3-5 ^{1}H superhyperfine constants of the $[AsO_3]^{2-}$ center in gypsum from ENDOR and comparison with S–H data from neutron diffraction experiments

Proton	Principal value		Principal direction		As–H‡		S–H§		Proton	Principal value		Principal direction		As–H‡		S–H§	
	A_k	**A**/h MHz)	θ (°)	ϕ (°)	(Å)	θ (°)	ϕ (°)	(Å)		A_k	**A**/h (MHz)	θ (°)	ϕ (°)	(Å)	θ (°)	ϕ (°)	(Å)
	A_1	1.97	66.8	234.7						A_1	1.84	84.2	34.3				
H1’	A_2	-0.33	102.6	319.2	4.37	71.2	223.8	3.977	H1”	A_2	-1.08	108.0	306.2	4.26	71.2	43.8	3.977
(1)	A_3	-1.44	26.79	22.8					(1)	A_3	-1.42	161.0	107.1				
	A_1	2.36	51.6	222.8						A_1	2.23	54.3	32.9				
H2’	A_2	-1.47	141.6	224.6	3.99	49.7	216.0	3.898	H2”	A_2	-1.25	67.7	140.0	4.09	49.7	36.0	3.898
(1)	A_3	-1.33	89.1	313.5					(1)	A_3	-1.25	44.1	255.0				
	A_1	5.59	73.5	256.6						A_1	4.79	70.0	72.5				
H1’	A_2	-2.90	97.9	168.9	3.02	63.8	278.6	2.906	H1”	A_2	-2.65	109.9	350.1	2.95	63.8	98.6	2.906
(2)*	A_3	-4.56	161.6	283.5					(2)*	A_3	-3.58	151.2	121.1				
	A_1	1.90	56.5	269.4						A_1	2.38	51.6	87.9				
H2’	A_2	-0.91	126.1	208.3	4.39	53.7	271.3	4.258	H2”	A_2	-1.30	38.5	262.4	3.95	53.7	91.3	4.258
(2)	A_3	-0.91	126.2	330.5					(2)	A_3	-1.69	87.3	355.8				
	A_1	2.01	19.3	343.0						A_1	2.14	19.9	156.7				
H1’	A_2	-0.92	91.1	256.1	4.30	21.4	0.5	4.267	H1”	A_2	-1.03	84.7	261.4	4.21	21.4	180.5	4.267
(3)	A_3	-1.04	109.3	346.5					(3)	A_3	-1.09	70.9	353.2				
	A_1	6.19	22.3	332.7						A_1	5.14	30.7	156.0				
H2’\	A_2	-1.59	111.0	312.2	3.01	28.7	325.9	3.124	H2”	A_2	-3.17	60.0	349.5	3.02	28.7	145.9	3.124
(3)*	A_3	-3.54	97.1	44.9					(3)*	A_3	-3.94	95.9	76.1				
	A_1	1.14	70.9	333.9						A_1	1.59	73.3	145.2				
H1’	A_2	-0.87	160.8	341.3	4.91	73.8	323.9	4.602	H1”	A_2	-0.85	16.9	316.2	4.61	73.8	143.9	4.602
(4)	A_3	-0.87	87.7	64.7					(4)	A_3	-0.85	87.5	54.5				
	A_1	1.36	58.1	342.0						A_1	2.25	60.4	162.7				
H2’	A_2	-0.60	121.9	274.8	4.96	59.4	335.7	4.946	H2”	A_2	-0.72	43.4	35.8	5.04	59.4	155.7	4.946
(4)	A_3	-0.60	131.7	38.4					(4)	A_3	-0.72	118.5	90.7				
	A_1	2.16	23.7	1.1						A_1	2.43	19.4	202.1				
H1’	A_2	-1.14	68.4	155.4	4.23	23.7	0.5	3.960	H1”	A_2	-1.31	86.8	102.8	3.91	23.7	180.5	3.960
(5)	A_3	-0.85	80.7	249.1					(5)	A_3	-1.78	109.1	191.7				
	A_1	1.09	14.9	12.7						A_1	1.26	16.8	190.6				
H2’	A_2	-0.57	75.6	207.9	5.24	23.2	23.9	5.287	H2”	A_2	-0.45	105.7	169.2	5.19	23.2	203.9	5.287
(5)	A_3	-0.57	93.8	297.0					(5)	A_3	-0.45	95.8	260.8				

Labels of hydrogen atoms are same as those in Figure 1. θ and ϕ are tilting angles relative to the axes z and x, respectively. ‡, As–H distances calculated from the point-dipole model; §, S–H directions and distances from neutron diffraction experiments of Schofield et al. (1996); *, protons with the four largest hyperfine splittings.

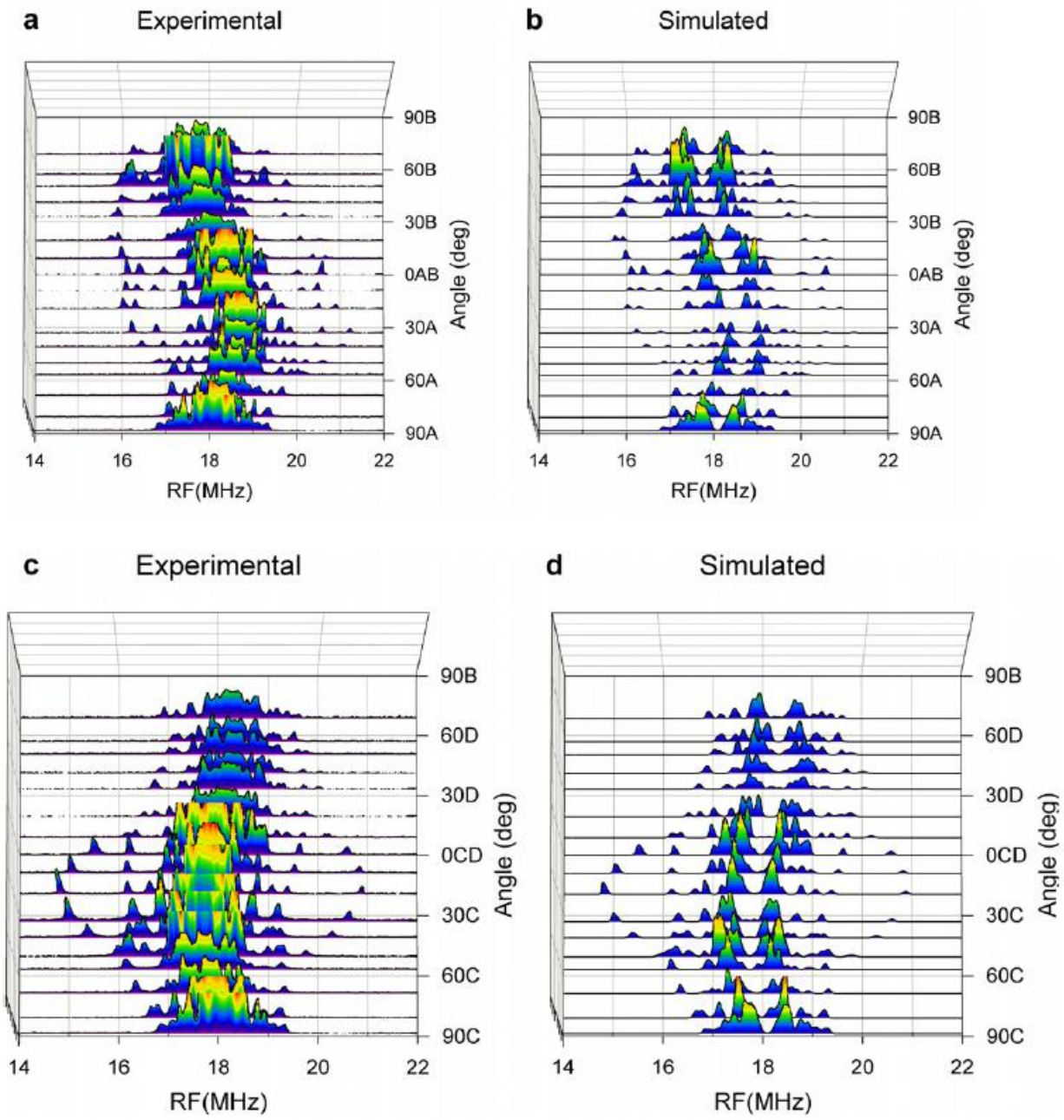

Figure 3-7 Stacked plots of experimental and simulated Mims ENDOR spectra as a function of rotation angles in one rotation plane, showing two parts of the twinned crystals (upper and lower panels; A, B, C and D represent the four magnetic sites in the effective rotation group D_2). Note that spectra simulations included 20 protons (Table 3-5), whereas the central component arising from interactions with more distant protons was not considered.

expected to change the pattern of hydrogen bonding around the center. Changes in hydrogen bonding should affect H1(2) and H2(3) the most, because the O1-H1(2) and O1-H2(3) distances are only 1.85 and 1.94 Å, respectively. Table 3-5 shows that the A_{iso} values and the rhombic splittings differ significantly between H1′(2) and H1″(2) and between H2′(3) and H2″(3). Simulations (Fig. 3-7) show that the all hyperfine peaks/patterns can be fairly well accounted for using the 20 proton couplings, although there is clearly a significant component in the center of the pattern attributable to more distant protons with hyperfine couplings <1 MHz. Also, because of the larger number of protons with similar couplings the uncertainty in the smaller couplings is expected to be not much less than a few tenths of 1 MHz. Despite the uncertainty in the smaller couplings, Table 3-5 shows that the magnitude and direction of hyperfine coupling for all 20 protons correlate well with the crystal structure of gypsum (Schofield et al., 1996), confirming the assignment of the $[AsO_3]^{2-}$ center as a substitution of As for S and a removal of one oxygen atom. It is also interesting to note that protons with the four largest couplings do not arise from the nearest water. Rather two of the protons correspond to the H1 proton on the pseudo-C_2 pair of $H_2O(2)$ and the other two protons correspond to the H2 proton on the pseudo-C_2 pair of $H_2O(3)$.

3.2.2.5 Formation of the $[AsO_3]^{2-}$ and $[AsO_2]^{2-}$ centers

The A(^{75}As) hyperfine constants of the $[AsO_3]^{2-}$ center can be decomposed into an isotropic (*a*) and an unaxial component (*b*): a = 1644.4 MHz and b = 153.8 MHz, yielding ~11% and ~46% of the unpaired electron on the As 4*s* and 4p_z orbitals. The direction of the unique A(^{75}As) axis shows that the 4p_z orbital is along the S-O1 bond direction (Table 3-3). Therefore, the $[AsO_3]^{2-}$ center represents electron trapping on the central As^{5+} ion of a substitutional $(AsO_4)^{3-}$ group after removal of an O1 atom. This structural model has been confirmed by the detailed analysis of ^{1}H superhyperfine structures from pulsed ENDOR spectra (Table 3-5).

The substitution of $(AsO_4)^{3-}$ for $(SO_4)^{2-}$ in gypsum may be written as:

$$(AsO_4)^{3-} + M^+ \leftrightarrow (SO_4)^{2-} \qquad (3\text{-}1),$$

$$(AsO_4)^{3-} \rightarrow (SO_4)^{2-} \qquad (3\text{-}2).$$

Reactions 3-1 and 3-2 differ in the presence of a monovalent cation (e.g., Na^+ and H^+) as a charge compensator at a neighboring interstitial site in the former, whereas the latter does not have an immediate charge compensator. My ENDOR results show that all proton superhyperfine

structures arise from interactions with ^{1}H nuclei at normal lattice sites (Table 3-5) and that there is no evidence for ^{23}Na, ^{1}H or any other ENDOR-active nuclei at interstitial sites, casting doubt on Reaction 3-1. On the other hand, there is abundant literature for heterovalent substitutions without an immediate charge compensator (e.g., Pan et al., 2011). Another alternative is the presence of both $(AsO_3)^{-}$ and $(AsO_4)^{3-}$ in synthetic gypsum to maintain the overall neutrality, where the former is the direct precursor to the $[AsO_3]^{2-}$ radical by electron trapping during gamma-ray irradiation.

The A(^{75}As) hyperfine constants of the $[AsO_2]^{2-}$ center suggest that ~71% of the unpaired electron is localized on the As $4p_z$ orbital. The orientations of the principle g, A and P axes show that the $[AsO_2]^{2-}$ center involves electron trapping on a substitutional As^{3+} ion at the S site. The location of As^{3+} at the S site is also supported by the magnitude of the ^{1}H syperhyperfine splittings (Fig. 3-5b). Specifically, this $[AsO_2]^{2-}$ center probably has a diamagnetic precursor of the pyramidal $(AsO_3)^{3-}$ type without an O1 atom. Gamma-ray irradiation may have been responsible for the removal of an O2 atom and trapping an unpaired electron in the As $4p_z$ orbital directed towards the missing O2 atom. It is noteworthy that Centers III and IV have similar magnitudes of A(^{75}As) hyperfine constants and most likely represent variants of the $[AsO_2]^{2-}$ center (i.e., different distortions of the precursors $(AsO_3)^{3-}$ relative to the original $(SO_4)^{2-}$ group). By analogy with As^{5+} discussed above, As^{3+} in gypsum may occur as both $(AsO_2)^{-}$ and $(AsO_3)^{3-}$ species, where the former is the precursor to the $[AsO_2]^{2-}$ radical by electron trapping.

The presence of both As^{5+} and As^{3+} in Sample #1 synthesized with $Na_2HAsO_4 \bullet 7H_2O$ as the source of arsenic was puzzling and was the motivation for my synthesis of Sample #2. Interestingly, synchrotron XAS and single-crystal EPR spectra show that Sample #2 synthesized with the $NaAsO_2$ standard solution also contains mixed As^{3+} and As^{5+} but, as expected, has a significantly higher As^{3+}/As^{5+} value than Sample #1. Possible explanations for the presence of mixed As^{5+} and As^{3+} in Samples #1 and #2 include 1) impure starting materials and 2) unknown electron-transfer reactions involving trace-metal impurities or bacterial activity during synthesis experiments (cf., Reeder et al., 2006). Indeed, bacterial activity during my prolonged synthesis experiments in open U-tubes cannot be ruled out.

3.3 Arsenic uptake in gypsum as a function of pH

3.3.1 Materials and experimental methods

Powder samples of gypsum have been precipitated by first adding 20 mL of 0.5 M calcium chloride dihydrate ($CaCl_2 \cdot 2H_2O$) into a beaker, then a mixture of 20 mL of 0.5 M ammonium sulfate [$(NH_4)_2SO_4$] together with 0.04 M sodium hydrogen arsenate heptahydrate ($Na_2HAsO_4 \cdot 7H_2O$) were poured into the beaker while stirring. The pH values at various runs were adjusted to 2, 4, 7.5, 9, 12 and 14 by adding the ammonium sulfate solution. All six solutions were vigorously stirred for 7 days. After reaction, the pH values of residual fluids were measured which were consistent with the starting values. The solid samples were centrifuged and dried at 60 °C in an oven, and then were measured by powder X-ray diffraction analysis with CuKα1 radiation (λ = 1.54056 Å) at 45 kV and 40 mA. Samples were also carbon-coated for examination on a JEOL 840A scanning electron microscope (SEM).The concentrations of arsenic in each sample were analyzed by using Inductively Coupled Plasma Mass Spectrometry (ICPMS). All powder samples were weighted, irradiated at room temperature in a ^{60}Co cell, with a dose rate of ~460 Gy/h, for 2 and 6 days, and measured at room temperature for EPR spectra by using a Bruker EMX instrument. Arsenic K-edge XANE data for six powder samples was collected in the fluorescence mode at room temperature.

3.3.2 Results and discussion

Powder X-ray diffraction analyses show that only a single gypsum phase is present in each of the six runs (Fig. 3-8). The crystallinity of gypsum, as defined by the full width at half maximum (FWHM) of the well resolved reflection at 2θ = ~20.5°, is high at low pH values but becomes poorer at high pH values, particularly at pH = 12 and 14. The apparent decrease in crystallinity of gypsum with the increase in pH is also clearly observed in the crystal sizes revealed by SEM images (Fig. 3-9).

Figure 3-10 illustrates the concentrations of total arsenic as a function of pH. It is interesting to note that the levels of As in these gypsum samples from runs at pH = 2-7.5 are

broadly similar to that observed in the single crystals from the gel diffusion technique. Considering the high crystallinities (Figs. 3-8 and 3-9), it reasonable to conclude that As in these samples obtained at low pH values is also dominantly lattice bound. The exceedingly high As contents in the products obtained from runs at pH = 12 and 14 are interesting but are unlikely to incorporate in the gypsum structure (see below), especially in view of the poor crystallinity from PXRD and SEM.

All six samples of synthetic gypsum have similar powder EPR spectra, which closely match those simulated from the spin Hamiltonian parameters from the single-crystal EPR study (Fig. 3-11). These EPR spectra show that both As^{3+} and As^{5+} are present in the powder samples as well. Figure 3-12 shows that the intensity of the third peak of Center I increases with the pH values from 2 to 7.5. This trend is similar to that obtained from ICPMS analyses, supporting a significant effect of pH on the uptake of arsenic in gypsum.

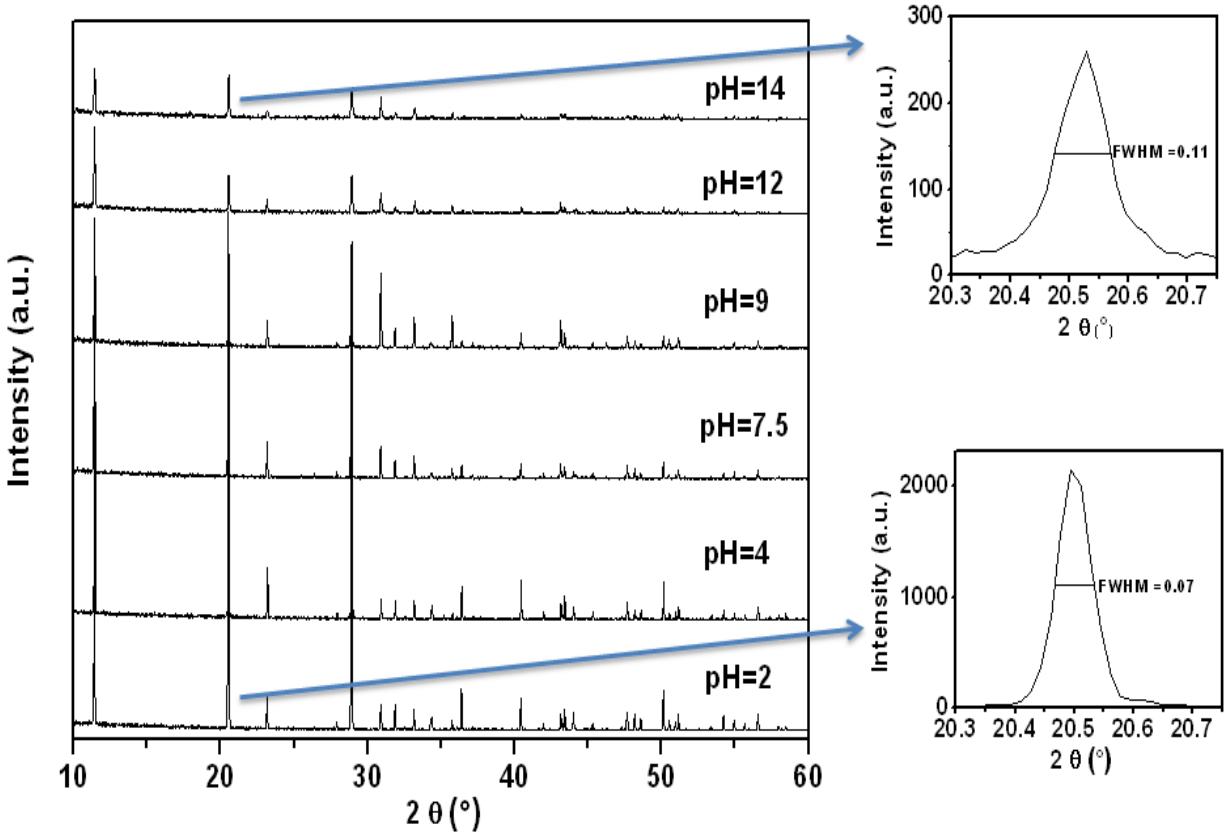

Figure 3-8 Powder X-ray diffraction patterns of gypsum formed at different pH values

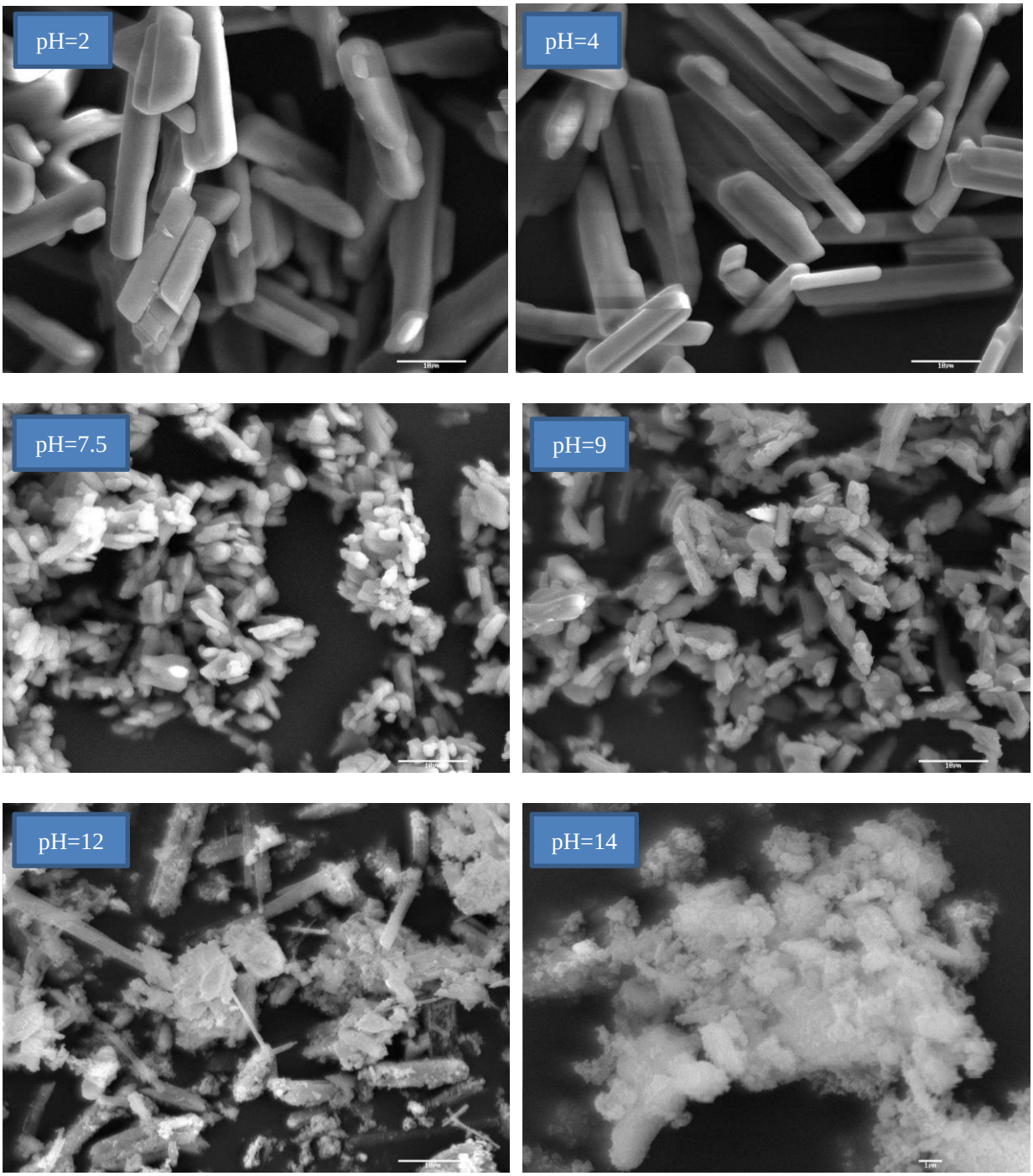

Figure 3-9 SEM images showing the sizes of gypsum crystals at different pH values

Interestingly, the intensities of the third peak of Center I in the powder EPR spectra of the two samples from runs at pH = 12 and 14 do not show further increase relative to those of the low pH samples. This result suggests that the anomalously high As contents in gypsum from runs

at pH = 12 and 14 cannot be attributed entirely to lattice substitutions. Instead, other mechanisms such as surface adsorption may be dominant here.

Figure 3-11 also shows that the center II, albeit present, is subordinate to the center I, indicating very low concentrations of As^{3+} in these samples (e.g., the relative intensity of Center II is less than 5% of that of Centers I at pH = 9). Figure 3-13 shows that the intensity of the center II also increases with pH in the range from 2 to 7.5 and that further increase is not observed in the two samples obtained from runs at pH = 12 and 14, again suggesting that surface sorption is probably responsible for the anomalous high As contents at high pH values.

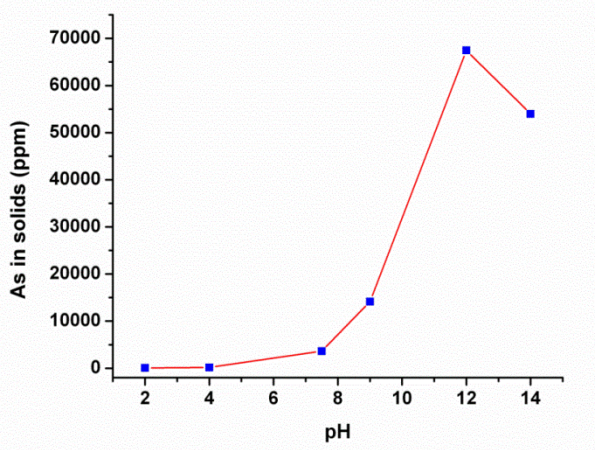

Figure 3-10 ICPM results of total arsenic in synthetic gypsum samples (both sorption and substitution)

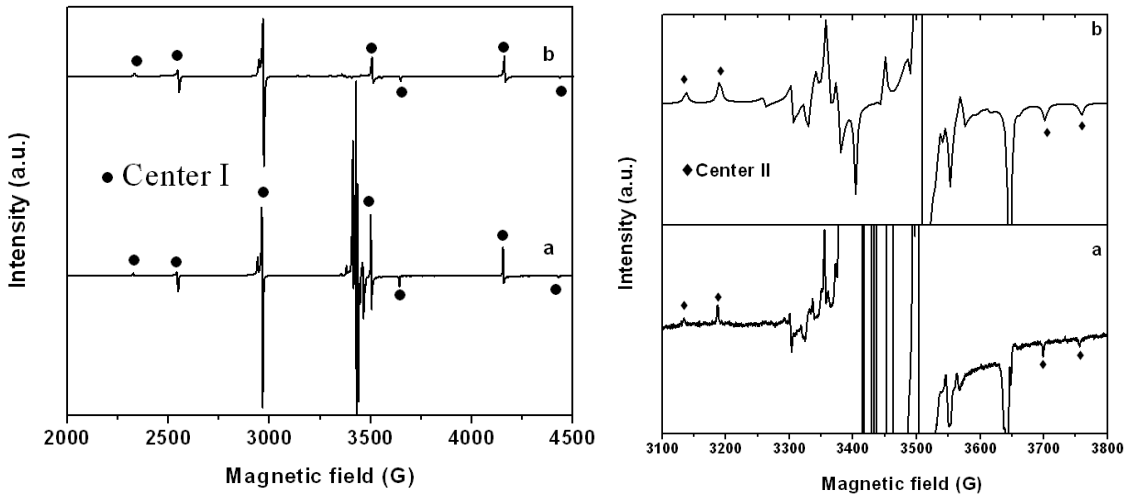

Figure 3-11 Comparison of powder EPR spectra in gypsum at pH=9(a) with simulated spectra (b) of the centers I and II

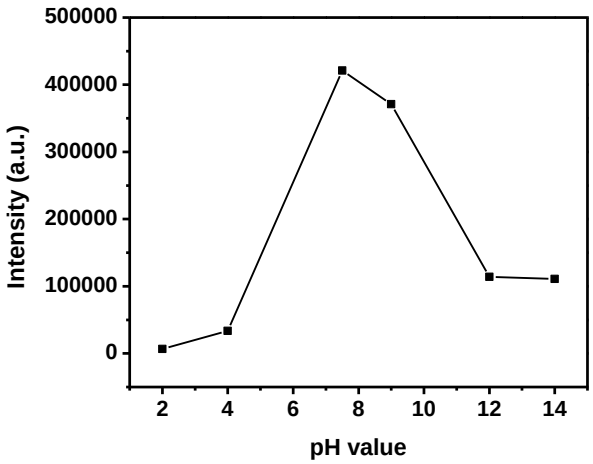

Figure 3-12 The intensity of the third peak of the center I (As^{5+}) in powder gypsum samples at different pH values

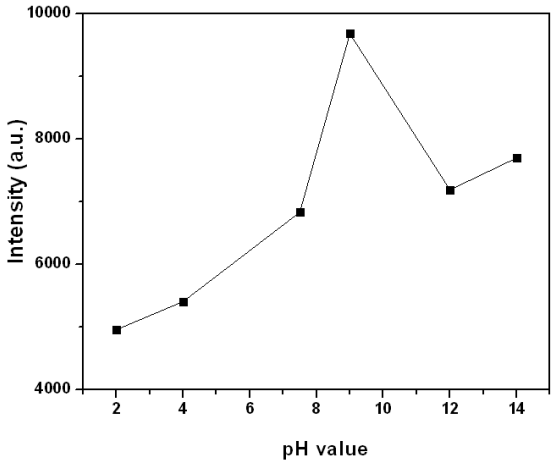

Figure 3-13 The intensity of the third peak of the center II (As^{3+}) in powder gypsum samples at different pH values

Unlike the EPR results, As^{5+} is the only species observed in the As K-edge XANES spectra (Fig. 3-14). This is probably attributable to low concentrations of As^{3+} in these powder samples synthesized using a shorter duration than the single crystal samples, which are undetectable by the XANES technique. This is consistent with results from other studies that the sensitivity of X-ray absorption spectroscopy is expected to be much lower than that of the EPR technique (Li et al., 2013).

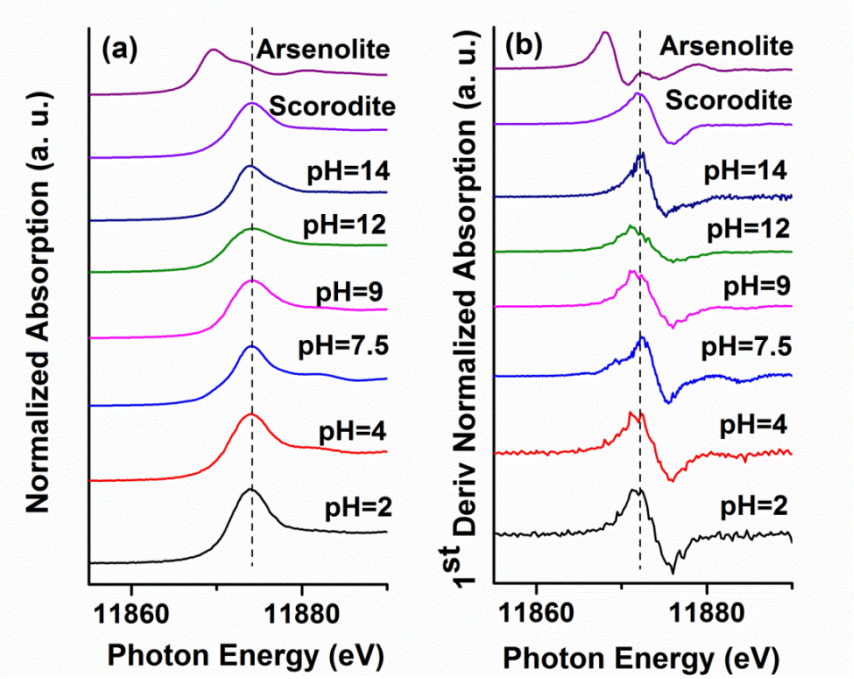

Figure 3-14 (a)As K edge XANES spectra of model compounds and synthetic gypsum samples and (b) corresponding first-derivative XANES spectra.

3.4 Implications for remediation of As contamination

My synchrotron XAS and single-crystal EPR results provide evidence for incorporation of both As^{3+} and As^{5+} in gypsum, confirming the observations of Fernandez-Martinez et al. (2006, 2008) for accommodation of As^{5+} at the S site. To the best of my knowledge, this is the first documentation of As^{3+} substitution for S^{6+}. Moreover, my angle dependence data from single-crystal EPR spectra provides unambiguous evidence for lattice-bound As^{3+} and As^{5+} at the S site in gypsum. Furthermore, results from crystalline powder samples with pH value from 2-14 show that uptake of arsenic in gypsum is pH dependent. At low pH value, substitution is dominant, whereas at high pH value, sorption might be dominant.

Therefore, gypsum adds to the growing list of rock-forming minerals (e.g., apatite, calcite, hemimorphite and jarosite) that are capable of accommodating significant amounts of As in their crystal lattices, with potential application for immobilization and removal of As contamination in

surface environments (Bothe and Brown, 1999; Savage et al., 2005; Di Benedetto et al., 2006; Zhu et al., 2006; Blanchard et al., 2007; Lee et al., 2009; Drahota and Filipi, 2009; Mao et al., 2010; Bardelli et al., 2011). In this context, two major advantages of gypsum are notable: 1) a major phase in the mining and milling processes of various mineral deposits (Jamieson, 2011) and 2) its formation and stability in aqueous solutions at ambient conditions. Therefore, gypsum is expected to exert important controls on the stability and bioavailability of As in mine tailings and surrounding areas, particularly those associated with borate, phosphate and uranium deposits. For example, my results can now explain the behavior of As in Turkish arsenical borogypsum wastes and their cement products reported by Alp et al. (2009), who noted that As is not readily leachable from those materials. Also, gypsum is potentially useful for immobilization and removal of arsenic contamination from aqueous solutions by co-precipitation. One disadvantage of gypsum is its considerable solubility in water (Tanji, 1969; Harvie et al., 1984; Wollmann and Voigt, 2008), hence potential for secondary contamination from dissolution. However, dissolution of gypsum can be minimized by carefully monitoring and controlling the Ca^{2+} and SO_4^{2-} concentrations, ionic strength, and pH, which are important factors in controlling the solubility of this mineral at ambient conditions (Tanji, 1969; Harvie et al., 1984; Wollmann and Voigt, 2008).

3.5 References

Albuquerque A. R. P and Isotani S. (1982) The EPR spectra of X-ray irradiated gypsum. *Journal of the Physical Society of Japan* **51**, 1111-1118.

Alp I., Deveci H., Süngün Y. H., Yazici E. Y., Savaş M. and Demirçi S. (2009) Leachable characteristics of arsenical borogypsum wastes and their potential use in cement production. *Environmental Science & Technology* **43**, 6939-6943.

Andruzzi L., Nakano M., Nilges M. J. and Blackburn N. J. (2005) Spectroscopic studies of metal binding and metal selectivity in *Bacillus subtilis* BSco, a homologue of the yeast mitochondrial protein sco1p. *Journal of the American Chemical Society* **127**, 16548–16558.

Bardelli F., Benvenuti M., Costagliola P., Di Benedetto F., Lattanzi P., Meneghini C., Romanelli, M. and Valenzano L. (2011) Arsenic uptake in natural calcite: An XAS study. *Geochimica*

et Cosmochimica Acta **75**, 3011-3023.

Barquera B., Ramirez-Silva L., Morgan J. E. and Nilges M. J. (2006) A new flavin radical signal in the Na^+-pumping NADH: quinone oxidoreductase from *Vibrio cholerae*: an EPR/ENDOR investigation of the role of the covalently bound flavins in subunits B and C. *Journal of Biological Chemistry* **281**, 36482–36491.

Bothe J.V. and Brown P. W. (1999) Arsenic immobilization by calcium arsenate formation. *Environmental Science & Technology* **33**, 3806-3811.

Chen N., Jiang D. T., Cutler J., Kotzer T., Jia Y., Demopoulos G. P. and Rowson J. (2009) Structural characterization of poorly-crystalline scorodite, iron(III)-arsenate co-precipitates and uranium mill neutralized raffinate solids using X-ray absorption fine structure spectroscopy. *Geochimica et Cosmochimica Acta* **73**, 3260-3276.

Çolak M., Gemici Ü. and Tarcan G. (2003) The effects of colemanite deposits on the arsenic concentrations of solid and groundwater in Igdekoy-Emet, Kutahya, Turkey. *Water, Air, & Soil Pollution* **149**, 127-143.

Dalal N. S., Dickinson J. R. and McDowell C. A. (1972): Electron paramagnetic resonance studies of X-irradiated KH_2AsO_4, KD_2AsO_4, RbH_2AsO_4, RbD_2AsO_4, CsH_2AsO_4, $NH_4H_2AsO_4$, and $ND_4D_2AsO_4$ (ferroelectrics and antiferroelectrics). *Journal of Chemical Physics* **57**, 4254-4265.

Delfini M., Ferrini M., Manni A., Massacci P. and Piga L. (2003) Arsenic leaching by Na_2S to decontaminate tailings coming from colemanite processing. *Minerals Engineering **16***, 45–50.

Di Benedetto F., Da Pelo S., Caneschi A. and Lattanzi P. (2011) Chemical state of arsenic and copper in enargite: evidences from EPR and X-ray absorption spectroscopies, and SQUID magnetometry. *Neues Jahrbuch für Mineralogie Abhandlungen* **188**, 11-19.

Di Benedetto F., Costagliola P., Benvenuti M., Lattanzi P., Romanelli M. and Tanelli G. (2006) Arsenic incorporation in natural calcite lattice: Evidence from electron spin echo spectroscopy. *Earth and Planetary Science Letters* **246**, 458–465.

Donahue R. and Hendry M. J. (2003) Geochemistry of arsenic in uranium mine mill tailings, Saskatchewan, Canada. *Applied Geochemistry* **18**, 1733-1750.

Drahota P. and Filipi M. (2009) Secondary arsenic minerals in the environment: A review. *Environment International* **35**, 1243-1255.

Fendorf S., Eick M. J., Grossl P. and Sparks D. L. (1977): Arsenate and chromate retention mechanisms on goethite. 1. Surface structure. *Environmental Science & Technology* **31**, 315-320.

Fernández-Martínez A., Roman-Ross G., Cuello G. J., Turrillas X., Charlet L., Johnson M. R. and Bardelli F. (2006) Arsenic uptake by gypsum and calcite: Modelling and probing by neutron and X-ray scattering. *Physica B* **385-286**, 935-937.

Fernández-Martínez A., Charlet L., Cuello G. J., Johnson M. R., Roman-Ross G., Bardelli F. and Turrillas X. (2008) Arsenate incorporation in gypsum probed by neutron, X-ray scattering and DFT modeling. *Journal of Physical Chemistry* **A112**, 5159-5166.

Foster A. L., Brown G. E., Tingle T. N. and Parks G. A. (1998) Quantitative arsenic speciation in mine tailings using X-ray absorption spectroscopy. *American Mineralogist* **83**, 553-568.

Gemici Ü., Tarcan G., Helvaci C. and Somay A. M. (2008) High arsenic and boron concentrations in groundwaters related to mining activity in the Bigadic borate deposits (Western Turkey). *Applied Geochemistry* **23**, 2462-2476.

Geoffroy M. and Llinares A. (1979) Etude par resonance paramagnétique électronique des radicaux piégés dans un monocristal de diméthylarsinate de sodium irradié aux rayons X. *Helvetica Chimica Acta* **62**, 1605-1613.

Harvey M. C., Schreiber M. E., Rimstidt J. D. and Griffith M. M. (2007) Scorodite dissolution kinetics: Implications for arsenic release. *Environmental Science & Technology* **40**, 6709-6714.

Harvie C. E., Moeller N. and Weare J. H. (1984) The prediction of mineral solubilities in natural waters: The Na-K-Mg-Ca-H-Cl_SO4-OH-HCO_3-CO_3-CO_2-H_2O system to high ionic strengths at 25 ºC. *Geochimica et Cosmochimica Acta* **48**, 723-751.

Helvaci C. and Alonso R. N. (2000) Borate deposits of Turkey and Argentina: A summary and geological comparison. *Turkish Journal of Earth Sciences* **9**, 1-27.

Ikeda S. and Ikeya, M. (1992) Electron spin resonance signals in natural and synthetic gypsum: An application of ESR to the age estimation of gypsum precipitates from the San Andreas fault. *Japanese Journal of Applied Physics* **31**, L136-L138.

Jamieson H. E. (2011) Geochemistry and mineralogy of solid mine waste: Essential knowledge for predicting environmental impact. *Elements* **7**, 381-386.

Jiang D. T., Chen N. and Sheng W. (2007) CLS 06ID-1: A Wiggler-based Hard X-ray

Spectroscopy Beamline. *AIP Proceedings* **879**, 800-803.

Joly Y. (2001) X-ray absorption near edge structure calculations beyond the muffin-tin approximation. *Physical Review B* **63**, 125120.

Kasuya M., Brumby M. S. and Chappell J. (1991) ESR signal in gypsum single crystals: implications for ESR dating. *Nuclear Tracks and Radiation Measurements* **18**, 329.

Lee Y. J., Stephens P. W., Tang Y., Li W., Phillips B. L., Parise J. B. and Reeder R. J. (2009) Arsenate substitution in hydroxylapatite: Structural characterization of the $Ca_5(P_xAs_{1-x}O_4)_3OH$ solid solution. *American Mineralogist* **94**, 666-675.

Li, R., Lin, J., Nilges, M. J., Chen, N., and Pan, Y. (2013). Arsenic speciation in danburite ($CaB_2Si_2O_8$): A synchrotron XAS and single-crystal EPR study. *European Journal of Mineralogy* (in press).

Lin J., Pan Y., Chen N., Mao M., Li R. and Feng R. (2011) Arsenic incorporation in colemanite from borate deposits: Data from ICP-MS, μ-SXRF, XAFS and EPR analyses. *Canadian Mineralogist* **49**, 809-822.

Lin W. C. and McDowell C. A. (1964) Electron spin resonance of an X-ray irradiated single crystal of disodium hydrogen arsenate, $Na_2HAsO_4.7H_2O$. *Molecular Physics* **7**, 223-234.

Lytle F. W., Sayers D. E. and Stern E. A. (1989) Report of the international workshop on standards and criteria in X-ray absorption spectroscopy. *Physica B* **158**, 701–722.

Majzlan J., Lalinská, B., Chovan, M., Bläß, U., Bretcht., B., Göttlicher J., Steininger R., Hug, K., Ziegler, S. and Gescher J. (2011) A mineralogical, geochemical and microbiological assessment of the antimony- and arsenic-rich neutral mine drainage tailings near Pezinok, Slovakia. *American Mineralogist* **96**, 1-13.

Mao M., Lin J. and Pan Y. (2010) Hemimorphite as a natural sink for arsenic in zinc deposits and related mine tailings: Evidence from single-crystal EPR spectroscopy and hydrothermal synthesis. *Geochimica et Cosmochimica Acta* **74**, 2943-2956.

Marshall S. A. and Serway R. A. (1969) Electron spin resonance absorption spectrum of the AsO molecule-ion in γ-irradiated single-crystal calcite. *Journal of Chemical Physics* **50**, 435-439.

Moldovan B. J., Jiang D. T. and Hendry M. J. (2003) Mineralogical Characterization of Arsenic in Uranium Mine Tailings Precipitated from Iron-Rich Hydrometallurgical Solutions. *Environmental Science & Technology* **37**, 873-879.

Murty P. N., Murty C. R. K. and Subramanian S. (1977) Electron paramagnetic resonance study of X-irradiated arsenate-doped phosphate: KH_2AsO_4/KH_2PO_4. *physica status solidi* **A39**, 675-682.

Nilges M. J., Pan Y. and Mashkovtsev R. I. (2009) Radiation-induced defects in quartz. III. W-band EPR, ENDOR and ESEEM study of a peroxy radical. *Physics and Chemistry of Minerals* **36**, 61-73.

Paktunc D., Dutrizac J. and Gertsman V. (2008): Synthesis and phase transformations involving scorodite, ferric arsenate and arsenical ferrihydrite: implications for arsenic mobility. *Geochimica et Cosmochimica Acta* **72**, 2649-2672.

Paktunc D., Foster A. L., Heald S. and Laflamme, G. (2004): Speciation and characterization of arsenic in gold ores and cyanidation tailings using X-ray absorption spectroscopy. *Geochimica et Cosmochimica Acta* **68**, 969-983.

Pan Y., Fleet M. E., Chen N., Weil J. A. and Nilges M. J. (2002) Site preference of Gd in fluorapatite by single-crystal W-band EPR and X-ray refinement of the structure: A comparative study. *The Canadian Mineralogist* **40**, 1157-1166.

Pan Y., Mashkovtsev R. I., Huang D., Mao M. and Shatskiy A. (2011) Mechanisms of Cr and H incorporation in stishovite determined by single-crystal EPR spectroscopy and DFT calculations. *American Mineralogist* **96**, 1331-1342.

Pöppl A., Tober O. and Völkel G. (1994) ESR study of the AsO_3^{2-} radical in γ-irradiated betaine arsenate. *Physica Status Solidi* **B183**, K63-K66.

Raju K. S. (1983a) Dendritic structure of gel grown gypsum. *Crystal Research and Technology* **18**, 1277-1281.

Raju K. S. (1983b) Interpenetration twinning in gel-grown gypsum single crystals. *Journal of Materials Science Letters* **2**, 705-709.

Ravel B. (2009): ATHENA user guide: http://cars9.uchicago.edu/~ravel/software/exafs/.

Ravel B. and Newville M. (2005) ATHENA, ARTEMIS, HEPHAESTUS: data analysis for X-ray absorption spectroscopy using IFEFFIT. *Journal of Synchrotron Radiation* **12**, 537-541.

Ravenscroft P., Brammer H. and Richards K. S. (2009) Arsenic pollution: a global synthesis. John Wiley and Sons.

Reeder R. J., Schoonen M. A. A., Lanzirotti A. (2006) Metal speciation and its role in bioaccessibility and bioavailability. *Reviews in Mineralogy and Geochemistry* **64**, 59-113.

Rehr J. J. and Albers R. C. (2000) Theoretical approaches to x-ray absorption fine structure. *Reviews of Modern Physics* **72**, 621-654.

Ressler T. (1997) WinXAS: A new software package not only for the analysis of energy-dispersive XAS data. *Journal de Physique IV* **7**, 269-270.

Rodríguez J. D., Jiménez A., Prieto M., Torre L. and García-Granda S. (2008) Interaction of gypsum with As(V)-bearing aqueous solutions: Surface precipitation of guerinite, sainfeldite, and $Ca_2NaH(AsO_4)2{\cdot}6H_2O$, a synthetic arsenate. *American Mineralogist* **93**, 928-939.

Rodríguez-Blanco J. D., Jiménez A. and Prieto M. (2007) Oriented overgrowth of pharmacolite ($CaHAsO_4{\cdot}2H_2O$) on gypsum ($CaSO_4{\cdot}2H_2O$). *Crystal Growth Design* **7**, 2756–2763.

Roman-Ross G., Charlet L., Cuello G. J. and Tisserand D. (2003) Arsenic removal by calcite and gypsum in lacustrine environments. *Journal de Physique IV France* **107**, 1153-1156.

Saalfield S. L. and Bostick B. C. (2010) Synergistic effect of calcium and bicarbonate in enhancing arsenate release from ferrihydrite. *Geochimica et Cosmochimica Acta* **74**, 5171–5186.

Savage K. S., Bird D. K. and O'Day P. A. (2005) Arsenic speciation in synthetic jarosite. *Chemical Geology* **215**, 473-498.

Schofield P. F., Knight K. S. and Stretton I. C. (1996) Thermal expansion of gypsum investigated by neutron powder diffraction. *American Mineralogist* **81**, 847-851.

Serway R. A. and Marshall S. A. (1966) Electron spin resonance absorption spectrum of the AsO_3^{2-} molecule ion in γ–irradiated single–crystal calcite. *The Journal of Chemical Physics* **45**, 2309-2314.

Suess E., Scheinost A., Bostick B. C., Merkel B. J., Wallschlaeger D. and Planer-Friedrich B. (2009): Discrimination of thioarsenites and thioarsenates by X-ray absorption spectroscopy. *Analytical Chemistry* **81**, 8318-8326.

Tanji K. K. (1969) Solubility of gyspum in aqueous electrolytes as affected by ion association and ionic strengths up to 0.15 M and at 25 ºC. *Environmental Science & Technology* **3**, 656-661.

Vaughan D. J. (2006) Arsenic. *Elements* **2**, 71-75.

Waychunas G. A., Rea B. A., Fuller C. C. and Davis J. A. (1993) Surface-chemistry of ferrihydrite .1. EXAFS studies of the geometry of coprecipitated and adsorbed arsenate.

Geochimica et Cosmochimica Acta **57**, 2251-2269.

Wollmann G. and Voigt W. (2008) Solubility of gypsum in MSO_4 solutions (M = Mg, Mn, Co, Ni, Cu, Zn) at 298.15 K and 313.15 K. *Journal of Chemical & Engineering Data* **53**, 1375-1380.

Xu R. (1992) EPR studies of AsO_3^{2-} centers in $MgNH_4PO_4 \cdot 6H_2O$ (struvite) crystals. *Physica Status Solidi* **B172**, K15-K18.

Zhu Y. N., Zhang X. H., Xie Q. L., Wang D. Q. and Cheng G. W. (2006) Solubility and stability of calcium arsenates at 25°C. *Water, Air and Soil Pollution* **169**, 221-238.

CHAPTER 4

Arsenic incorporation in struvite ($NH_4MgPO_4 \cdot 6H_2O$): A synchrotron XAS and single-crystal EPR study

4.1 Introduction

Wastewaters (e.g., domestic, commercial and industrial sewages, agricultural and surface runoffs, and mine tailings) often contain high levels of phosphate ions. If discharged without treatment, these wastewaters result in eutrophication of receiving rivers and lakes, threatening the environment and human health (de-Bashan and Bashan, 2004; Parsons and Smith, 2008). Another common element in wastewaters is nitrogen, which exists in high abundances in human and livestock wastes and poultry manure (Perera et al., 2007; Zhang and Lau, 2007). Therefore, recovery of phosphates and nitrogen from wastewaters is not only necessary for the sake of environmental protection but also can be used as new fertilizers with significant economic merits, making the wastewater treatment industry more sustainable. One common product from spontaneous precipitation of phosphate- and nitrogen-rich wastewaters is struvite ($NH_4MgPO_4 \cdot 6H_2O$), which is also an important biomineral occurring as a major constituent of kidney and urinary stones in human and animals and is often found as a major constituent in guano deposits, soils and organic-rich sediments (Frost et al., 2004; Ferraris et al., 1973). Struvite containing both nitrogen and phosphorus has obvious advantages over other fertilizers and has been the subject of numerous recent studies, especially with respect to the sustainable treatment of domestic or animal wastewaters (de-Bashan and Bashan, 2004; Doyle and Parsons, 2002; El Diwani et al., 2007; Jaffer et al., 2002; Le Corre et al., 2009; Negrea et al., 2010; Pang, 2008; Parsons and Smith, 2008; Perera et al., 2007; Rahaman, 2009; Tünay et al., 1997; Zhang and Lau, 2007).

Struvite crystallizes in the space group $Pmn2_1$ and consists of isolated PO_4 tetrahedra (site symmetry *m*), $Mg(H_2O)_6$ octehedra (*m*) and $(NH_4)O_{10}$ irregular polyhedra (*m*), held together by a complex network of hydrogen bonds (Fig. 4-1; Ferraris et al., 1973; Weil, 2008). One major concern of struvite as fertilizer is that it may sequester a wide variety of toxic heavy metals and

metalloids such as As, Cd, Co, Cr, Cs, Cu and Ni (Chowardi et al., 1982, Agarwal and Chand 1984; Sivdprasad et al., 1990; Chand and Agarwal 1991; Rao et al., 1991; Ravikumar et al., 1997; Sougandi et al., 2002; Weil, 2008, 2009; Aguilera et al., 2010; Arai et al., 2003; Hunger et al., 2008; Sohel et al., 2010). For example, accommodation of As in struvite is suggested by the presence of its arsenate analogs ($NH_4MgAsO_4 \cdot 6H_2O$ and $CsMgAsO_4 \cdot 6H_2O$; Weil, 2008, 2009). Not surprisingly, spontaneous precipitation of struvite has been proposed to be useful for the removal of As and other heavy metals and metalloids from wastewaters (Ronteltap et al., 2007; Uysal et al., 2010). On the other hand, direct use of struvite recovered from wastewaters as fertilizer, without removal of As and other heavy metals and metalloids, represents a potential source of contamination.

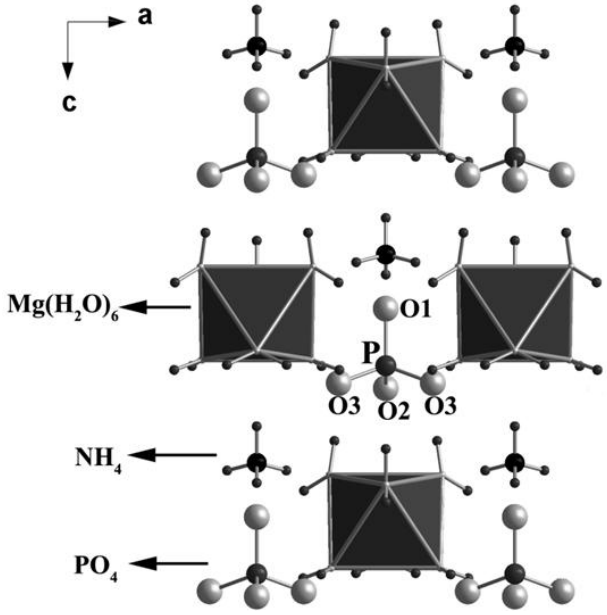

Figure 4-1 Crystal structure of struvite projection along [010] showing the local structural environment of the P site (data from Ferraris et al., 1973).

Of course, the presence of arsenate analogs is not proof for arsenic incorporation in struvite precipitated spontaneously from wastewaters under ambient conditions. For example, apatites $Ca_5(PO_4)_3(F,OH,Cl)$ have arsenate analogs $Ca_5(AsO_4)_3(F,OH,Cl)$, which are also known to form extensive solid solutions at elevated temperatures (Pan and Fleet, 2002; Lee et al., 2009; Biagioni, et.al., 2013). However, Bothe and Brown (1999) noted that there is no solid solution

between $Ca_5(PO_4)_3(OH)$ and $Ca_5(AsO_4)_3(OH)$ precipitated under ambient conditions. In this contribution we report on the synthesis of struvite with $Na_2HAsO_4{\cdot}7H_2O$ or $NaAsO_2$ in the starting materials over a range of pH values under ambient conditions. My struvite crystals reaching 5 mm in the maximum dimension allow chemical analyses by use of multiple, high-sensitivity chemical (inductively coupled plasma mass spectrometry, ICPMS), imaging (microbeam synchrotron X-ray fluorescence mapping, μ-SXRF), and structural techeniques (synchrotron X-ray absorption spectroscopy, XAS; and electron paramagnetic resonance spectroscopy, EPR). These data not only confirm the uptake of lattice-bound As in struvite formed under ambient conditions but also provide insights into its speciation and local structural environment, with direct relevance to struvite recovered from wastewater treatment plants both for the removal of As and as a new fertilizer.

4.2 Synthesis experiments and characterization techniques

Two series of synthesis experiments (I and II) by using the single diffusion gel technique (Henisch, 1973; Henisch et al., 1965; Patel and Rao, 1982) have been made to produce crystals of arsenic doped struvite. Five experiments of Series I used mixtures of 20 ml sodium metasilicate solution (Na_2SiO_3) and 5 ml each of 1 M ammonium dihydrogen phosphate ($NH_4H_2PO_4$) and 0.01 M sodium hydrogen arsenate heptahydrate ($Na_2HAsO_4{\cdot}7H_2O$), which were first adjusted to pH = 4, 6, 7, 8 and 9 with acetic acid and then poured into test tubes to form gels. After the gel settled down in each tube, 10 ml solution of 0.5 M magnesium sulphate ($MgSO_4$) was poured into the tubes that were then covered with aluminum foil and kept at room temperature for one month. Series II of only two runs at pH = 6 and 8 utilized the same procedure described above and the same starting materials except that 0.04 M $NaAsO_2$ standard solution was added as the source for arsenic. Individual runs at various pH values have been designated as I-4, 6, 7, 8 and 9 and II-6 and 8 hereafter.

Hand-picked crystals from each synthesis experiment were first washed with deionized water and then pulverized for powder X-ray diffraction (PXRD) analysis on a PANalytical X'pert PRO X-ray diffractometer using Co Kα1 radiation (λ = 1.7809Å) at 40 kV and 45 mA, and for ICPMS analyses of As with the HF-HNO_3 dissolution method. Selected crystals were

also carbon-coated for examination on a JEOL 840A scanning electron microscope (SEM).

4.2.1 X-band EPR measurements

Single-crystal X-band EPR measurements at room temperature were made on a Bruker EMX instrument at the Saskatchewan Structure Sciences Centre, University of Saskatchewan, Selected crystals of struvite from both series of experiments were irradiated at room temperature in a ^{60}Co cell (dose rate = ~460 Gy/h) for 2 days. In particular, one crystal from I-8 was selected for detailed single-crystal EPR measurements at room temperature in four rotation planes approximately parallel to the (100), (010), (001) and (101) crystal faces. Experimental conditions included microwave frequencies from ~9.360 to ~9.386 GHz, a microwave power of ~20 mW, a modulation frequency of 100 kHz, and a modulation amplitude of 0.1 mT, a constant angle interval of 5º, and a spectral resolution of ~0.137 mT (i.e., 2048 field data points over the scan range from 190 to 470 mT).

4.2.2 Synchrotron μ-SXRF mapping and arsenic K edge XAS experiments

The μ-SXRF mapping experiments were made at the VESPERS beamline (Feng et al., 2007; Lin et al., 2011) and As K edge XAS analyses were conducted in the HXMA beamline (Jiang et al., 2007), at the Canadian Light Source (CLS), University of Saskatchewan. μ-SXRF mapping for a crystal from I-8 (Fig.4-4), which was mounted on a three-way NanoMotion stage tilting at 45° azimuthally and orthogonally to the incoming beam, was made with a beam of ~2 μm in diameter, a step size of 3 μm, and a constant counting time of 1 s for each data point.

Arsenic K edge (11, 867 eV) XAS data for powder obtained from selected crystals (I-8 and II-8) and seven model compounds (arsenopyrite, realgar, orpiment, arsenolite, synthetic scorodite, and As_2O_3 and As_2O_5 from Alfa Aesar) were collected at in the fluorescence mode and the transmission mode, respectively. A Si(111) monochromator crystal and Rh mirrors (collimating and focusing mirrors) with a 32 element Ge detector and wiggler field of 1.9 T were used during data collection. All samples were diluted with boron nitride to give a satisfactory edge jump and absorption. The sizes of the scan steps for the pre-edge, XANES, and EXAFS regions for all experiments were 10 eV/step, 0.25 eV/step, and 0.05 $Å^{-1}$/step, respectively.

4.3 Results and discussion

4.3.1 Characterization and composition of synthetic struvite

All the synthesis experiments, except for I-4, yielded several colorless crystals of two contrasting morphologies (i.e. prismatic and tabular) with the maximum dimension up to 5 mm. PXRD analyses (Fig. 4-2) show that the prismatic crystals (Fig. 4-3) are struvite, whereas the tabular ones are boussingaultite $(NH_4)_2Mg(SO_4)_2 \cdot 6H_2O$.

The μ-SXRF mapping shows that the distribution of As in sample I-8 is reasonably homogeneous (i.e., intensity with a standard deviation of only 11%) without any visible As-rich inclusions (Fig. 4-4b). Triplicate ICPMS analyses of the struvite samples from Series I experiments show an apparent trend of enhanced uptake of As with increasing pH, from 227±15

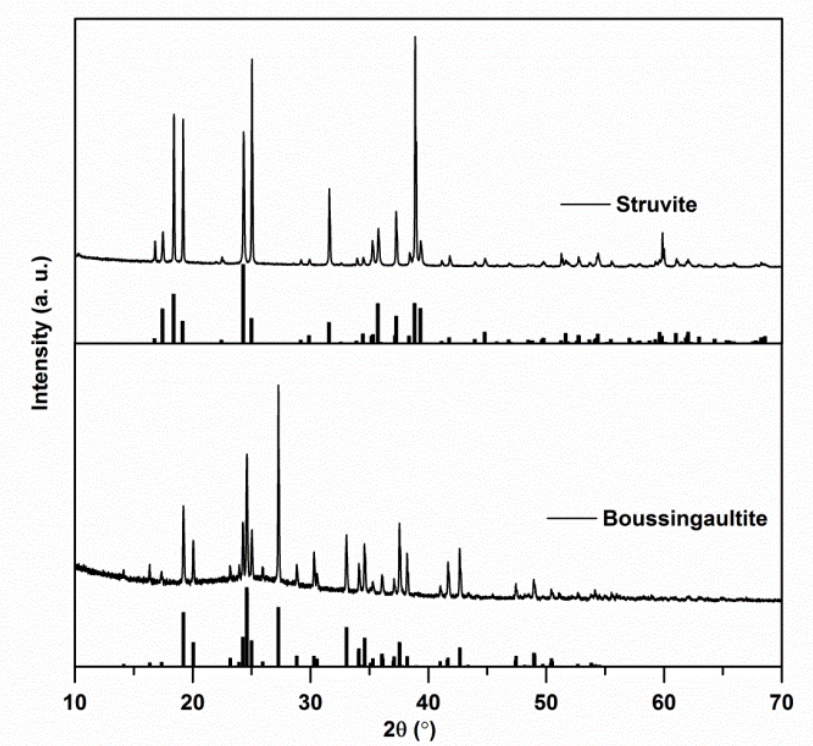

Figure 4-2 Representative powder X-ray diffraction patterns of synthetic struvite and boussingaultite. Also shown for comparison are their respective reference patterns from the Inorganic Crystal Structure Database (ICSD).

ppm in I-6 to 78±5, 352±33 and 547±15 ppm in I-7, I-8 and I-9, respectively (Fig. 4-5). The

standard deviation of ±9.4% obtained from ICPMS analyses of different crystals in I-8 (Fig. 4-5) is similar to the variation in intensity present in one crystal as revealed by μ-SXRF (Fig. 4-4b). Struvite crystals from Series II experiments contain significantly lower As contents (24 and 23 ppm) than their counterparts from Series I.

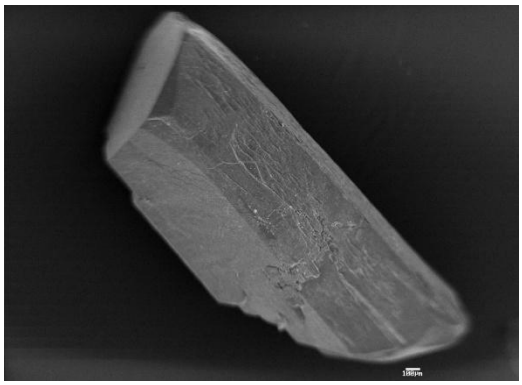

Figure 4-3 SEM image showing a doubly-terminated, prismatic crystal of synthetic struvite (I-8)

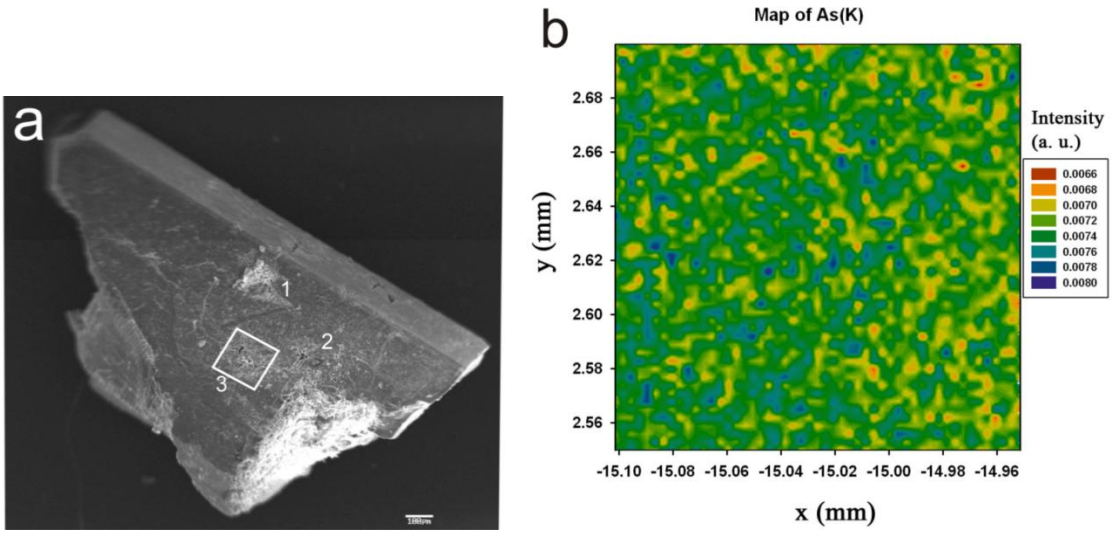

Figure 4-4. (a) SEM image of a prismatic crystal of synthetic struvite (I-8) showing three areas (1, 2 and 3) of notable beam damage from μ-SXRF mapping; (b) μ-SXRF map showing the distribution of As in an 150 μm x 150 μm area (outlined in a).

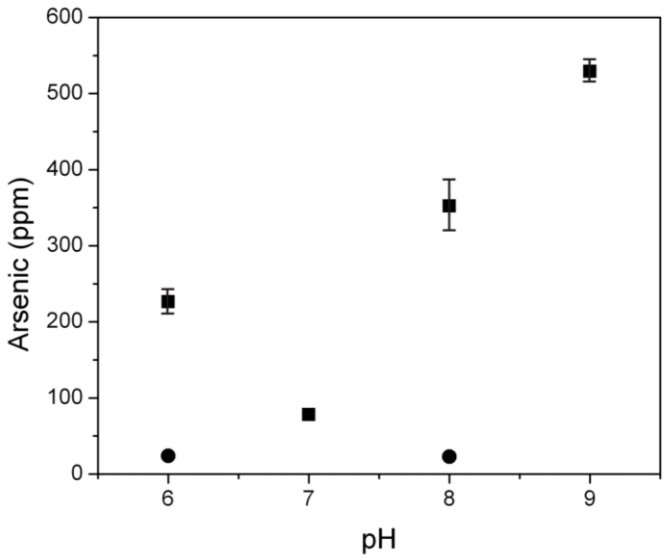

Figure 4-5 Arsenic contents in synthetic struvite as a function of pH. Squares and circles denote data from Series I and II experiments. Uncertainties are shown or are smaller than the symbols.

4.3.2 Synchrotron As K edge XANES and EXAFS data

My initial XAS measurements at room temperature showed that the As K edge XANES spectra of struvite have notable variations between scans, suggesting significant radiation-induced reduction of As^{5+}. Subsequently, XAS measurements were made for 5 scans at 20 K by using an Oxford Instruments liquid-helium cryostat. These spectra measured at 20 K, unlike their counterparts collected at room temperature, do not exhibit any visible changes in the line shape or intensity between scans. The XANES spectra of struvite I-8 and II-8 are similar to each other and are characterized by a main peak centered at ~11,874eV, which is in excellent agreement with those of scorodite and As_2O_5 (Fig. 4-6a) and suggests the dominant oxidation state of As^{5+}. This observation is also evident in the first-derivative spectra of I-8 and II-8 (Fig. 4-6b).

The As K edge EXAFS $k^3 \bullet \chi(k)$ data of struvite I-8 and II-8 are also similar, except that the former with a higher As content has better signal-to-noise ratios than the latter. These EXAFS data have been analyzed for R space curve fittings based on the FEFF7 modeling (Rehr and

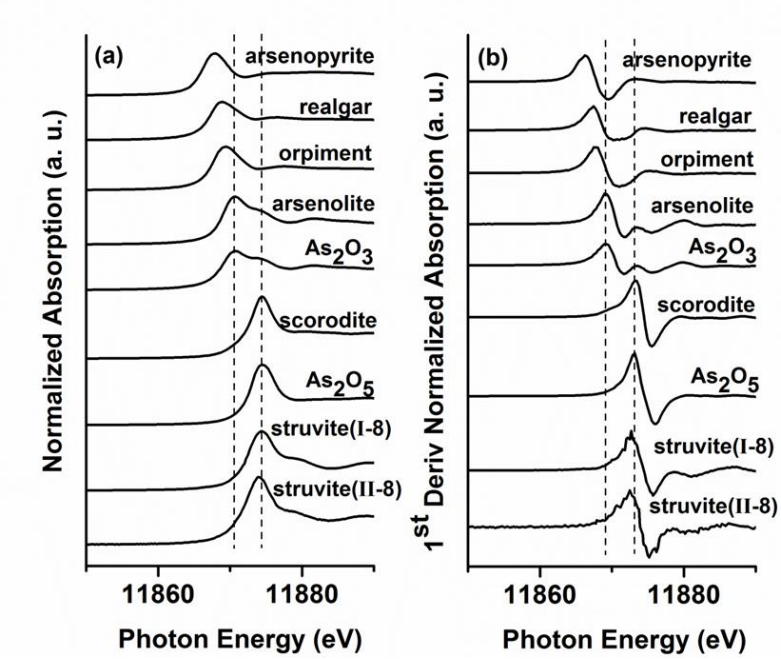

Figure 4-6 (a) As K edge XANES spectra of struvite samples (I-8 and II-8) and model compounds;and (b) corresponding first-derivative XANES spectra.

Albers, 2000) by using the XAFS data processing software WinXas 3.2 (Ressler, 1997). Fourier transform was performed by using a Gaussian window function over the *k* range of 2.78-14.63 $Å^{-1}$ with the window parameter of 30%, and the R-space data was fitted in a window of 2.79-3.73 Å (Fig. 4-7). The fitted interatomic distance for the nearest neighbor As-O shell is 1.69 Å (Table 4-1), matching closely to those of typical As^{5+} (Kitahama et al., 1975; Foster et al., 1998; Moldovan et al. 2003). This interatomic distance is notably larger than that of the average P-O bond distance in struvite (1.54 Å, Ferraris, 1973), requiring significant expansion of the P site.

Beyond the nearest-neighbor As-O shell, two groups of scattering paths are included in the fitting (regions I and II in Fig. 4-7). The first group is 3 types of multiple scatterings occurring in the AsO_4 tetrahedron. Following the approach of Kim et al (2013), the Debye-Waller factors (σ^2) for these paths were constrained, namely the $\sigma^2_{\text{As-Oa-Ob}}$ and $\sigma^2_{\text{As-Oa-As-Oa}}$ were correlated to those of the nearest-neighbor As-O scattering by factors of 2 and 4, respectively. Meanwhile, the $\sigma^2_{\text{As-Oa-As-Ob}}$ values were changed by factors of 2 to 4 to that of the As-O path. The FEFF modeling of these multiple scattering paths was based on the morphology of the AsO_4

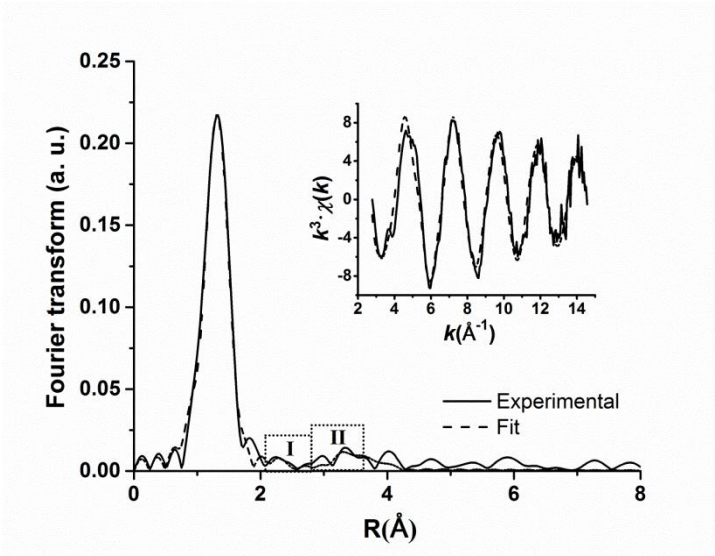

Figure 4-7 R-space curve fittings for As K edge EXAFS spectra of Struvite. The Fourier transforms of $k^3 \bullet \chi(k)$ spectra were performed over the k ranges of 2.78-14.63 Å^{-1} and R-space fitting windows of 2.79-3.73 Å. Also included in inserts are the $k^3 \bullet \chi(k)$ spectra in comparison with those from R-space fittings.

Table 4-1. Local environment of As from R space fittings of As K edge EXAFS data in struvite

Paths	CN	R (Å)	σ^2 (Å^2)	E0 (eV)
As-O	4.0§	1.69	0.0018	2.5
As-Oa-Ob	6.0§	2.90	0.0036	2.5
As-Oa-Ob	6.0§	3.19	0.0036	2.5
As-Oa-As-Oa	4.0§	3.58	0.0072	2.5
As-Oa-As-Ob	6.0§	3.25	0.0040	2.5
As-Oa-As-Ob	6.0§	3.47	0.0050	2.5
As-O	3.3	3.75	0.0100	2.5
As-O	6.0	4.24	0.0100	2.5

Oa and Ob mark nonequivalent oxygen atoms; § denotes fixed values.

tetrahedron in the scorodite structure (Kitahama et al., 1975). Inclusion of these multiple scattering paths in the data analysis is necessary for struvite, because the intensity contribution from these multiple scattering is not negligible (Fig. 4-7). Noted that the estimated σ^2 value for

the nearest-neighbor As-O path of struvite is slightly larger than that of scorodite (Chen et al. 2009), suggesting a larger distortion of the arsenate tetrahedron in the former. This local structural distortion is expected to partially remove the degeneration of the multiple scattering paths As-Oa-Ob andAs-Oa-As-Ob. Therefore, the path As-Oa-Ob was treated as two sets of separated paths from the scattering distances perspective in fitting (Table 4-1), same was the path As-Oa-As-Ob. Nevertheless the FEFF multiple scattering modeling on the basis of the scorodite structure is shown to be suitable.

The second group of scattering paths (II in Fig. 4-7) include outer As-O paths from two groups of oxygen atoms of the neighboring $Mg(H_2O)_6$ groups (Fig. 4-1). The calculated interatomic distances for the outer As-O paths from the first group are larger than those in the ideal struvite structure, suggesting that local structural distortion associated with As^{5+} incorporation reaches up to 3.75 Å. Although the absence of any strong back scattering elements in this R region makes accurate analysis of the experimental data difficult, the fitted two sets of the single scattering As-O paths are consistent with the extended PO_4 site symmetry, supporting the substitution of As^{5+} for P^{5+} in struvite.

4.3.3 Single-crystal X-band EPR spectra

Single-crystal EPR measurements show that synthetic struvite does not contain any paramagnetic defects before gamma-ray irradiation but is characterized by six sets of four-line resonance signals all centered at the effective g value of ~2.00 (Centers I-VI in Figure 4-8a). Centers I to V are all characterized by large but unequal separations of ~50-81 mT, ~55-82 mT, ~44-85 mT, ~47-91 mT and ~50-98 mT, respectively, and have approximately similar linewidth of ~0.5 mT. The relative intensities of Centers I to V are 100:13:11:7:3. These five centers are all attributable to simple spins (i.e., a single unpaired electron S=1/2) interacting with a ^{75}As nucleus (i.e., nuclear spin number I=3/2 and natural isotope abundance = 100%). The individual hyperfine lines of Center II are resolved to a maximum of 4 when the external magnetic field **B** is rotated away from symmetry axes (Fig. 4-9), indicative of triclinic site symmetry in orthorhombic struvite. Centers I, III, IV and V, however, are resolved to at most two magnetically nonequivalent sites and therefore have monoclinic site symmetries (Figures 4-10-13). At some orientations individual lines of Center I are resolved into triplets with an intensity

ratio of approximately 1:2:1 (Fig. 4-8b), characteristic of a superhyperfine structure arising from interactions with two equivalent or nearly equivalent ^{1}H nuclei.

The spin Hamiltonian for Centers I to V, ignoring the incompletely resolved ^{1}H superhyperfine structure of Center I, can be written as follow:

$$\mathbf{H} = \beta_e \mathbf{S \cdot g \cdot B} + \mathbf{I \cdot A \cdot S} + \mathbf{I \cdot P \cdot I} - \beta_n \mathbf{I \cdot g_n \cdot B} \qquad (4.1)$$

where β_e and β_n are the electronic (Bohr) and nuclear magnetons, respectively; **S** and **I** are the electron spin and nuclear spin operators, respectively; **g** is the Zeeman electron term; and **A** and **P** are the nuclear hyperfine and quadrupole terms for ^{75}As with an isotropic g_n value of 0.959647.

All analyses have been made with the experimental axes **x**, **y** and **z** along the crystallographic axes **a**, **c** and **b**, respectively. The total number of line-position data points used for the fittings of Centers I to V were 1736, 1047, 1074, 838 and 948, respectively. The final values of the root-mean-squares of weighed differences (RMSD) between the calculated and observed line positions for the five centers are 0.132 mT, 0.167 mT, 0.158 mT, 0.167 mT and 0.193 mT, respectively (Table 4-3), which are all less than half of the average linewidths. Spectral simulations have been used to determine the two matrices **A**(^{1}H) for the superhyperfine structure of Center I (Table 4-3), which include an isotropic component a = 0.410 mT and an anisotropic component b = 0.278 mT. The directions of the unique principal A(^{1}H) axes at (θ=30°, ϕ=270°) and (30°, 90°) are close to the orientations from P to two nearest H atoms in struvite (Table 4-4; Ferraris et al., 1973), where θ and ϕ are tilting angles from crystallographic axes **b** and **a**, respectively.

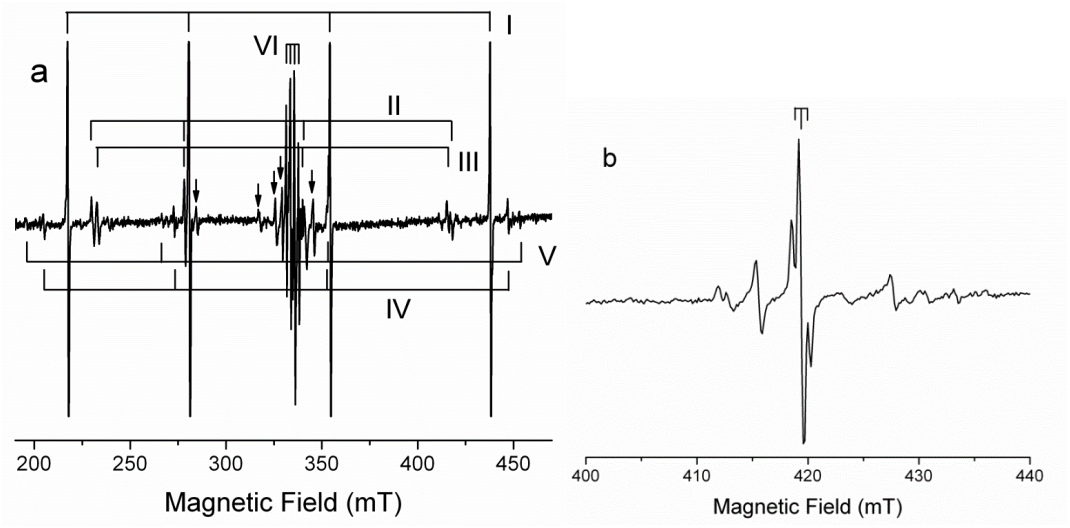

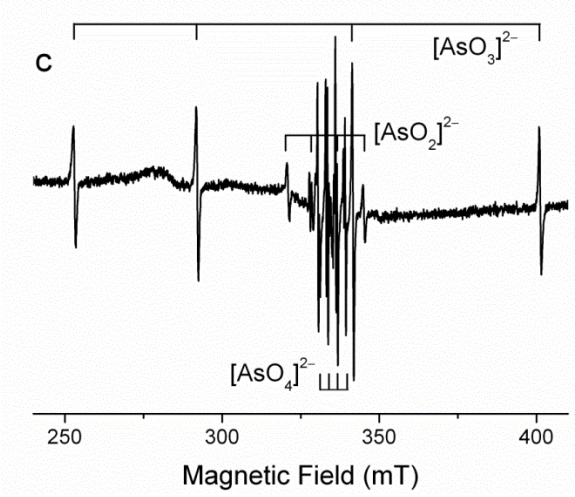

Figure 4-8 Representative single-crystal EPR spectra of gamma-ray-irradiated struvite measured at: a) **B**//**c** showing six arsenic-centered oxyradicals with characteristic ^{75}As hyperfine structures (labeled I to VI); and unknown peaks are marked by arrows; and b) **B**∧**b** = ~30° in the high magnetic field showing that Center I contains a well-resolved superhyperfine structure arising from interactions with two equivalent ^{1}H nuclei. Also shown for comparison is c) a single-crystal EPR spectrum of gamma-ray-irradiated boussingaultite measured at **B**//**c** showing three well-resolved arsenic-centered oxyradicals ($[AsO_4]^{2-}$, $[AsO_3]^{2-}$ and $[AsO_2]^{2-}$) .

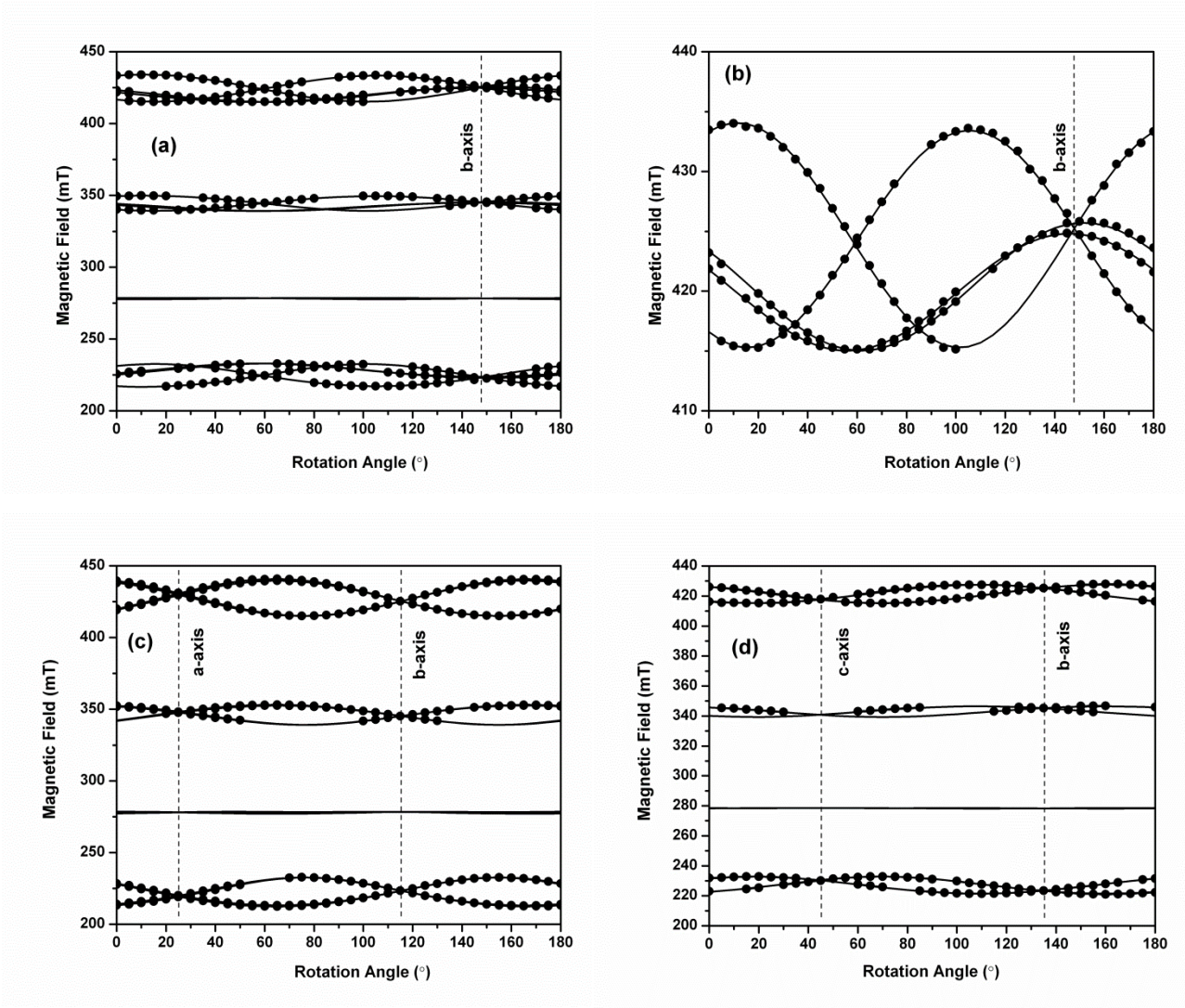

Figure 4-9. Line-position data (road maps) of Center II in struvite: a) and b) approximately parallel to the (101) crystal face at ν = ~9.386 GHz, c) approximately parallel to the (001) face at ν = ~9.386 GHz, and d) approximately parallel to the (100) face at ν = ~9.386 GHz.

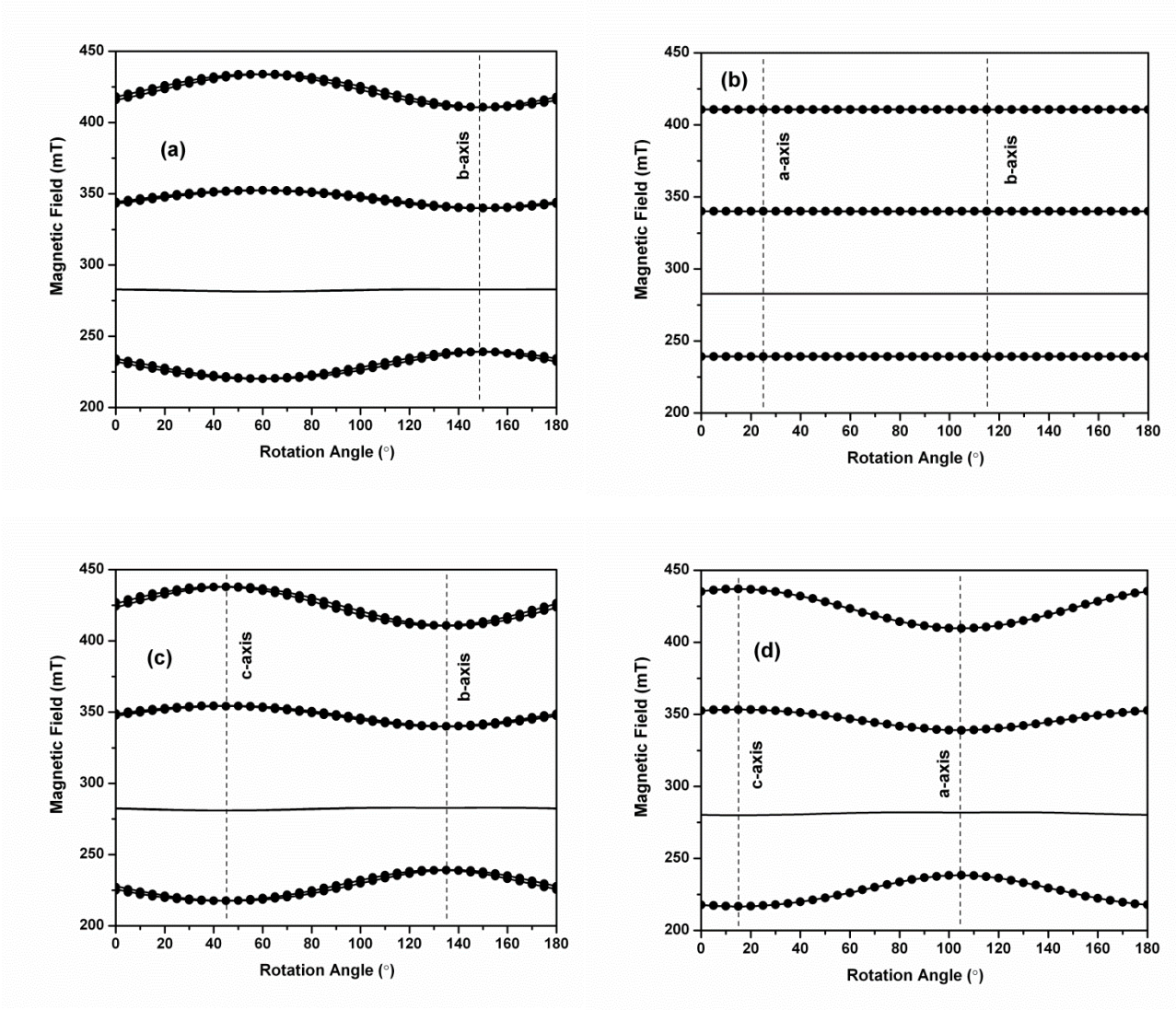

Figure 4-10. Line-position data (road maps) of Center I in struvite: a) approximately parallel to the (101) crystal face at ν = ~9.386 GHz, b) approximately parallel to the (001) face at ν = ~9.386 GHz, c) approximately parallel to the (100) face at ν = ~9.386 GHz, and d) approximately parallel to the (010) face at ν = ~9.360 GHz.

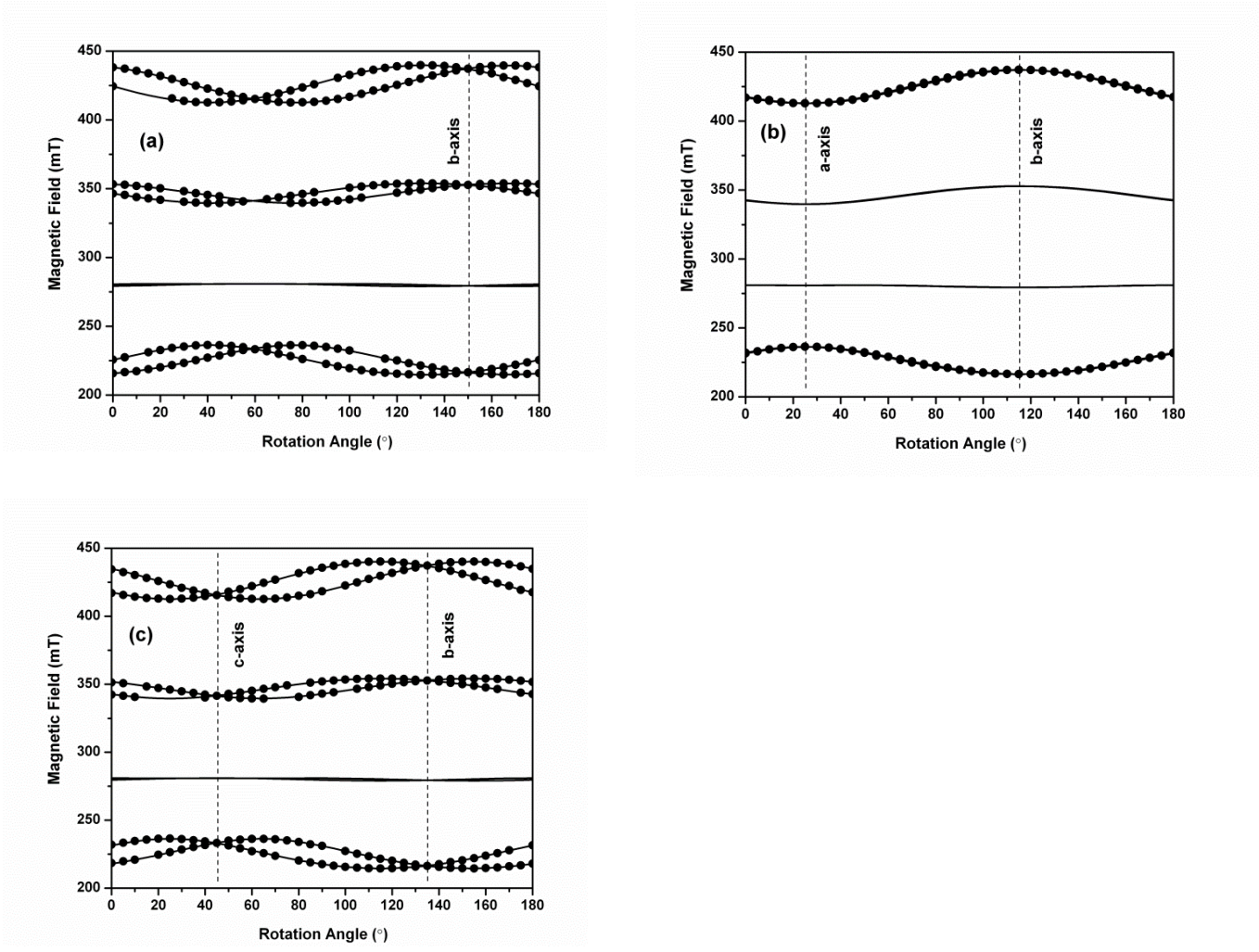

Figure 4-11. Line-position data (road maps) of Center III in struvite: a) and b) approximately parallel to the (101) crystal face at ν = ~9.386 GHz, c) approximately parallel to the (001) face at ν = ~9.386 GHz.

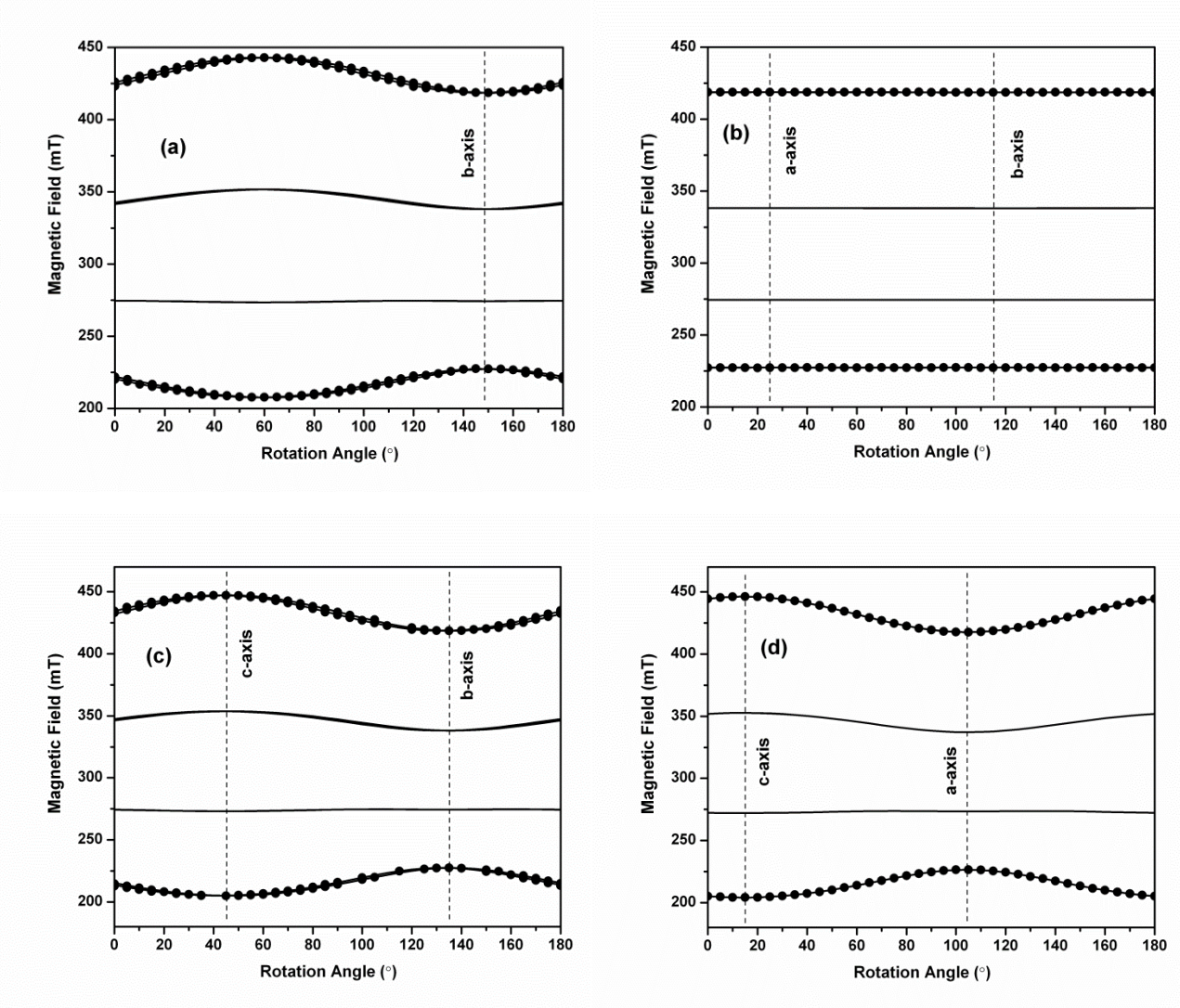

Figure 4-12. Line-position data (road maps) of Center IV in struvite: a) approximately parallel to the (101) crystal face at ν = ~9.386 GHz, b) approximately parallel to the (001) face at ν = ~9.386 GHz, c) approximately parallel to the (100) face at ν = ~9.386 GHz, and d) approximately parallel to the (010) face at ν = ~9.360 GHz.

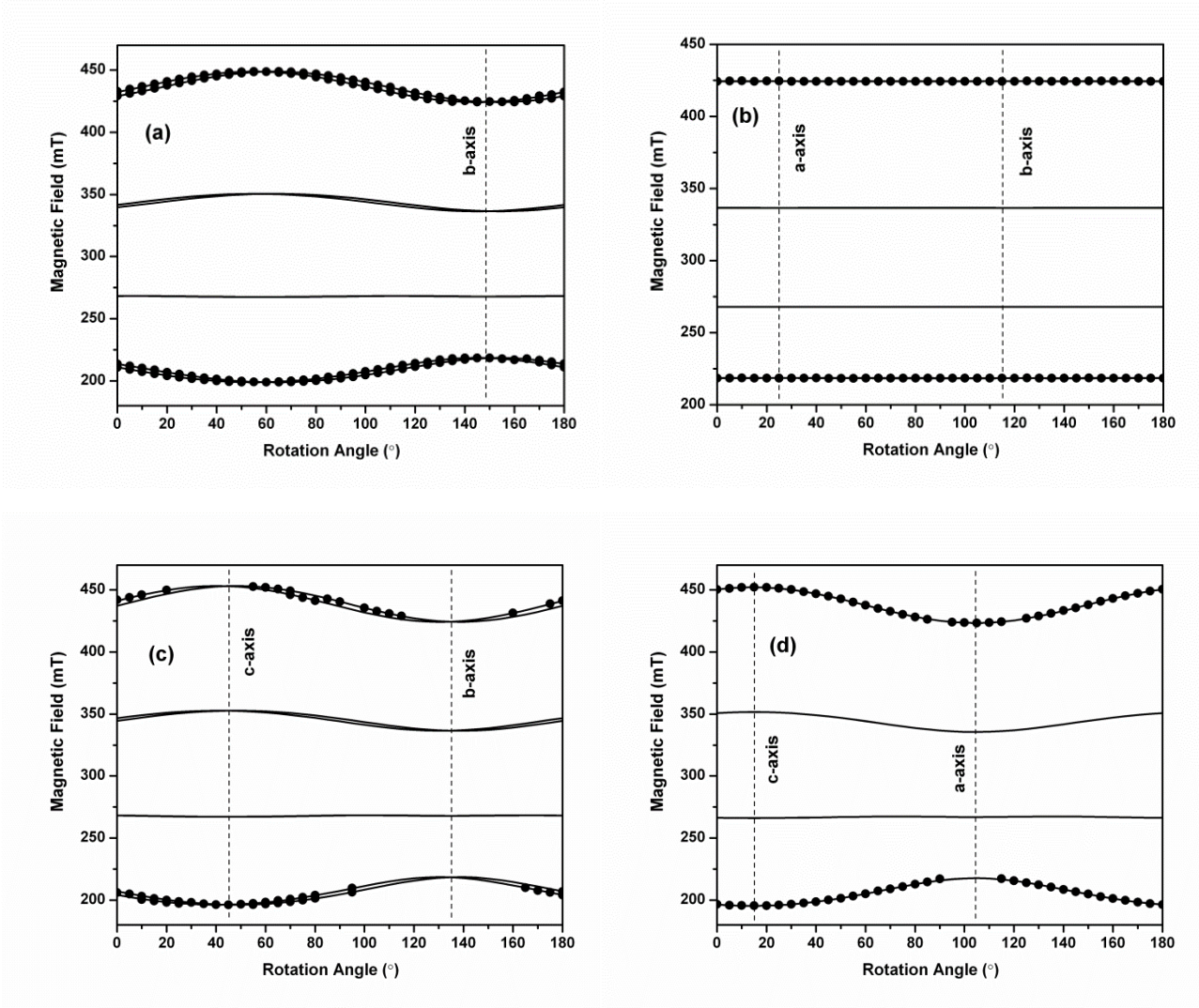

Figure 4-13. Line-position data (road maps) of Center V in struvite: a) approximately parallel to the (101) crystal face at ν = ~9.386 GHz, b) approximately parallel to the (001) face at ν = ~9.386 GHz, c) approximately parallel to the (100) face at ν = ~9.386 GHz, and d) approximately parallel to the (010) face at ν = ~9.360 GHz.

The best-fit matrices **g** and **A**(^{75}As) of Centers I to V (Table 4-3) are approximately axial in symmetry and are closely comparable to those of the well-established $[AsO_3]^{2-}$ radical (Table 4-2; Lin and McDowell, 1964; Serway and Marshall, 1966; Lin et al., 2013). This radical is readily linked to diamagnetic $[AsO_4]^{3-}$ precursors and involves the sp^3 hybridization for the unpaired electron orbital directed towards the missing O atom (Table 4-2; Pan, 2013). Specifically, the orientations of the unique g_3 and A_1 axes of Centers I, II and III (Table 4-3) are approximately along the P-O1 bond direction (86.2°, 90°), the P-O3 bond direction (61.2°, 159.7°) and the P-O2 bond direction (23.1°, 270°), respectively. These $[AsO_3]^{2-}$ radicals in struvite are readily attributed to electron trapping on the central As^{5+} ion of the substitutional $[AsO_4]^{3-}$ group at the $[PO_4]^{3-}$ position after removal of one of the four nearest O atoms, via the following reaction:

$$[AsO_4]^{3-} \xrightarrow{hv} [AsO_3]^{2-} + O^{2-} \qquad (4\text{-}2)$$

Similarly, Centers IV and V are characterized by the orientations of their unique g_3 and A_1 axes approximately along the P-O2 bond direction and may represent variants of Center I: i.e., $[AsO_3]^{2-}$ radicals from electron trapping on substitutional $[AsO_4]^{3-}$ group after the removal of the O2 atom but involving slightly different distortions. The fact that the two O3 atoms coordinated to P are symmetrically equivalent explains the presence of these $[AsO_3]^{2-}$ radicals with three distinct orientations only.

Center VI is characterized by ^{75}As hyperfine coupling constants from ~1.5 to ~2.2 mT (Fig. 4-8a) and possesses multiple and strong "forbidden" nuclear transitions arising from significant nuclear quadrupole effects, typical of the well-established $[AsO_4]^{2-}$ radical with the unpaired spin localized in the $2p_z$ orbital of an O atom (Table 4-2; Pan, 2013). Unfortunately, quantitative determination of the spin Hamiltonian parameters for this $[AsO_4]^{2-}$ radical in struvite is not possible owing to difficulties in tracking the angular dependence of individual lines, which are affected by not only "forbidden" nuclear transitions but also splittings related to a triclinic site symmetry as well as overlapping lines from unknown centers (Fig. 4-8a).

Table 4-2. Spin Hamiltonian parameters of $[AsO_3]^{2-}$, $[AsO_4]^{2-}$ and $[AsO_2]^{2-}$ radicals in struvite, boussingaultite and other crystalline hosts

Host	g_1	g_2	g_3	$A_1/g_e\beta_e$ (mT)	$A_2/g_e\beta_e$ (mT)	$A_3/g_e\beta_e$ (mT)	Unpaired spin (%) 4*s*	$4p_z$	$4p_x$	Ref.
				$[AsO_3]^{2-}$						
struvite (I)	2.00431(4)	2.00399(4)	2.00154(4)	72.950(6)	56.581(5)	56.576(5)	11.9	45.8		1
struvite (II)	2.00467(6)	2.00298(7)	2.00122(6)	76.457(9)	60.210(9)	60.059(9)	12.5	45.7	0.3	1
struvite (III)	2.00419(7)	2.0034(1)	2.00161(5)	74.620(6)	58.271(9)	58.172(9)	12.2	45.9	0.2	1
struvite (IV)	2.00349(6)	2.00322(6)	2.00110(6)	79.976(9)	62.975(6)	62.937(7)	13.1	47.7		1
struvite (V)	2.00330(8)	2.00287(9)	2.00104(8)	84.771(9)	67.64(1)	67.62(1)	14.0	48.0		1
boussingaultite	2.00603(4)	2.00538(4)	2.00218(4)	63.906(5)	49.391(5)	49.016(6)	10.3	41.1	0.8	1
calcite (77K)	2.00195(5)	2.00195(5)	2.00162(5)	93.73(1)	75.24(1)	75.24(1)	15.6	51.8		2
$Na_2HAsO_4{\cdot}7H_2O$	2.005(2)	2.005(2)	2.004(2)	72.5(1)	56.7(2)	56.7(1)	11.9	44.3		3
KH_2AsO_4 (K)	1.996(5)	1.996(5)	1.996(5)	91.8	75	74.2	15.4	49.3	2.1	4
KH_2AsO_4 (L)	1.999(5)	1.999(5)	1.999(5)	76.5	60.8	60.4	12.6	45.1	0.9	4
KH_2AsO_4 (M)	2.000(5)	2.000(5)	2.000(5)	66.1	50	49.6	10.6	46.0	0.9	4
betaine arsenate	2.001(4)	1.998(4)	1.998(4)	65.9(4)	51.6(4)	51.6(4)	10.8	40.1		5
haidingerite(I)	1.999	1.999	1.999	85.23	67.26	67.26	13.9	53.2		6
haidingerite(II)	1.998	1.993	1.993	94.03	75.63	75.63	15.6	51.6		6
gypsum	2.00537(4)	2.00371(5)	2.00134(3)	69.65(1)	53.26(1)	53.12(1)	11.2	46.2	0.3	7
				$[AsO_4]^{2-}$						
scheelite (77K)	2.0470	2.0122	2.00070	2.30	1.9	1.87	0.39	1.0		8
$(NH_4)_2HPO_4$	2.030(5)	2.023(5)	2.016(5)	3.1(1)	1.7(1)	0.7(1)	0.35	3.3		9
hemimorphite	2.02407(1)	2.00982(1)	2.00326(1)	2.158(1)	1.861(1)	1.678(1)	0.36	0.7		10
boussingaultite	2.03760(6)	2.00325(6)	2.00281(6)	3.020(6)	2.332(7)	1.405(8)	0.43	3.2	2.2	1
				$[AsO_2]^{2-}$						
boussingaultite	2.0115(1)	1.9996(1)	1.9946(1)	16.86(1)	-8.14(1)	-8.44(1)	0.01	70.4	0.7	1
gypsum	2.01484(2)	1.99962(2)	1.9958(1)	16.96(1)	-7.53(1)	-7.95(2)	0.09	69.2	0.9	7

Reference 1 is this study, 2, Serway and Marshall, 1966; 3, Lin and McDowell, 1964; 4, Dalal et al., 1972; 5, Pöppl et al., 1994; 6, Giliniskaya and Afanas'eva (1981); 7, Lin et al. 2013; 8, Edwards et al. 1968; 9, Subramanian et al. 1977; 10, Mao et al. 2010. The distribution of unpaired spins in the 4*s* and 4*p* orbitals of arsenic has been re-calculated to the atomic a_0 and b_0 values of 523.11 and 11.905 mT, respectively (Weil and Bolton 2007).

Table 4-3. Spin Hamiltonian parameters of five $[AsO_3]^{2-}$ radicals in struvite at 295 K

	Matrix (Y)			k	Principal value/direction			RMSD (mT)
					Y_k	θ_k(°)	ϕ_k(°)	
				Center I				
	2.00399(4)	0	0	1	2.00431(4)	1.6(9)	270	
g		2.00154(4)	−0.00008(4)	2	2.00399(4)	90	0	
			2.00431(4)	3	2.00154(4)	88.3(9)	90	
A(^{75}As)	56.576(6)	0	0	1	72.950(6)	93.8(2)	90	0.132
(mT)		72.910(5)	−0.817(5)	2	56.581(5)	2.8(2)	90	
			56.622(5)	3	56.576(5)	90	180	
A(^{1}H)†	0.271	0	0	1	0.688	30	270	
(mT)		0.375	−0.180	2	0.271	90	0	
			0.584	3	0.271	60	90	
				Center II				
	2.00254(7)	0.00020(9)	0.00162(9)	1	2.00467(6)	37.1(9)	353(4)	
g		2.00291(7)	-0.00030(7)	2	2.00298(7)	85(3)	258(2)	
			2.00343(6)	3	2.00122(6)	53(1)	165(3)	
A(^{75}As)	69.038(9)	-3.61(1)	-7.27(1)	1	76.457(9)	52.7(2)	158.1(2)	0.167
(mT)		61.523(9)	2.898(8)	2	60.210(9)	38.4(8)	321(5)	
			66.165(8)	3	60.059(9)	81(2)	61(2)	
				Center III				
	2.0034(1)	0	0	1	2.00419(7)	71(1)	90	
g		2.00392(7)	0.00079(5)	2	2.0034(1)	90	0	
			2.00188(5)	3	2.00161(5)	19(1)	270	
A(^{75}As)	58.27(1)	0	0	1	74.620(6)	19.4(2)	270	0.158
(mT)		59.989(9)	-5.155(7)	2	58.271(9)	90	0	
			72.803(6)	3	58.172(9)	70.6(2)	90	
				Center IV				
	2.00322(6)	0	0	1	2.00349(6)	7(1)	90	
g		2.00114(6)	0.00031(7)	2	2.00322(6)	90	0	
			2.00345(6)	3	2.00110(6)	97(1)	90	0.134
A(^{75}As)	62.975(6)	0	0	1	79.976(9)	92.1(2)	90	
(mT)		79.951(9)	-0.652(8)	2	62.975(6)	90	0	
			62.962(7)	3	62.937(7)	2.1(2)	90	
				Center V				
	2.00287(9)	0	0	1	2.00330(8)	7(2)	90	
g		2.00108(8)	0.00030(9)	2	2.00287(9)	90	0	
			2.00326(8)	3	2.00104(8)	97(2)	90	
A(^{75}As)	67.62(1)	0	0	1	84.771(9)	93.8(2)	90	0.193
(MHz)		84.694(8)	-1.14(1)	2	67.64(1)	3.8(2)	90	
			67.71(1)	3	67.62(1)	90	0	

Polar angle (θ) and azimuthal angle (ϕ) are relative to the crystallographic axes b and a, respectively. †, two equivalent matrices **A**(^{1}H) are obtained from spectral simulations.

Table 4-4. Selected bond distances and directions in struvite ($Pmn2_1$: a = 6.955 (1), b = 6.142 (1), c = 11.218 (2) Å)

Bond	Distance (Å)	θ (°)	ϕ (°)
P-O3	1.5417	61.2	20.3
P-O3	1.5417	61.2	159.7
P-O2	1.5440	23.1	270
P-O1	1.5402	86.2	90
P-H4	2.6699	28.1	5.1
P-H4	2.6699	28.1	264.9
Mg-OW1	2.1158	27.2	270
Mg-OW2	2.1125	29.3	270
Mg-OW31	2.0763	70.1	39.1
Mg-OW32	2.0763	70.1	140.9
Mg-OW41	2.0553	71.1	139.2
Mg-OW42	2.0553	71.1	40.8

Polar angle (θ) and azimuthal angle (ϕ) are relative to the crystallographic axes **b** and **a**, respectively.

4.3.4 Single-crystal EPR spectra of boussingaultite

Single-crystal EPR measurements show that synthetic boussingaultite does not contain any paramagnetic defect before gamma-ray irradiation but is characterized by three well-resolved arsenic-centered oxyradicals after irradiation ($[AsO_4]^{2-}$, $[AsO_3]^{2-}$ and $[AsO_2]^{2-}$; Fig. 4-8c). These three arsenic-centered oxyradicals are readily identified on the basis of their diagnostic ^{75}As hyperfine coupling constants (Table 4-2; Lin and McDowell, 1964; Serway and Marshall, 1966; Lin et al., 2013). Interestingly, the angular dependence of the experimental line positions (i.e., roadmaps) and the best-fit spin Hamiltonian parameters of the $[AsO_3]^{2-}$ radical in boussingaultite are almost identical to those of an $[AsO_3]^{2-}$ radical in arsenate-doped struvite reported by Xu (1992). Also, the same $[AsO_2]^{2-}$ radical (Fig. 4-8c) is visible in the **B**//**c** spectrum reported by Xu (1992). Moreover, a broad signal at the central magnetic field in the **B**//**c** spectrum reported by Xu (1992) corresponds to the well-resolved $[AsO_4]^{2-}$ radical in Figure 4-8c. These similarities lead us to suggest that "arsenate-doped struvite" investigated by Xu (1992) was most likely boussingaultite. Indeed, PXRD analyses demonstrate that crystals from my synthesis experiment using the same slow evaporation method (i.e., equal volumes of the equimolar solutions of $NH_4H_2PO_4$ and $MgSO_4$ with the addition of one molar percent $(NH_4)_3AsO_4$) are boussingaultite.

4.4 Insights into arsenate uptake in struvite

ICPMS analyses confirm that struvite formed under ambient conditions contains up to 547±15 ppm As. Moreover, modeling of synchrotron As K-edge EXAFS data and single-crystal EPR analyses of arsenic-centered oxyradicals demonstrate lattice-bound As in struvite. In particular, the angular dependences of the experimental EPR spectra of all five $[AsO_3]^{2-}$ radicals, including agreements between their experimental lines with both the site symmetries and the Laue crystal symmetry of struvite, rule out origins from As-bearing inclusions or surface absorbents. Moreover, the close matches in directions between the unique g and A(^{75}As) axes with specific P-O bonds of the $[PO_4]^{3-}$ group are unambiguous evidence for incorporation of As^{5+} at the P site in the struvite lattice. In addition, the observed ^{1}H superhyperfine structure of Center I (Fig. 4-8b and Table 4-4) provides further support for the location of As^{5+} at the P^{5+} site

in the struvite structure.

My results for the incorporation of up to 547±15 ppm As in struvite differ from those of Bothe and Brown (1999), who did not detect any solid solution between $Ca_5(AsO_4)_3(OH)$ and $Ca_5(PO_4)_3(OH)$ under ambient conditions. Elevated As contents in apatites from marine phosphorite deposits are well known (Smedley and Kinniburgh, 2002). The failure to detect any solid solution between $Ca_5(AsO_4)_3(OH)$ and $Ca_5(PO_4)_3(OH)$ in Bothe and Brown (1999) is most likely attributable to the PXRD technique of limited sensitivity. My observation of an enhanced As uptake in struvite with increasing pH in Series I experiments is consistent with the increased stability of $[AsO_4]^{3-}$ relative to $[HAsO_4]^{2-}$ and $[H_2AsO_4]^{-}$ at high pH in aqueous environments (Smedley and Kinnburgh, 2002; Reeder et al., 2006) but must be viewed with caution, because thermodynamic equilibrium was not demonstrated in my synthesis experiments.

The most salient feature from this combined synchrotron XAFS and EPR study is the exclusive incorporation of As^{5+} in struvite, irrespective of $Na_2HAsO_4{\cdot}7H_2O$ or $NaAsO_2$ as the source. In particular, the detection of only As^{5+} in struvite from Series II experiments demonstrates that As^{3+} is highly unfavorable in this mineral. Here As^{5+} in Series II experiments probably resulted from oxidation reaction(s) related to bacterial activity in the unsealed tubes (Lin et al., 2013). Other possible causes for the presence of As^{5+} in Series II experiments include 1) impurity in the starting material and 2) abiotic oxidation related to atmospheric O_2. The incorporation of only As^{5+} in struvite differs from the accommodation of mixed As^{3+} and As^{5+} in gypsum formed under similar experimental conditions (Lin et al., 2013).

Although my design for the single diffusion gel technique does not allow any control or monitoring of the oxidation state, the presence of mixed As^{3+} and As^{5+} species during my experiments is confirmed by the single-crystal EPR spectra of co-precipitated boussingaultite (Fig. 4-8c). The $[AsO_4]^{2-}$ and $[AsO_3]^{2-}$ radicals in boussingaultite, similar to their counterparts in struvite, are readily linked to the diamagnetic $[AsO_4]^{3-}$ group (i.e., forming from hole trapping on one of the four oxygen atoms for the former and electron trapping on the central As atom after removal of an oxygen atom for the latter), indicating the occurrence of As^{5+} (Pan, 2013) The $[AsO_2]^{2-}$ radical is known to form from the $[AsO_3]^{3-}$ group by electron trapping on the As $4p_z$ orbital (Table 4-2) after removal of an O atom, confirming the presence of As^{3+} (Pan, 2013). The

absence of any $[AsO_2]^{2-}$ radical in the EPR spectra of gamma-ray-irradiated struvite, considering the sensitivity of this technique (Weil and Bolton, 2007; Pan, 2013), suggests that As^{3+} in struvite, if present, is unlikely to exceed 1 ppm.

Local structural expansion beyond the first shell of substituting As^{5+} in struvite suggested by modeling of EXAFS data is also corroborated by EPR results. For example, the anisotropic component *b* from the ^1H superhyperfine structure of Center I, using the point-dipole model [$b = -(2\mu_0/4\pi)(g\beta_e g_n \beta_n/r^3)$, where $g_n = 5.5856912$ for ^1H], predicts As-H distances of 2.76 Å, which are significantly longer than those from P to the two nearest H atoms determined by neutron diffraction studies (2.67 Å; Ferrais et al., 1973).

Another interesting question is whether As^{5+} in struvite occupies the Mg octahedral site or not, because octahedral arsenate groups, albeit rare, have been reported to occur in synthetic compounds (Schwendtner and Kolitsch, 2007) and minerals (Groat et al., 2013). My EXAFS modeling suggests that as little as 5% As^{5+} at the octahedral site (As-O = 1.83 Å; Schwendtner and Kolitsch, 2007) would be visible in experimental spectra. The fact that none of the arsenic-centered oxyradicals is consistent with the orientation of the $Mg(H_2O)_6$ group (Tables 4-3 and 4-4) also refutes any accommodation of As^{5+} at the octahedral site in struvite, even at the level of the exceptionally sensitive EPR technique.

Finally the present study of arsenic-doped struvite formed under ambient conditions not only provides new insights into the mechanism of As^{5+} incorporation but also raises serious questions about the current use of this material as fertilizer. In particular, struvite precipitated from sewage and wastewater treatment plants, without removal of As (and other heavy metals and metalloids), is a potential source of contamination. My recognition of As^{3+} exclusion from struvite suggests that precipitation under reduced conditions is a possible route to minimize As.

4.5 References

Aguilera, I., Daponte, A., Gil, F., HernÃ¡ndez, A.F., Godoy, P., Pla, A., and Ramos, J.L. (2010) Urinary levels of arsenic and heavy metals in children and adolescents living in the

industrialised area of Ria of Huelva (SW Spain). *Environment International*, **36 (6)**, 563-569.

Arai, Y., Lanzirotti, A., Sutton, S., Davis, J.A., and Sparks, D.L. (2003) Arsenic speciation and reactivity in poultry litter. *Environmental Science & Technology*, **37 (18**), 4083-4090.

de-Bashan, L.E., and Bashan, Y. (2004) Recent advances in removing phosphorus from wastewater and its future use as fertilizer (1997-2003). *Water Research*, **38 (19)**, 4222-4246.

Biagioni, C., Pasero, M. (2013) The crystal structure of johnbaumite, $Ca_5(AsO_4)_3OH$, the arsenate analogue of hydroxylapatite. *American Mineralogist*, **98**, 1580-1584.

Bothe, J. V., Brown, P. W. (1999) Arsenic immobilization by calcium arsenate formation. *Environmental Science and Technology*, **33 (21)**, 3806-3811.

Chand, P., Agarwal, O. P. (1991) Electron paramagnetic resonance study of doped synthetic crystals of struvite and its zinc analogue. *Spectrochimica Acta Part A*, **47 (6)**, 775-783.

Chen, N., Jiang, D. T., Cutler, J., Kotzer, T., Jia, Y. F., Demopoulos, G. P., and Rowson, J. W. (2009) Structural characterization of poorly-crystalline scorodite, iron(III)-arsenate co-precipitates and uranium mill neutralized raffinate solids using X-ray absorption fine structure spectroscopy. *Geochimica et Cosmochimica Acta*, **73 (11)**, 3260-3276.

Dalal, N. S., Dickson, J. R., McDowell, C. A. (1972) Electron paramagnetic resonance studies of X-irradiated KH_2AsO_4, KD_2AsO_4, RbH_2AsO_4, RbD_2AsO_4, CsH_2AsO_4, $NH_4H_2AsO_4$, and $ND_4D_2AsO_4$ (ferroelectrics and antiferroelectrics). *Journal of Chemical Physics*, **57 (10)**, 4254-4265.

Doyle, J.D., and Parsons, S.A. (2002) Struvite formation, control and recovery. *Water Research*, **36 (16)**, 3925-3940.

Driver, J., Lijmbach, D., and Steen, I. (1999) Why recover phosphorus for recycling, and how? *Environmental Technology*, **20 (7)**, 651-662.

El Diwani, G., El Rafie, S., El Ibiari, N.N., and El-Aila, H.I. (2007) Recovery of ammonia nitrogen from industrial wastewater treatment as struvite slow releasing fertilizer. *Desalination*, **214 (1-3)**, 200-214.

Edwards, P. R., Subramanian, S., Symons, M. C. R. (1968) Electron spin resonance studies of vanadate, niobate, phosphate, and arsenate in γ-irradiated calcium molybdate and calcium tungstate. *Chemical Communications (London)*, 799-799.

Feng, R., Gerson, A., Ice, G., Reininger, R., Yates, B., McIntyre, S. (2007) VESPERS: a beamline for combined XRF and XRD measurements. *AIP Conference Proceedings*, **879**, 872-874.

Ferraris, G., Fuess, H.; Joswig, W. (1986) Neutron diffraction study of $MgNH_4PO_4 \bullet 6H_2O$ (struvite) and survey of water molecules donating short hydrogen bonds. *Acta Crystallographica*, **B42**, 253-258.

Frost, R.L., Weier, M.L., and Erickson, K.L. (2004) Thermal decomposition of struvite implications for the decomposition of kidney stones. *Journal of Thermal Analysis and Calorimetry*, **76(3)**, 1025-1033.

Foster A.L., Brown G.E., Tingle T.N., and Parks G.A. (1998) Quantitative arsenic speciation in mine tailings using X-ray absorption spectroscopy. *American Mineralogist*, **83**, 553-423.

Gilinskaya, L. G., Afanas'eva, V. I. (1981) Two forms of the AsO_3^{2-} radical in γ-irradiated heidingerite $CaHAsO_4 \cdot H_2O$. *Journal of Structural Chemistry*, **22 (4)**, 640-642.

Groat, L. A., Evans, J., J, C., McCammon, C., Houzar, S. (2013) Fe-rich and As-bearing vesuvianite and wiluite from Kozlov, Czech Republic. *American Mineralogist*, **98**, 1330-1337.

Henisch, H. K. (1970) Crystal growth in gels. *The Pennsylvania State Press, University Park*

Henisch, H. K., Dennis, J., and Hanoka, J. I. (1965) Crystal growth in gels. *Journal of Physics and Chemistry of Solids.* **26 (3)** 493-496

Hunger, S., Sims, J.T., and Sparks, D.L. (2008) Evidence for Struvite in Poultry Litter: Effect of storage and drying. *Journal of environmental quality*, **37 (4)**, 1617-1625.

Jaffer, Y., Clark, T.A., Pearce, P., and Parsons, S.A. (2002) Potential phosphorus recovery by struvite formation. *Water Research*, **36 (7)**, 1834-1842.

Jiang, D.T., Chen, N., Demopoulos, G.P., and Rowson, J.W. (2010) Response to the comment by D. Paktunc on "Structural characterization of poorly-crystalline scorodite, iron(III)-arsenate co-precipitates and uranium mill neutralized raffinate solids using X-ray absorption fine structure spectroscopy", *Geochimica et Cosmochimica Acta*, **74**, 4597-4602

Kim, E., Chen, N., Arthur, Z., Warner, J., Demopoulos, G. P., Rowson, J. W. and Jiang, D. T (2013) Multiple scattering Debye-Waller factors for arsenate. *Journal of Physics: Conference Series,* **430**, 012086.

Kitahama K., Kiriyama R., and Baba Y. (1975) Refinement of the crystal structure of scorodite. *Acta Crystallographica Section B*, **31**, 322-324.

Le Corre, K.S., Valsami-Jones, E., Hobbs, P., and Parsons, S.A. (2009) Phosphorus recovery from wastewater by struvite crystallization: A review. *Critical Reviews in Environmental Science and Technology*, **39 (6)**, 433-477.

Lee, Y. J., Stephens, P. W., Tang, Y.; Li, W., Phillips, B. L., Parise, J. B., Reeder, R. J. (2009) Arsenate substitution in hydroxylapatite: Structural characterization of the $Ca_5(P_xAs_{1-x}O_4)_3OH$ solid solution. *American Mineralogist*, **94 (5-6)**, 666-675.

Lin, J., Chen, N., Nilges, M.J., and Pan, Y. (2013) Arsenic speciation in synthetic gypsum ($CaSO_4.2H_2O$): A synchrotron XAS, single-crystal EPR and pulsed ENDOR study. *Geochimica et Cosmochimica Acta*, **106**, 524-540.

Lin, J., Pan, Y., Chen, N., Mao, M., Li, R., and Feng, R. (2011) Arsenic incorporation in colemanite from borate deposits: Data from ICP-MS, micro-S-XRF, XAS and EPR analyses. *Canadian Mineralogist*, **49**, 809-822.

Lin W. C., and McDowell C. A. (1964) Electron spin resonance of an X-ray irradiated single crystal of disodium hydrogen arsenate, $Na_2HAsO_4.7H_2O$. *Molecular Physics*, **7**, 223-234.

Mao, M.; Lin, J.; Pan, Y. (2010) Hemimorphite as a natural sink for arsenic in zinc deposits and related mine tailings: Evidence from single-crystal EPR spectroscopy and hydrothermal synthesis. *Geochimica et Cosmochimica Acta*, **74**, 2943-2956.

Moldovan, B.J., Jiang, D.T., and Hendry, M.J. (2003) Mineralogical characterization of arsenic in uranium mine tailings precipitated from iron-rich hydrometallurgical solutions. *Environmental Science & Technology*, **37 (5)**, 873-879.

Negrea, A., Lupa, L., Negrea, P., Ciopec, M., and Muntean, C. (2010) Simultaneous removal of ammonium and phosphate ions from wastewaters and characterization of the resulting product. *Chem. Bull. "POLITEHNICA" Univ. (Timisoara)*, **55(69)**, 2, 136-142.

Pan, Y. (2013) Arsenic speciation in rock-forming minerals determined by EPR spectroscopy. In *Arsenic: Sources, Environmental Impacts, Toxicity and Human Health: A Medical Geology Perspective*; Masotti, A., Ed.; Nova Science Publishers Inc, 39-52.

Pan, Y., Fleet, M. E. (2002) Compositions of the apatite-group minerals: Substitution mechanisms and controlling factors. *Reviews in Mineralogy and Geochemistry*, **48 (1)**, 13-49.

Parsons, S.A., and Smith, J.A. (2008) Phosphorus removal and recovery from municipal wastewaters. *Elements*, **4(2)**, 109-112.

Patel, A. R. and Rao, A. V. (1982) Crystal growth in gel media. *Bulletin of Materials Science*, **4(5),** 527-548

Perera, P.W.A., Han, Z.-Y., Chen, Y.-X., and Wu, W.-X. (2007) Recovery of nitrogen and phosphorous as struvite from swine waste biogas digester effluent. *Biomedical and Environmental Sciences*, **20(5)**, 343-350.

Pöppl, A; Tober, O., Völkelel, G. (1994) ESR study of the AsO_3^{2-} radical in γ-irradiated betaine arsenate. *Physica Status Solidi B*, **183**, K63-K66.

Rahaman, M.S. (2009) Phosphorus recovery from wastewater through struvite crystallization in a fluidized bed reactor: kinetics, hydrodynamics and performance. PhD these Civil Engineering, University of British Columbia, Vancouver, BC.

Rao, S. N., Sivaprasad, P., Reddy, Y. P. (1991) Optical absorption studies on cobalt doped struvite. *Radiation Effects and Defects in Solids*, **116 (4)**, 369-373.

Ravikumar, R. V. S. S. N., Madhu, N.; Reddy, B. J., Reddy, Y. P., Rao, P. S. (1997) Spectroscopic investigations on vanadyl doped cadmium struvite. *Physica Scripta*, **55 (5)**, 637.

Reeder, R. J., Schoonen, M. A. A., Lanzirotti, A. (2006) Metal speciation and its role in bioaccessibility and bioavailability. *Reviews in Mineralogy and Geochemistry*, **64 (1)**, 59-113.

Rehr, J.J. and Albers, R.C. (2000) Theoretical approaches to x-ray absorption fine structure. *Reviews of Modern Physics*, **72**, 621-654.

Ressler, T. (1997) WinXAS: A new software package not only for the analysis of energy-dispersive XAS data. *Journal de Physique IV*, **7 (C2)**, 269-270.

Ronteltap, M., Maurer, M., and Gujer, W. (2007) The behaviour of pharmaceuticals and heavy metals during struvite precipitation in urine. *Water Research*, **41 (9)**, 1859-1868.

Schwendtner, K., Kolitsch, U. (2007) Octahedral As in M^+ arsenates-architecture and seven new members. *Acta Crystallographica*, **B63 (2)**, 205-215.

Serway R. A. and Marshall S. A. (1966) Electron spin resonance absorption spectrum of the AsO_3^{2-} molecule ion in γ–irradiated single–crystal calcite. *Journal of Chemical Physics*, **45 (6)**, 2309-2314.

Sivaprasad, P., Ramesh, K., Reddy, Y. P. (1990) Optical and EPR studies of Cu^{2+} in

$MgNH_4PO_4 \cdot 6H_2O$. *Physica Status Solidi A*, **118 (2)**, K103-K106.

Smedley, P.L., and Kinniburgh, D.G. (2002) A review of the source, behaviour and distribution of arsenic in natural waters. *Applied Geochemistry*, **17 (5)**, 517-568.

Sohel, N., Kanaroglou, P.S., Persson, L.A., Haq, M.Z., Rahman, M., and Vahter, M. (2010) Spatial modelling of individual arsenic exposure via well water: evaluation of arsenic in urine, main water source and influence of neighbourhood water sources in rural Bangladesh. *Journal of Environmental Monitoring*, **12 (6)**, 1341-1348.

Sougandi, I., Venkatesan, R., Rajendiran, T. M., Rao, P. S. (2003) Identification of VO(II) at substitutional and interstitial locations in magnesium ammonium phosphate hexahydrate: A single crystal EPR study. *Physica Scripta*, **67 (2)**, 153.

Subramanian, S., Murty, P. N., Murty, C. R. K. (1977) EPR studies of some arsenic and phosphorus oxyradicals. *Journal of Physics and Chemistry of Solids*, **38**, 825-829.

Tünay, O., Kabdasli, I., Orhon, D., and Kolçak, S. (1997) Ammonia removal by magnesium ammonium phosphate precipitation in industrial wastewaters. *Water Science and Technology*, **36(2-3)**, 225-228.

Uysal, A., Yilmazel, Y.D., and Demirer, G.N. (2010) The determination of fertilizer quality of the formed struvite from effluent of a sewage sludge anaerobic digester. *Journal of Hazardous Materials*, **181(1-3**), 248-254.

Xu, R. (1992) EPR studies of AsO_3^{2-} centers in $MgNH_4PO_4 \cdot 6H_2O$ (struvite) crystals. *physica status solidi (b)*, **172(1)**, K15-K18.

Zhang, W., and Lau, A. (2007) Reducing ammonia emission from poultry manure composting via struvite formation. *Journal of Chemical Technology & Biotechnology*, **82(6)**, 598-602.

Weil, J. A., and Bolton, J. R. (2007) Electron Paramagnetic Resonance: Elementary Theory and Practical Applications, 2rd, ed.; John Wiley & Sons: New York.

Weil, M. (2008) The struvite-type compounds M $[Mg(H_2O)_6](XO_4)$, where M = Rb, Tl and X = P, As. *Crystal Research and Technology*, ***43*** **(12)**, 1286-1291.

CHAPER 5

Arsenic speciation in newberyite ($MgHPO_4•3H_2O$) determined by synchrotron XAS and single-crystal EPR spectroscopy: Implications for green fertilizers

5.1 Introduction

Phosphorus (P) is an element of fundamental importance to humans for the creation of energy in cells, control of metabolic reactions and, as an essential nutrient for crops, promotion of food production (Smil, 2000; Valsami-Jones, 2004). Phosphidic deposits are a primary source of P and are commonly used as fertilizers for agriculture (Cordell et al., 2009). In this context, phosphorus is a non-renewable resource. Global phosphate reserves are limited and, at the present rate of consumptions, the existing phosphate reserves could be exhausted in less than 100 years (Cordell et al., 2009; Isherwood, 2000; Runge-Metzger, 1995; Smil, 2000; Steen, 1998). Other phosphate-rich rocks are available but cannot be extracted economically at present due to their low qualities and hence high processing costs (Cordell et al., 2009). Therefore, phosphorus recovery from wastes as a renewable source is considered to be an important alternative in reducing our reliance on limited natural resources and relieving the pressure of increasing demands of phosphorus consumptions.

One commercial technology for recovering P from wastewaters is chemical precipitation of inorganic magnesium phosphates such as struvite ($Mg(NH_4)PO_4·6H_2O$) and newberyite ($MgHPO_4•3H_2O$) (Cordell et al., 2009; Muster et al., 2013; Sartorius et al., 2011). Of these magnesium phosphates, struvite or "Crystal Green" (a commercial slow-release fertilizer) is particularly promising to the problem of both phosphorus and nitrogen recovery (Ali, 2005; Bhuiyan et al., 2008; Cordell et al., 2009; Jaffer et al., 2002; Kern et al., 2008; Le Corre et al., 2009; Muster et al., 2013; Shu et al., 2006). This fertilizer is formulated from struvite pellets recovered from waterwaters in nutrient recovery facilities. However, struvite formed from this process commonly contains elevated levels of various heavy metals and metalloids, which are common in wastewaters (Buj et al., 2009; Kern et al., 2008; Ronteltap et al., 2007). Our recent study in chapter 4 confirmed that struvite precipitated under ambient conditions is capable of accommodating up to 547±15 ppm As (Lin et al., 2013b). Therefore, precipitation of struvite from wastewaters is, on the one hand, a useful method for minimizing and removing As

contamination (Ronteltap et al., 2007; Uysal et al., 2010). On the other hand, direct use of struvite as a fertilizer, without removal of heavy metals and metalloids, presents a potential source of As contamination.

Newberyite of the space group *Pbca* (Fig. 5-1) often co-precipitates with struvite in urine as well as calculi (Abbona et al., 1982; Babić-Ivančić et al., 2004; Babić-Ivančić et al., 2006; Boistelle et al., 1983; Kontrec et al., 2005; Williams et al., 2012) and is a common component in "Crystal Green" recovered from wastewaters. In addition, newberyite has long been known to transform from struvite under both subaerial and aqueous environments (Cohen and Ribbe, 1966; Whtaker, 1968, 1969). For example, at room temperature, struvite would completely decompose subaerially to newberyrite after approximately half a year (Whtaker, 1968). Therefore, the question of arsenic uptake and speciation in newberyite is of significant importance to not only the manufacture of green fertilizers from wastewaters but also understanding the fate of this toxic metalloid in soils.

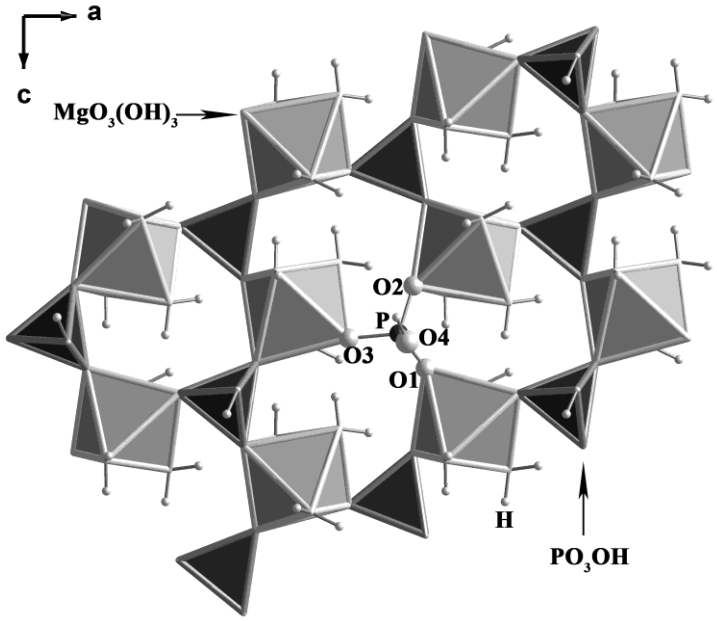

Figure 5-1 The crystal structure of newberyite projected onto (010) (data from Bartl et al., 1983), showing the local environment of phosphorus.

This chapter investigates arsenic doped newberyite using of synchrotron X-ray absorption spectroscopy (XAS) and single-crystal electron paramagnetic resonance (EPR) spectroscopy.

These results are compared with those from struvite and other phosphates to provide insights into the uptake and speciation of arsenic in newberyite. Also investigated in this study are representative samples of natural newberyite from Skipton caves, Australia and Paoha island, Mono Lake, California, both which are well known occurrences of newberyite as a pseudomorph after struvite. Data from natural newberyite are interpreted in light of new experimental results from its synthetic counterpart, with implications for green fertilizers.

5.2 Materials and analytical methods

5.2.1 Synthesis and growth of single crystals of As-doped newberyite

Single crystals of arsenic doped newberyite have been grown by the gel diffusion technique, similar to that used in the synthesis of struvite (Lin et al., 2013b). Approximately 20 mL sodium metasilicate (Na_2SiO_3) solution with a density of 1.05 g/cm^3 mixed with 0.25 M potassium dihydrogen phosphate ($K_2H_2PO_4$) and 0.005 M sodium hydrogen arsenate heptahydrate ($Na_2HAsO_4 \cdot 7H_2O$), were first adjusted to pH = 6.4 by using acetic acid, and were then poured into a test tube to form a gel. After the gel settled down, 10 mL solution of 0.5 M $Mg(CH_3COOH)_2$ was added into the tube. Crystals were obtained after 2 months and, after washing with deionized water, have been investigated by powder X-ray diffraction (PXRD), inductively coupled plasma mass spectrometry (ICPMS), As K edge synchrotron X-ray absorption spectroscopy and electron paramagnetic resonance (EPR) spectroscopy.

5.2.2 Samples of natural newberyite

Four samples of natural newberyite (2 each from Paoha island, Mono Lake, California, USA and Skipton, western Victoria, Australia) have investigated using PXRD, ICPMS and powder EPR analyses. Mono Lake in eastern California is a closed lake within a basin without any outlet to oceans. It is a hypersaline and alkaline water body that contains exceptionally high concentrations of arsenic (averaging ~200 µM; Oremland et al., 2004; Kulp et al., 2008; Wolfe-Simon et al., 2011). Because the prohibitive environment eliminates aquatic predators and competition, Mono Lake offers unusually productive food in the form of brine shrimp and alkali

flies, which feeds millions of migratory and nesting birds. The guano deposits on the Paoha island in Mono Lake are thought to accumulate from bird droppings. Two samples of newberyite from Paoha Island, Mono Lake, are similar to those described in the literature and possess well-preserved morphologies of struvite, indicative of pseudomorph after the latter (Cohen and Ribbe, 1966). Similarly, the two samples of newberyite from bat caves in Skipton, Australia are similar to those described in the literature and are pseudomorphs after struvite from bats' droppings (Ollier, 1963; Bridge, 1971; Frost et al., 2012).

5.2.3 Arsenic K edge XAS measurements

The As K-edge (11867eV) spectra were collected at HXMA beamline of Canadian Light Source (CLS) (Jiang et al., 2010) with a storage ring operated at 2.9 GeV. The monochromatic beam was produced using a pair of Si(111) monochromator crystals with the second crystal detuned by 50% of fully tuned beam intensity for reduction of harmonic and Rh mirrors was introduced in this experiment. Synthetic newberyite sample was mounted in an aluminium holder covered with kapton at 45^0 to incident X-ray beam and measured in fluorescence detection using a 32-elements solid state Ge detector positioned at 90^0 to the X-ray beam. The sample was held at 8K using an Oxford Instruments liquid helium flow cryostats to reduce the beam damage, and straight ion chamber detectors filled with standard 100% nitrogen gas. The photon energy was calibrated by an Au foil with the first derivation of the absorption edge assigned a value of 11919 eV at Au L3 edge. Spectra of model compounds were obtained in a previous study using transmission methods (Lin et al., 2013a). Three spectra were collected with the sizes of scan steps for the pre-edge, XANES, and EXAFS regions of 10 eV/step, 0.25 eV/step, and 0.05 $Å^{-1}$/step, respectively.

5.2.4 X-band EPR measurements

One selected single crystal of arsenic-doped newberyite was irradiated at room temperature in a ^{60}Co cell, with a dose rate of ~460 Gy/h, for 2 days, for detailed single-crystal EPR measurements in three rotation planes at an interval of 5º each step. These single-crystal EPR measurements were made at room temperature on a Bruker EMX instrument at the

Saskatchewan Structure Sciences Centre, University of Saskatchewan. The microwave power of ~5 mW, modulation frequency of 100 kHz and modulation amplitude of 0.1 mT were used for data collection. Among the three rotation planes, two are nearly parallel to the (010) crystal face and one is approximately parallel to (011) with microwave frequency of ~ 9616 and 9856 GHz, respectively. The spectral resolution of single-crystal EPR spectra was 0.098 mT (i.e., 2048 data points over the scan range from 207 to 407 mT).

Powder EPR spectra of natural and synthetic newberyite were also measured at room temperature after gamma-ray irradiations for 7 days and 2 days, respectively, at the dose rate of ~460 Gy/h.

5.3 Results and discussion

5.3.1 Characterization of synthetic and natural newberyite

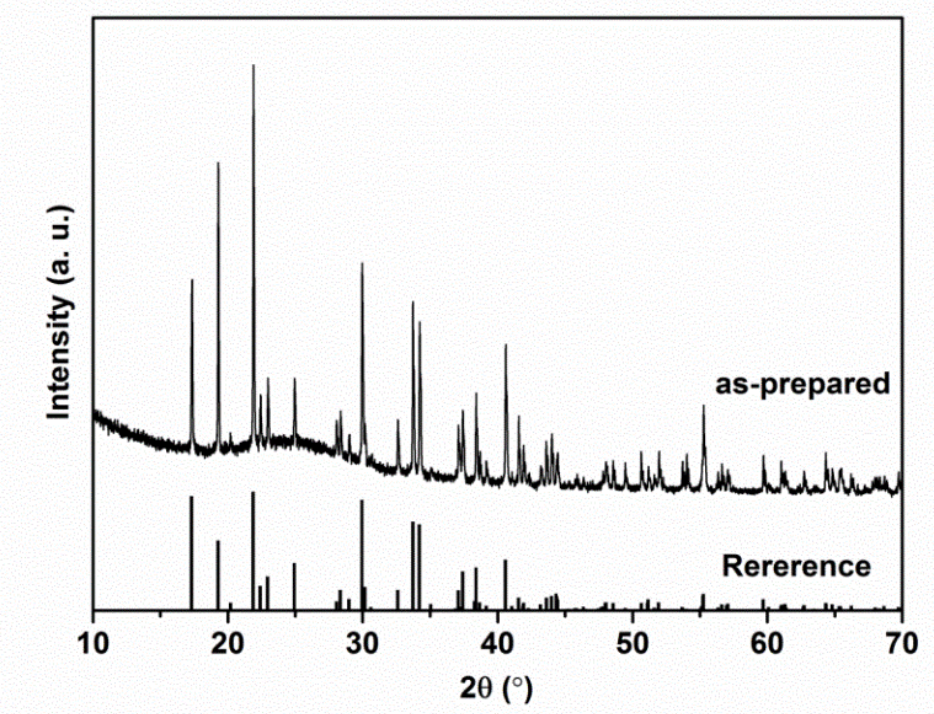

Figure 5-2 Powder X-ray diffraction pattern of synthetic newberyite in comparison with reference.

Synthetic newberyite crystals are characterized by well-developed prismatic and dipyramidal morphologies and have the maximum size of 2 mm × 1 mm ×1 mm. Several of these crystals were pulverized for powder X-ray diffraction (PXRD) analysis to confirm the experimental products to be pure newberyite (Abbona et al., 1979) (Fig. 5-2). An ICPMS analysis of the pulverized material, after dissolution in HF-HNO_3, showed synthetic newberyite to contain 1099 ppm As.

PXRD analyses of the four samples of natural newberyite confirm that they all contain a single phase within the detection limit of this technique. ICPMS analyses show that the two samples from Skipton bat caves contain 2-3 ppm As, whereas one sample from Paoha Island contains 6.7 ppm As. All four samples of natural newberyite are characterized by elevated concentrations of various transition metals (Table 5-1).

Table 5-1 ICPMS results of natural newberyite samples

Newberyite Samples	As (ppm)	Fe (ppm)	Mn (ppm)	Cu (ppm)	Zn (ppm)	Ni (ppm)	Cr (ppm)
#1 Skipton Caves	3.0	833	5746	27	478	4.0	4.1
#2 Skipton Caves	2.7	878	5755	27	480	4.1	3.9
#3 Paoha Island	2.0	63	150	1.3	2.7	2.4	1.1
#4 Paoha Island	6.7	106	210	0.1	3.0	2.0	1.6

5.3.2 Arsenic K edge XANES and EXAFS spectra of synthetic newberyite

Figure 5-3a shows the near-edge regions of the As K edge X-ray absorption spectra of the model compounds and the synthetic newberyite sample. The dominated whiteline peak position of synthetic newberyite at ~11,874 eV is consistent with those of scorodite and As_2O_5, suggesting the presence of the As^{5+} oxidation state only, which is evident in the first-derivative spectra as well (Fig. 5-3b).

Figure 5-4 shows the As K edge EXAFS spectrum $k^3 \bullet \chi(k)$ of synthetic newberyite and the R-space curve fits of its Fourier transform. In this study, individual EXAFS scans were first checked for energy calibration (and subtraction of bad spectra in some channels) and then

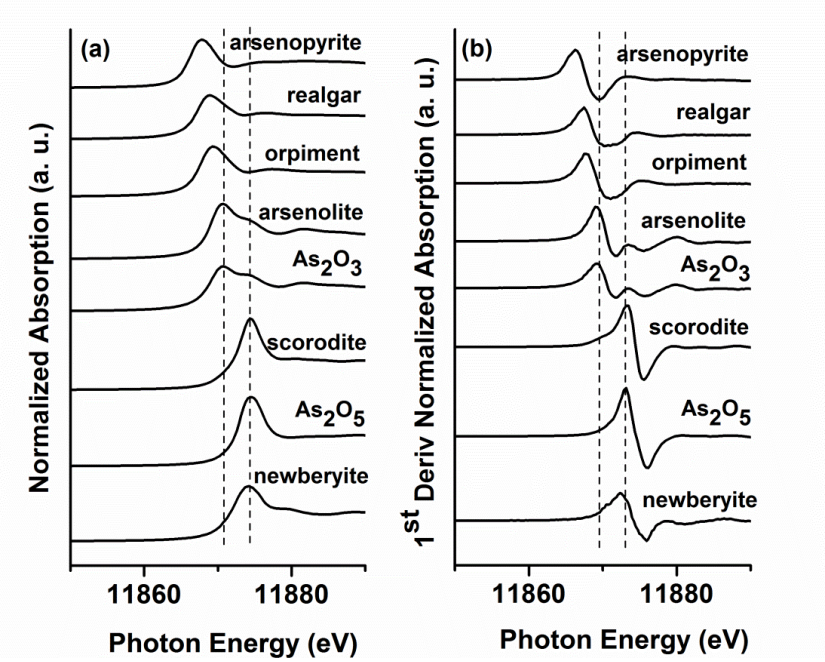

Figure 5-3 (a) As K edge XANES spectra of model compounds and synthetic newberyite; and (b) corresponding first-derivative XANES spectra.

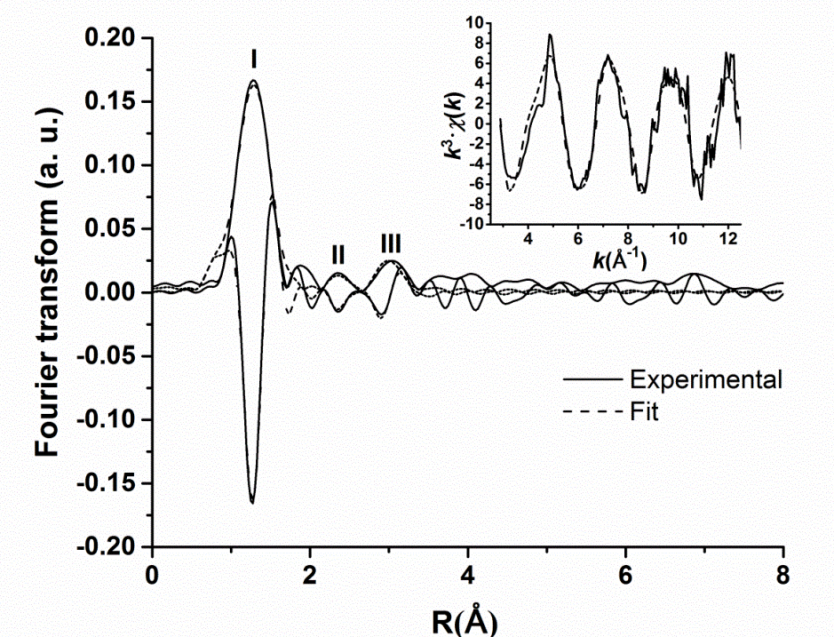

Figure 5-4 R-space curve fittings for As K edge EXAFS spectra of synthetic newberyite. The Fourier transforms of $k^3 \bullet \chi(k)$ spectra were performed over the k ranges of 2.89-13.08 Å^{-1} and R-space fitting windows of 0.83-3.38 Å. Both the magnitude (positive envelopes) and the imaginary (oscillating parts) of the Fourier transforms are shown. Also included in inserts are the $k^3 \bullet \chi(k)$ spectra in comparison with those from R-space fittings

merged. Data analysis included background subtraction using a linear pre-edge function, normalization and conversion to *k* space followed by using a cubic spline fit for μ(0) with k^3weighting. The k^3-weighted spectrum was Fourier transformed with a 30% Gaussian window function over the *k* space range of 2.89-13.08 $Å^{-1}$. All fits were done in R-space using the program Winxas 3.2 (Ressler, 1997), while theoretical phases and backscattering amplitudes were performed by FEFF6 (Rehr and Albers, 2000).

The As K edge EXAFS of synthetic newberyite is dominated by back-scattering from an O first shell at ~ 1.30 Å (labeled as I, not corrected for phase shift), with additional contributions from two smaller shells at 2.37 and 3.05 Å (II and III in Fig. 5-4). A single O first shell was used for initial fittings. Attempts to fit the shell III by assuming both As-Mg back-scattering and an outer As-O back-scattering at the radial distance of ~3.4 Å yielded unsatisfactory results with a double increment in the calculated residual. This might be caused by the unsolved shell II arising from interferences of multiple scatterings within the AsO_4 tetrahedron (i.e., As-O-O, As-O-As-O, et al.). A subsequent fitting, following the approach of Kim et al. (2013), included 3 types of multiple scatterings occurring in the AsO_4 tetrahedron. This fitting reproduced the main features in the experimental EXAFS data and yielded reasonable parameters. In detail, a single threshold energy (ΔE0) was allowed to vary during the fitting, and the amplitude reduction factor (S_0^2) was fixed at a value of 0.83. Following Kim et al. (2013), the Debye-Waller factors (σ^2) for the back-scattering paths were constrained, namely the $\sigma^2_{As\text{-}O1\text{-}O2}$ and $\sigma^2_{As\text{-}O1\text{-}As\text{-}O1}$ were correlated to that of the As-O scattering in the first shell by factors of 2 and 4, respectively. Similarly, the $\sigma^2_{As\text{-}O1\text{-}As\text{-}O2}$ path was changed by a factor of 2 to 4 to that of the As-O path (Kim et al., 2013). This fitting confirms that Region II is dominated by multiple scatterings in the AsO_4 tetrahedron and Region III is mainly contributed by the outer As-Mg and As-O paths.

Table 5-2 shows that the fitted interatomic distance of the arsenic species in synthetic newberyite is 1.68 Å, in agreement with those of typical As^{5+} (Foster et al., 1998; Kitahama et al., 1975; Moldovan et al., 2003). Also, the fitting results for the outer three single scattering As-Mg and As-O paths are consistent with the extended phosphorous site symmetry in newberyite. These results suggest that As^{5+} occurs as a substitution for P^{5+} in the newberyite structure.

Table 5-2 Local environments of As from R-space fittings of As K edge EXAFS data in synthetic newberyite.

Sample	Paths	CN	R(Å)	σ^2(Å^2)	Residual
Newberyite	As-O	4[a]	1.68(2)	0.0020(15)	12.64
	As-O1-O2	12[a]	3.03(2)	0.0040(15)	
	As-O1-As-O1	4[a]	3.26(2)	0.0080(15)	
	As-O1-As-O2	12[a]	3.16(2)	0.0041(15)	
	As-Mg	3[a]	3.38(2)	0.0081(31)	
	As-O	3(2)	3.45(2)	0.0090(50)	

a denotes fixed values.

5.3.3 Single-crystal X-band EPR spectra

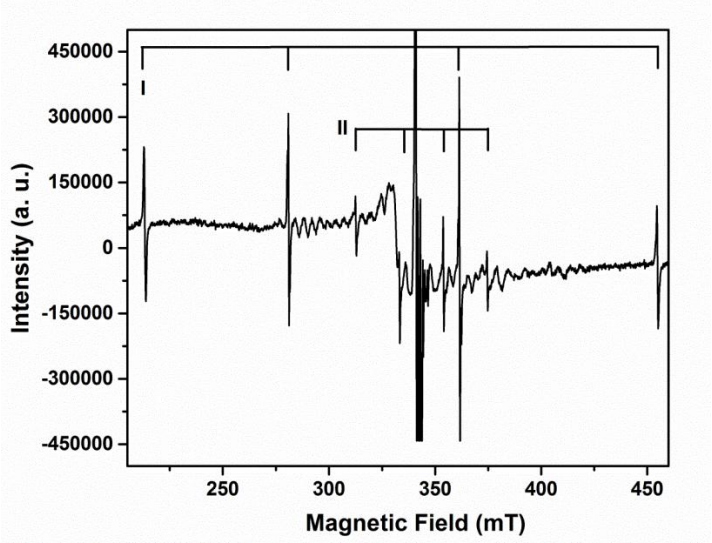

Figure 5-5 Single-crystal EPR spectrum of gamma-ray-irradiated newberyite measured with the magnetic field **B** approximately parallel to the crystallographic axis **c**, showing two centers with characteristic ^{75}As hyperfine structures (labeled I and II)

Single-crystal EPR spectra of gamma-ray-irradiated of newberyite gave two distinct sets of hyperfine lines (I and II in Fig. 5-5), both arising from interactions between an unpaired electron (S=1/2) and an ^{75}As nucleus (I=3/2 and a natural isotope abundance of ~100%). Center I has relatively large but unequal splittings from ~48 mT to ~94 mT. Each hyperfine line of this

species, with an average linewidth of ~0.7 mT, is split into at most four at random crystal orientations (Fig. 5-6a,b), indicative of a triclinic site symmetry in orthorhombic newberyite. Center II, which is much weaker in intensity than Center I (~19%), has an average linewidth of ~0.3 mT and is characterized by splittings between ~9 mT and ~21 mT (Fig. 5-6c,d). One additional set of hextet hyperfine lines with the splittings of ~9 mT is readily attributable to $^{55}Mn^{2+}$. Also present in the central magnetic field are strong but uncharacterized lines (Fig. 5-5).

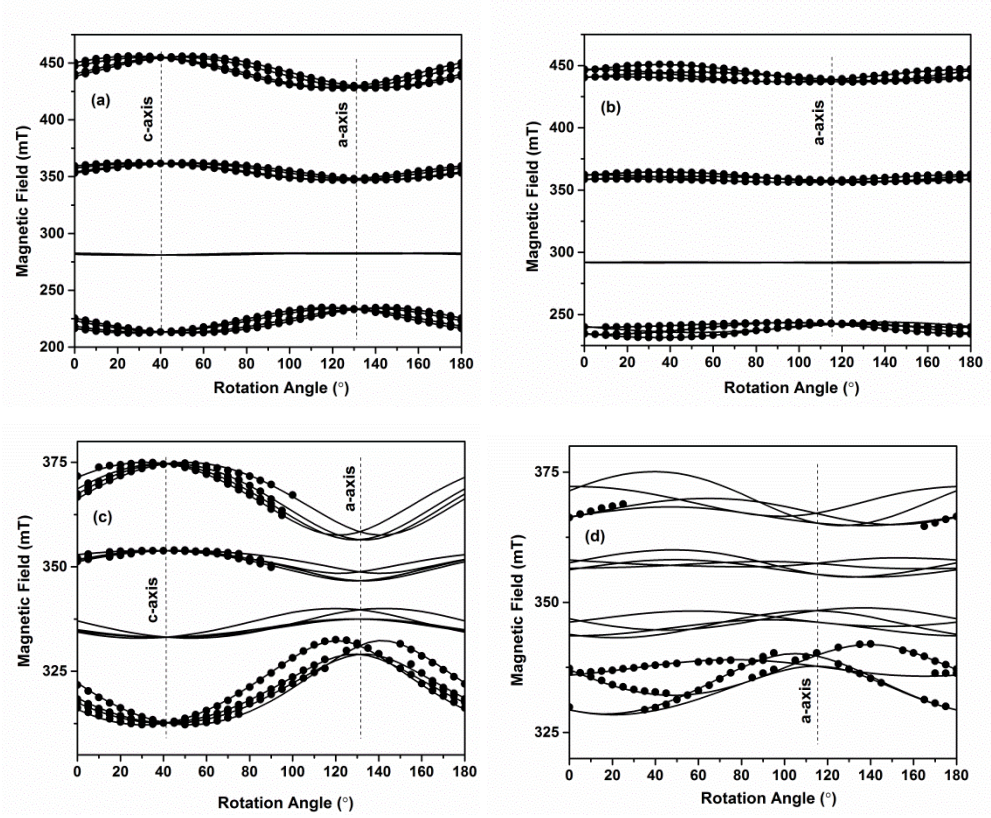

Figure 5-6. Representative angular dependences of line positions (i.e., roadmaps) of Centers I (a and b) and Center II (c and d): (a and c) approximately parallel to the (010) crystal face, and b and d are nearly parallel to the (011) crystal face.

The EPR spectra of Centers I and II can be described in terms of a spin-Hamiltonian of the form

$$H_s = \beta_e \mathbf{S \cdot g \cdot B} + \mathbf{I \cdot A \cdot S} + \mathbf{I \cdot P \cdot I} - \beta_n \mathbf{I} \cdot g_n \cdot \mathbf{B}$$

Where β_e and β_n are the electronic (Bohr) and nuclear magnetons, respectively; **S** and **I** are the electron spin and nuclear spin operators, respectively; **g** is the Zeeman electron term; **B** is the external magnetic field; and **A** and **P** are the hyperfine and quadrupole terms for the ^{75}As nucleus

with an isotropic g_n value of 0.959647. The line-position data of Centers I and II in newberyite have been analyzed with the rotation group *D*2 with the experimental axes **z** and **x** along the crystallographic axes **b** and **a**, respectively. The total number of line-position data points for Center I and Center II were 1246 and 501, respectively. The final values of the root-mean-squares of weighed differences (RMSD) between the calculated and observed line positions for Centers I and II are 0.127 mT and 0.257 mT, respectively (Table 5-3).

The characteristic ^{75}As hyperfine coupling constants (Table 5-4) suggest that Center I is an As-associated oxyradical of the type $[AsO_3]^{2-}$ (Pan, 2013, Lin et al., 2013a,b). The orientations of the principal g_2 and A_1 axes of Center I are approximately along the P-O2 bond direction (74.5°, 286.8°) (Fig. 5-1; Table 5-5). The orientations of the g_1 and g_3 axes of Center II are nearly perpendicular to the P-O1-O2 plane (39.8°, 182.7°) and P-O2-O4 plane (78.5°, 19.2°) (Table 5-5), respectively. Moreover, the A_1 and A_3 axes are almost along the directions of the P-O2 bond (74.5°,286.8°) and the P-O3 bond (81.8°, 174.6°) (Fig. 5-1; Table 5-5), respectively. The close matches of these orientations suggest that the $[AsO_3]^{2-}$ radical formed from the diamagnetic $[AsO_4]^{3-}$ group substituting for the $[PO_4]^{3-}$ group in the newberyite lattice. The formation mechanism of the $[AsO_3]^{2-}$ radical involves trapping of an electron on the central As^{5+} ion after removal of an O atom during gamma ray irradiation:

$$[PO_4]^{3-} \rightarrow [AsO_4]^{3-} \quad (5\text{-}1)$$

$$[AsO_4]^{3-} \xrightarrow{hv} [AsO_3]^{2-} + O^{2-} + e^- \quad (5\text{-}2)$$

Similarly, the best-fit ^{75}As hyperfine coupling constants suggest that Center II is an As-associated oxyradical of the type $[AsO_2]^{2-}$ (Table 5-4; Pan, 2013; Lin et al., 2013a). The $[AsO_2]^{2-}$ radicals in various crystalline hosts have been interpreted to originate from the diamagnetic $[AsO_3]^{3-}$ precursor, involving trapping of an unpaired electron on the As $4p_z$ orbital after removal of an O atom during gamma ray irradiation. The orientations of the principal *g* and *A* axes of the $[AsO_2]^{2-}$ center in newberyite also match closely to the P-O bond directions or perpendicular to the P-O-O planes, suggesting a substitutional As^{3+} ion at the P site.

Table 5-3. Spin Hamiltonian parameters of arsenic-associated oxyradicals in synthetic newberyite at 295 K

	Matrix (Y)			k	Principal value/direction			RMSD (mT)
					Y_k	θ_k(°)	φ_k(°)	
Center I ($[AsO_3]^{2-}$)								
	2.00304(5)	0.00023(4)	-0.00246(4)	1	2.00533(5)	47.9(6)	188.5(8)	
g		2.00126(5)	-0.00041(5)	2	2.00124(5)	92(2)	101(2)	
			2.00256(8)	3	2.00029(5)	137.7(7)	194(4)	
A(^{75}As)	64.361(8)	-3.064(5)	0.294(5)	1	80.537(6)	82.28(2)	280.86(1)	0.127
(mT)		79.646(6)	-2.196(6)	2	63.982(9)	148(1)	358.1(7)	
			64.20(1)	3	63.695(7)	59(1)	15.4(2)	
Center II ($[AsO_2]^{2-}$)								
	1.9932(3)	-0.0014(1)	-0.0080(2)	1	2.0078(4)	30.1(7)	204(2)	
g		1.9977(1)	-0.0032(2)	2	1.9981(1)	87(1)	110(1)	
			2.0027(4)	3	1.9878(3)	120.0(7)	198(1)	
A(^{75}As)	-8.56(4)	-3.38(3)	1.05(4)	1	20.98(1)	80.9(1)	276.84(7)	0.257
(mT)		19.88(2)	-4.28(6)	2	-7.13(6)	161(1)	214(1)	
			-6.60(4)	3	-9.12(4)	106(1)	4.1(2)	

Experimental axes **x** and **z** are defined as parallel to the crystallographic axes **a** and **b**, respectively.

Table 5-4 Spin Hamiltonian parameters of $[AsO_3]^{2-}$ and $[AsO_2]^{2-}$ in crystalline hosts

Host	g_1	g_2	g_3	$A_1/g_e\beta_e$ (mT)	$A_2/g_e\beta_e$ (mT)	$A_3/g_e\beta_e$ (mT)	Ref
			$[AsO_3]^{2-}$				
newberyite	2.00533(5)	2.00124(5)	2.00029(5)	80.537(6)	63.982(9)	63.695(7)	TS
struvite (I)	2.00431(4)	2.00399(4)	2.00154(4)	72.950(6)	56.581(5)	56.576(5)	1
struvite (II)	2.00467(6)	2.00298(7)	2.00122(6)	76.457(9)	60.210(9)	60.059(9)	1
struvite (III)	2.00419(7)	2.0034(1)	2.00161(5)	74.620(6)	58.271(9)	58.172(9)	1
struvite (IV)	2.00349(6)	2.00322(6)	2.00110(6)	79.976(9)	62.975(6)	62.937(7)	1
struvite (V)	2.00330(8)	2.00287(9)	2.00104(8)	84.771(9)	67.64(1)	67.62(1)	1
boussingaultite	2.00603(4)	2.00538(4)	2.00218(4)	63.906(5)	49.391(5)	49.016(6)	1
calcite (77K)	2.00195(5)	2.00195(5)	2.00162(5)	93.73(1)	75.24(1)	75.24(1)	2
$Na_2HAsO_4{\cdot}7H_2O$	2.005(2)	2.005(2)	2.004(2)	72.5(1)	56.7(2)	56.7(1)	3
KH_2AsO_4 (K)	1.996(5)	1.996(5)	1.996(5)	91.8	75	74.2	4
KH_2AsO_4 (L)	1.999(5)	1.999(5)	1.999(5)	76.5	60.8	60.4	4
KH_2AsO_4 (M)	2.000(5)	2.000(5)	2.000(5)	66.1	50	49.6	4
KH_2PO_4 (b)	2.005(5)	2.005(5)	2.005(5)	75.6(5)	72.0(5)	72.0(5)	5
KH_2PO_4 (c)	2.005(5)	2.005(5)	2.005(5)	94.7(5)	88.3(5)	88.3(5)	5
betaine arsenate	2.001(4)	1.998(4)	1.998(4)	65.9(4)	51.6(4)	51.6(4)	6
haidingerite(I)	1.999	1.999	1.999	85.23	67.26	67.26	7
haidingerite(II)	1.998	1.993	1.993	94.03	75.63	75.63	7
gypsum	2.00537(4)	2.00371(5)	2.00134(3)	69.65(1)	53.26(1)	53.12(1)	8
danburite	2.00539(3)	2.00258(4)	2.00103(3)	85.852(3)	67.918(3)	67.514(3)	9
			$[AsO_2]^{2-}$				
newberyite	2.0078(4)	1.9981(1)	1.9878(3)	20.98(1)	-7.13(6)	-9.12(4)	TS
danburite (I)	1.99827(3)	1.99539(4)	1.97127(3)	26.148(7)	-9.78(1)	-10.69(1)	9
danburite (II)	1.99806(3)	1.99250(2)	1.97169(4)	26.540(7)	-10.929(7)	-11.625(7)	9
calcite	2.0150	1.9991	1.9910	21.89	–5.42	–6.17	10
$C_2H_6AsNaO_2$	2.012	1.995	1.967	18.31	–7.49	–8.49	11
boussingaultite	2.0115(1)	1.9996(1)	1.9946(1)	16.86(1)	-8.14(1)	-8.44(1)	1
gypsum	2.01484(2)	1.99962(2)	1.9958(1)	16.96(1)	-7.53(1)	-7.95(2)	8

Reference: TS is this study; 1, Lin et .al., (2013b); 2, Serway and Marshall, (1966); 3, Lin and McDowell, (1964); 4, Dalal et al., (1972); 5, Murty et al., (1977); 6, Pöppl et al., (1994); 7, Gilinskaya and Afanas'eva, (1981); 8, Lin et al., (2013a); 9, Li et al., (2013); 10, Marshall and Serway, (1969); 11, Geoffroy and Llinares, (1979).

Table 5-5 Selected bond distances and directions in newberyite

Bond	Distance (Å)	θ (°)	ϕ (°)
P-O1	1.497	61.6	52.2
P-O2	1.533	74.5	286.8
P-O3	1.529	81.8	174.6
P-O4	1.594	12.7	224.3
⊥(P-O1-O2)		39.8	182.7
⊥ (P-O1-O3)		36.7	275.8
⊥ (P-O1-O4)		88.4	321.4
⊥ (P-O2-O3)		17.5	57.2
⊥ (P-O2-O4)		78.5	19.2
⊥ (P-O3-O4)		80.0	83.2

Polar angle (θ) and azimuthal angle (ϕ) are relative to the crystallographic axes **b** and **a**, respectively.

$$[PO_4]^{3-} \rightarrow [AsO_3]^{3-} \quad (5\text{-}3)$$

$$[AsO_3]^{3-} \xrightarrow{hv} [AsO_2]^{2-} + O^{2-} + e^- \quad (5\text{-}4)$$

To the best of my knowledge, the single-crystal EPR detection of As^{3+} in synthetic newberyite is the first among phosphates. Previous studies of natural and synthetic phosphates reported only As^{5+}, including those using the highly-sensitive EPR technique (Zhu et al., 2009; Lee et al., 2009; Twidwell et al., 2005; Murty et al., 1977; Lin et al., 2013b). The presence of As^{3+} in this study using sodium hydrogen arsenate heptahydrate ($Na_2HAsO_4 \cdot 7H_2O$) in the starting material is similar to that in my previous syntheses of gypsum with a similar experimental setup and the same arsenic source. The presence of As^{3+} in these month-long open-tube experiments is probably attributable to either impurity or unknown reduction reactions related to biotic and abiotic processes (Lin et al., 2013a). The failure of detecting As^{3+} in synthetic newberyite by synchrotron XAS is attributable to the limitation of this technique, because the difference in the white line position between As^{3+} and As^{5+} in As K-edge XAS spectra is only ~3 eV, making detection of the subordinate As^{3+} species difficult (Li et al., 2013). The single-crystal EPR technique has a superior sensitivity than synchrotron XAS and can readily distinguish the various paramagnetic As-associated oxyradicals on the basis of diagnostic ^{75}As hyperfine coupling constants (Di Benedetto et al., 2011; Li et al., 2013; Lin et al., 2013a; Mao et al., 2010; Pan, 2013; Pan and Nilges, 2014).

5.3.4 Powder EPR spectra of synthetic and natural newberyite

Figure 5-7 compares the powder EPR spectra between synthetic and natural newberyite. The powder EPR spectrum of synthetic newberyite is dominated by Center I and is readily reproduced by spectral simulations using the spin Hamiltonian parameters obtained from the single-crystal EPR analysis (Table 5-3). Center II is not visible in the powder EPR spectrum of gamma-ray-irradiated synthetic newberyite due to interferences from the strong Mn^{2+} signals.

Powder EPR spectra of natural newberyite with and without gamma-ray irradiation are dominated by well-resolved Mn^{2+} and Fe^{3+} signals, without any evidence of As-associated oxyradicals. The Mn^{2+} center is readily identified by the characteristic ^{55}Mn hyperfine structure consisting of 6 approximately equal intensity lines at ~9 mT apart. The Fe^{3+} center is characterized by a broad signal at the effective g value of ~4.28 (Pan et al., 2009). The failure of detecting any As-associated oxyradicals in natural newberyite is attributable to 1) strong Mn^{2+} signals and 2) the presence of abundant transition metals (Table 5-1), which are deep electron trappers and probably inhibit the formation of paramagnetic As-associated oxyradicals from their diamagnetic precursors during gamma ray irradiation.

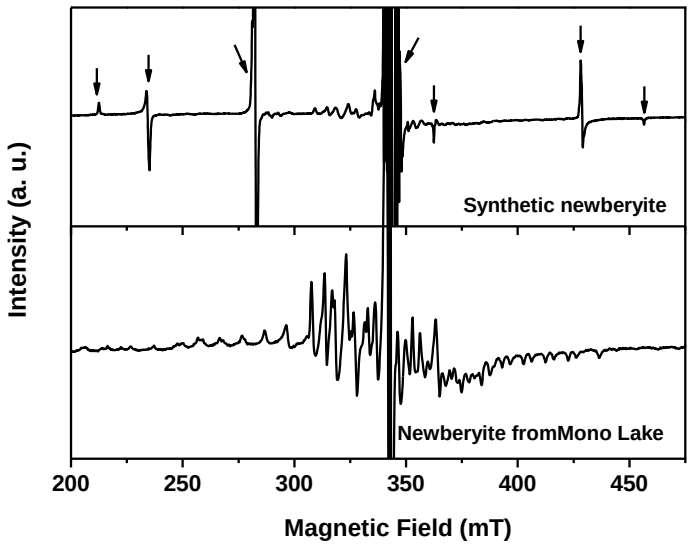

Figure 5-7. Powder EPR spectra of synthetic newberyite (upper trace) and natural newberyite from Paoha island, Mono Lake, California (lower trace).

5.3.5 Implications for green fertilizers

Guano deposits from the excrements of birds and cave-dwelling bats have been used as fertilizers since ancient times and are increasingly favored by organic farmers (Cushman, 2013). Arsenic as a natural element is known to become enriched in the food chain and is accumulated in guano deposits (O'Shea et al., 2001; Liu et al., 2013). For example, Xie and Sun (2008) reported penguin dropping sediments in Antarctic contain 12.41±0.45 ppm As, which is twice of the background sediment without any penguin dropping. These authors also noted that historical change in the As concentration in a 1,800-year record in lake sediments correlates with the fluctuation of penguin numbers. The As contents in newberyite from Skipton Caves are similar to those in bats' guano elsewhere (O'Shea et al., 2001), suggesting that As was retained during the transformation from struvite to newberyite. This finding is consistent with my experimental results that both struvite and newberyite are capable of sequestering significant amounts of As.

The elevated level of As in newberyite from Paoha island is undoubtedly related to the accumulation of this metalloid in the food chain (Bou-Olayan et al., 1995; Larsen et al., 1997; Raissy et al., 2012), because birds in the region are known to feed on brine shrimps in the As-rich Mono Lake (Oremland et al., 2004; Kulp et al., 2008; Wolfe-Simon et al., 2011). These results show that guano deposits, while natural, cannot be taken for granted when it comes to arsenic and other heavy metals and metalloids.

Guano fertilizers are limited in reserves, including most deposits located in ecological sensitive regions or highly regulated conservation areas, and therefore are unlikely to see significantly expanded exploitation in the future. Green fertilizers such as magnesium phosphates recovered from wastewaters, on the other hand, are expected to be increasingly important and have the potential to become dominant, while making wastewater treatments more sustainable. Similar to Lin et al. (2013b), this study shows that newberyite precipitated under ambient conditions is capable of accommodating significant levels of arsenic. These results raise a serious concern that magnesium phosphates recovered from wastewaters represent a potential source of arsenic contamination. This concern is particularly important considering the fact that elevated levels of arsenic have been documented in wastewaters around the world (Buj et al., 2009; Kern et al., 2008; Ronteltap et al., 2007), especially in places where the long-standing practice of

arsenic additives to chicken and swine feeds remains.

My previous discovery of an exclusive incorporation of As^{5+} in struvite led us to propose its precipitation from wastewaters under reduced conditions to minimize As uptake. The fact that newberyite is capable of sequestering As^{3+} makes this proposal less effective if newberyite and struvite co-precipitates. Previous experimental studies showed that struvite in the $MgCl_2$–$NH_4H_2PO_4$–NaOH–H_2O system is stable over a wide compositional range, whereas newberyite is restricted to high Mg (Babić-Ivančić et al., 2006) and low pH conditions (Kontrec et al., 2005). Therefore, careful control of appropriate Mg concentrations and approximately neutral pH as well as reducing conditions is a possible route to maximize the precipitation of struvite with minimal arsenic uptake.

The decomposition of struvite to newberyite (Cohen and Ribbe, 1966; Whtaker, 1968, 1969; Boistelle et al., 1983; Babić-Ivančić et al., 2002, 2004, 2006; Rouff, 2013) most likely occurs when green fertilizers are applied to soils as well. Therefore, my data on arsenic in newberyite also provide insights into the fate of arsenic in soils. The apparent accommodation and retention of arsenic in both synthetic and natural newberyite suggest that no negative impact, albeit temporary, during the initial decomposition of struvite. However, complete dissolution of struvite and newberyite from green fertilizers, if they contain arsenic, will contribute to arsenic contamination over time. Therefore, processes for removal of arsenic (other heavy metals and metalloids as well) from wastewaters must be developed before phosphate recovery for manufacturing green fertilizers.

Finally, the capacity of newberyite for accommodating significant amounts of arsenic in its lattice (i.e., 1099 ppm As vs 241 ppm As in struvite under similar conditions) coupled with its simple chemistry and ready formation under ambient conditions makes it a highly attractive material for the immobilization and removal of arsenic contamination in aqueous environments. Another advantage of newberyite over other phosphates is its apparent uptake of both As^{5+} and As^{3+}, although the latter, detected only by single-crystal EPR, is low. Moreover, the stability of newberyite at low pH values (Kontrec et al., 2005) makes it particularly useful under acidic conditions.

5.4 References

Abbona, F., Boistelle, R., and Haser, R. (1979) Hydrogen bonding in $MgHPO_4.3H_2O$ (newberyite). *Acta Crystallographica Section B: Structural Crystallography and Crystal Chemistry* **35**, 2514-2518.

Abbona, F., Lundager Madsen, H. E., and Boistelle, R. (1982) Crystallization of two magnesium phosphates, struvite and newberyite: Effect of pH and concentration. *Journal of Crystal Growth* **57**, 6-14.

Ali, M. I. (2005) Struvite crystallization from nutrient rich wastewater. *Struvite crystallization from nutrient rich wastewater. PhD thesis, James Cook University*.

Babić-Ivančić, V., Kontrec, J., and Brečević, L. (2004) Formation and transformation of struvite and newberyite in aqueous solutions under conditions similar to physiological. *Urol Res* **32**, 350-356.

Babić-Ivančić, V., Kontrec, J., Kralj, D., and Brečević, L. (2002) Precipitation diagrams of struvite and dissolution kinetics of different struvite morphologies. *Croatica Chemica Acta*, **75**, 89-106.

Babić-Ivančić, V., Kontrec, J., Brečević, L., and Kralj, D. (2006) Kinetics of struvite to newberyite transformation in the precipitation system $MgCl_2$–$NH_4H_2PO_4$–NaOH–H_2O. *Water Research* **40**, 3447-3455.

Bartl, H., Catti, M., Joswig, W., and Ferraris, G. (1983) Investigation of the crystal structure of newberyite, $MgHPO_4 \cdot 3H_2O$, by single crystal neutron diffraction. *TMPM Tschermaks Petr. Mitt.* **32**, 187-194.

Bhuiyan, M. I. H., Mavinic1, D. S., and Koch, F. A. (2008) Phosphorus recovery from wastewater through struvite formation in fluidized bed reactors: a sustainable approach. *Water Science and Technology* **57**, 175-181.

Boistelle, R., Abbona, F., and Lundager Madsen, H. E. (1983) On the transformation of struvite into newberyite in aqueous systems. *Phys Chem Minerals* **9**, 216-222.

Bou-Olayan, A. H., Al-Yakoob, S., and Al-Hossaini, M. (1995) Arsenic in shrimp from Kuwait. *Bull. Environ. Contam. Toxicol*. **54**, 584-590.

Bridge, P. J. (1971). Analyses of altered struvite from Skipton, Victoria. *Mineralogical Magazine* **38**, 381-382.

Buj, I., Torras, J., Casellas, D., Rovira, M., and de Pablo, J. (2009) Effect of heavy metals and water content on the strength of magnesium phosphate cements. *Journal of Hazardous Materials* **170**, 345-350.

Cordell, D., Drangert, J.-O., and White, S. (2009) The story of phosphorus: Global food security and food for thought. *Global Environmental Change* **19**, 292-305.

Cohen, L. H. and Ribbe, P. H. (1966) Magnesium phosphate mineral replacement at Mono Lake, California. *American Mineralogist* **51**, 1755–1765.

Cushman, Gregory T. (2013). *Guano and the Opening of the Pacific World: A Global Ecological History*. Cambridge and New York: Cambridge Univ. Press

Dalal, N. S., Dickson, J. R., McDowell, C. A. (1972) Electron paramagnetic resonance studies of X-irradiated KH_2AsO_4, KD_2AsO_4, RbH_2AsO_4, RbD_2AsO_4, CsH_2AsO_4, $NH_4H_2AsO_4$, and $ND_4D_2AsO_4$ (ferroelectrics and antiferroelectrics). *Journal of Chemical Physics*, **57 (10)**, 4254-4265.

Di Benedetto, F., Pelo, S. D., Caneschi, A., and Lattanzi, P. (2011). Chemical state of arsenic and copper in enargite: evidences from EPR and X-ray absorption spectroscopies, and SQUID magnetometry. *Neues Jahrbuch für Mineralogie - Abhandlungen* **188**, 11-19.

Foster, A. L., Brown, G. E., Tingle, T. N., and Parks, G. A. (1998) Quantitative arsenic speciation in mine tailings using X-ray absorption spectroscopy. *American Mineralogist* **83**.

Frost, R. L., Palmer, S. J., and Pogson, R. E. (2012) Thermal Stability of newberyite $Mg(PO_3OH)\cdot 3H_2O$ A cave mineral from Skipton Lava Tubes, Victoria, Australia. *Journal of Thermal Analysis and Calorimetry* **107**, 1143-1146.

Geoffroy M. and Llinares A. (1979) Etude par resonance paramagnétique électronique des radicaux piégés dans un monocristal de diméthylarsinate de sodium irradié aux rayons X. *Helvetica Chimica Acta* **62**, 1605-1613.

Gilinskaya, L. G., Afanas'eva, V. I. (1981) Two forms of the AsO_3^{2-} radical in γ-irradiated heidingerite $CaHAsO_4\cdot H_2O$. *Journal of Structural Chemistry* **22 (4)**, 640-642.

Isherwood, K. F. (2000) Mineral fertilizer use and the environment. *International Fertilizer Industry Association/United Nations Environment Programme, Paris*.

Jaffer, Y., Clark, T. A., Pearce, P., and Parsons, S. A. (2002). Potential phosphorus recovery by struvite formation. *Water Research* **36**, 1834-1842.

Jiang, D. T., Chen, N., Demopoulos, G. P., and Rowson, J. W. (2010). Response to the comment

by D. Paktunc on "Structural characterization of poorly-crystalline scorodite, Iron(III)–arsenate co-precipitates and uranium mill neutralized raffinate solids using X-ray absorption fine structure spectroscopy". *Geochimica et Cosmochimica Acta* **74**, 4597 - 4602.

Kern, J., Heinzmann, B., Markus, B., Kaufmann, A. C., Soethe, N., and Engels, C. (2008) Recycling and assessment of struvite phosphorus from sewage sludge. *Agricultural Engineering International: the CIGR Ejournal.* **10**.

Kim, E., Chen, N., Arthur, Z., Warner, J., Demopoulos, G. P., Rowson, J. W., and Jiang, D. T. (2013) Multiple scattering Debye-Waller factors for arsenate. *Journal of Physics: Conference Series* **430**.

Kitahama, K., Kiriyama, R., and Yoshihisa, B. (1975) Refinement of the crystal structure of scorodite. *Acta Crystallographica, Section B* , **31**, 322-324.

Kontrec, J., Babić-Ivančić, V., and Brečević, L. (2005) Formation and Morphology of Struvite and Newberyite in Aqueous Solutions at 25 and 37 °C. *Collegium Antropologicum* **29**, 289-294.

Kulp, T. R., Hoeft, S. E., Asao, M., Madigan, M. T., Hollibaugh, J. T., Fisher, J. C., Stolz, J. F., Culbertson, C. W., Miller, L. G., and Oremland, R. S. (2008) Arsenic(III) Fuels anoxygenic photosynthesis in hot spring biofilms from Mono Lake, California. *Science* **321**, 967-970.

Larsen, E. H., Quétel, C. R., Munoz, R., Fiala-Medioni, A., and Donard, O. F. X. (1997). Arsenic speciation in shrimp and mussel from the Mid-Atlantic hydrothermal vents. *Marine Chemistry* **57**, 341-346.

Le Corre, K. S., Valsami-Jones, E., Hobbs, P., and Parsons, S. A. (2009) Phosphorus recovery from wastewater by struvite crystallization: A review. *Critical Reviews in Environmental Science and Technology* **39**, 433-477.

Lee, Y. J., Stephens, P. W., Tang, Y., Li, W., Phillips, B. L., Parise, J. B., and Reeder, R. J. (2009) Arsenate substitution in hydroxylapatite: Structural characterization of the $Ca5(P_xAs_{1-x}O_4)_3OH$ solid solution *American Mineralogist* **94**, 666-675.

Li, R., Lin, J., Nilges, M. J., Chen, N., and Pan, Y. (2013). Arsenic speciation in danburite ($CaB_2Si_2O_8$): A synchrotron XAS and single-crystal EPR study. *European Journal of Mineralogy* (in press).

Lin, J., Chen, N., Nilges, M. J., and Pan, Y. (2013a) Arsenic speciation in synthetic gypsum ($CaSO_4 \cdot 2H_2O$): A synchrotron XAS, single-crystal EPR, and pulsed ENDOR study. *Geochimica et Cosmochimica Acta* **106**, 524-540.

Lin, J., Chen, N. and Pan, Y. (2013b) Arsenic incorporation in synthetic struvite ($NH_4MgPO_4 \cdot 6H_2O$): A synchrotron XAS and single-crystal EPR study. *Environmental Science & Technology* **47 (22)**, 12728-12735.

Lin W. C. and McDowell C. A. (1964) Electron spin resonance of an X-ray irradiated single crystal of disodium hydrogen arsenate, $Na_2HAsO_4 \cdot 7H_2O$. *Molecular Physics* **7**, 223-234.

Liu, X., Nie, Y., Sun, L., and Emslie, S. D. (2013) Eco-environmental implications of elemental and carbon isotope distributions in ornithogenic sediments from the Ross Sea region, Antarctica. *Geochimica et Cosmochimica Acta* **117**, 99-114.

Mao, M., Lin, J., and Pan, Y. (2010). Hemimorphite as a natural sink for arsenic in zinc deposits and related mine tailings: Evidence from single-crystal EPR spectroscopy and hydrothermal synthesis. *Geochimica et Cosmochimica Acta* **74**, 2943-2956.

Marshall S. A. and Serway R. A. (1969) Electron spin resonance absorption spectrum of the AsO molecule-ion in γ-irradiated single-crystal calcite. *Journal of Chemical Physics* **50**, 435-439.

Moldovan, B. J., Jiang, D. T. and Hendry, M. J. (2003) Mineralogical characterization of arsenic in uranium mine tailings precipitated from iron-rich hydrometallurgical solutions. *Environmental Science & Technology* **37**, 873-879.

Murty, P. N., Murty, C. R. K. and Subramanian, S. (1977). Electron paramagnetic resonance study of X-irradiated arsenate-doped phosphate: KH_2AsO_4/KH_2PO_4. *Physica Status Solidi (a)* **39**, 675-682.

Muster, T. H., Douglas, G. B., Sherman, N., Seeber, A., Wright, N. and Güzükara, Y. (2013) Towards effective phosphorus recycling from wastewater: Quantity and quality. *Chemosphere* **91**, 676-684.

Ollier, C. D. (1963). The Skipton lava caves. *Victoria Naturalist* **80**, 181-183.

Oremland, R. S., Stolz, J. F., and Hollibaugh, J. T. (2004) The microbial arsenic cycle in Mono Lake, California. *FEMS Microbiology Ecology* **48**, 15-27.

O'Shea, T. J., Everette, A. L., and Ellison, L. E. (2001) Cyclodiene insecticide, DDE, DDT, arsenic, and mercury contamination of big brown bats (Eptesicus fuscus) foraging at a

Colorado Superfund site. *Archives of Environmental Contamination and Toxicology* **40**, 112-120.

Pan, Y. (2013) Arsenic speciation in rock-forming minerals determined by EPR spectroscopy. In *Arsenic: Sources, Environmental Impacts, Toxicity and Human Health: A Medical Geology Perspective*; Masotti, A., Ed.; Nova Science Publishers Inc, 39-52.

Pan, Y. and Nilges, M.J. (2014) Electron paramagnetic resonance spectroscopy: Basic principles, experimental techniques and applications to Earth and planetary sciences. *Reviews in Mineralogy and Geochemistry* **78** (in press).

Pan, Y., Mao, M. and Lin, J. (2009) Single-crystal EPR study of Fe^{3+} and VO^{2+} in prehnite from the Jeffrey mine, Asbestos, Quebec. *Canadian Mineralogist* **47**,933-945.

Pöppl, A; Tober, O., Völkelel, G. (1994) ESR study of the AsO_3^{2-} radical in γ-irradiated betaine arsenate. *Physica Status Solidi B* **183**, K63-K66.

Raissy, M., Rahimi, E., Nadeali, V., Ansari, M., and Shakerian, A. (2012). Mercury and arsenic in green tiger shrimp from the Persian Gulf. *Toxicology and Industrial Health*.

Rehr, J. J. and Albers, R. C. (2000) Theoretical approaches to x-ray absorption fine structure. *Reviews of Modern Physics* **72**, 621-654.

Ressler, T. (1997) WinXAS: A new software package not only for the analysis of energy-dispersive XAS data. *Journal de Physique IV* **7**, 269-270.

Ronteltap, M., Maurer, M., and Gujer, W. (2007) The behaviour of pharmaceuticals and heavy metals during struvite precipitation in urine. *Water Research* **41**, 1859-1868.

Rouff, A. A. (2013) Temperature-dependent phosphorus precipitation and chromium removal from struvite-saturated solutions. *Journal of Colloid and Interface Science*, **392**, 343-348.

Runge-Metzger, A. (1995) Closing the cycle: obstacles to efficient P management for improved global food security. *SCOPE 54 - Phosphorus in the Global Environment - Transfers, Cycles and Management.*

Sartorius, C., von Horn, J., and Tettenborn, F. (2011) Phosphorus recovery from wastewater - state-of-the-art and future potential. *Conference Nutirent recovery and management, International Water Association (IWA), January 9-12, 2011, Miami, Florida, USA.*

Serway R. A. and Marshall S. A. (1966) Electron spin resonance absorption spectrum of the AsO_3^{2-} molecule ion in γ–irradiated single–crystal calcite. *Journal of Chemical Physics* **45 (6)**, 2309-2314.

Shu, L., Schneider, P., Jegatheesan, V., and Johnson, J. (2006) An economic evaluation of phosphorus recovery as struvite from digester supernatant. *Bioresource Technology* **97**, 2211-2216.

Smil, V. (2000) Phosphorus in the environment: natural flows and human Interferences. *Annual Review of Energy and the Environment* **25**, 53-88.

Steen, I. (1998) Phosphorus availability in the 21st Century: management of a non-renewable resource. *Phosphorus and Potassium* **217**, 25-31.

Twidwell, L. G., Mccloskey, J., Lee, M. G., and Saran, J. (2005). Arsenic removal from mine and process waters by lime/phosphate precipitation. *The Minerals, Metals & Materials Society*.

Valsami-Jones, E. (2004) Phosphorus in environmental technologies: principles and applications.

Xie Z. and Sun L. (2008) A 1,800-year record of arsenic concentration in the penguin dropping sediment, Antacrctic. *Environmental Geology* 55, 1055-1059.

Whtaker, A. (1968) The decomposition of struvite. *Mineralogical Magazine* **36**, 820-824.

Whtaker, A. (1969) The decomposition of struvite: further evidence *Mineralogical Magazine* **37**, 290-291.

Williams Jr, J. C., Sacks, A. J., Englert, K., Deal, R., Farmer, T. L., Jackson, M. E., Lingeman, J. E., and McAteer, J. A. (2012) Stability of the infection marker struvite in urinary stone samples. *Journal of Endourology* **26**, 726-731.

Wolfe-Simon, F., Blum, J. S., Kulp, T. R., Gordon, G. W., Hoeft, S. E., Pett-Ridge, J., Stolz, J. F., Webb, S. M., Weber, P. K., Davies, P. C. W., Anbar, A. D., and Oremland, R. S. (2011) A bacterium that can grow by using arsenic instead of phosphorus. *Science* **332**, 1163-1166.

Zhu, Y., Zhang, X., Long, F., Liu, H., Qian, M., and He, N. (2009). Synthesis and characterization of arsenate/phosphate hydroxyapatite solid solution. *Materials Letters* **63**, 1185-1188.

CHAPTER 6

Conclusions and directions for future research

This thesis reports on results of arsenic uptake and speciation in gypsum, struvite and newberyite, with direct relevance to understanding and remediation of arsenic contamination in aqueous environments. Major findings from the present thesis research can be summarized as follows. Also discussed in this chapter are potential areas for future research:

Synchrotron XAS and single-crystal EPR results reveal that both As^{5+} and As^{3+} occupy the S site in the gypsum structure. Results from experiments with pH values from 2 to 14 show that uptake of arsenic in gypsum is pH dependent. At low pH values, substitution is dominant, whereas at high pH values, sorption might be dominant. This result is particularly important with respect to not only the application of gypsum for remediation of arsenic contamination in aqueous environment but also the design of milling processes for optimal crystallization of gypsum with the maximal uptake of arsenic in its crystal lattice. Further research in this area may include detailed dissolution experiments to determine the solubility of arsenic-doped gypsum (i.e., for comparison available data of pure gypsum) and the rate of arsenic release from gypsum in various waters.

The discovery of As^{3+} substituting for S^{5+} extends my knowledge of arsenic in sulfates. Thus, sulfates such as jarosite and alunite are potentially useful to immobilize As^{3+} in aqueous systems. Future research on As^{3+} co-precipitation in jarosite and alunite can be made to evaluate the immobilization and removal of arsenic contamination in aqueous environments, especially those associated with mining and milling activities.

The reasons for the conversions between As^{5+} and As^{3+} in the double diffusion gel experiments remain unclear and require further research. First, high purity starting materials are highly recommended to avoid mixed As^{5+} and As^{3+} and transition metal impurities. Second, experiments with sterilized starting materials under abiotic conditions can be taken for comparison with existing data to evaluate the possibility of bacterial activity in the conversions between As^{5+} and As^{3+} in the double diffusion gel experiments.

Other areas of further research on arsenic in gypsum may include natural samples from lakes and mine tailings. Admittedly, experiments conducted in the present thesis research are simple and, therefore, are not directly applicable to the more complex natural environments. Data from natural samples can first be compared with results of the present thesis study. This exercise may point out additional factors that control on the uptake and speciation of arsenic in gypsum in various natural and man-made environments.

Results from synchrotron As K-edge XANES spectra and single-crystal electron paramagnetic resonance (EPR) spectra show the replacement of As^{5+} for P^{5+} in synthetic struvite. In particular, five $[AsO_3]^{2-}$ radicals and one $[AsO_4]^{2-}$ radical are found in the single-crystal electron paramagnetic resonance (EPR) spectra, all of which formed from the diamagnetic $[AsO_4]^{3-}$ precursor during gamma-ray irradiation. However, the pH range of the experiments conducted in this thesis is limited due to the synthesis method used. Further research on the effect of pH on the uptake of arsenic in struvite is interesting. In particular, further experiments on the stability of struvite at pH from 12 to 14 may provide a useful technique for the immobilization and removal of arsenic under ultra-alkaline conditions. Also, dissolution experiments of arsenic doped struvite can be made to determine its solubility (i.e., for comparison with pure struvite) and assess the rate of arsenic release, directly relevant to struvite recovered from wastewaters a fertilizer.

X-ray absorption spectra of arsenic doped newberyite ($MgHPO_4 \cdot 3H_2O$) suggest that As^{5+} is the dominant oxidation state. However, single-crystal EPR spectra of gamma-ray-irradiated newberyite contain two types of arsenic-associated oxyradicals: $[AsO_3]^{2-}$ and $[AsO_2]^{2-}$ from the substitution of As^{5+} and As^{3+} for P^{5+}, respectively. The EPR detection of As^{3+} in synthetic newberyite is the first among phosphate minerals and can be confirmed by additional synthesis experiments. Similar to the gypsum study in Chapter 3, synthesis experiments with As^{3+} in the starting material can be made. A more pronounced $[AsO_2]^{2-}$ radical in the resulting EPR spectra would be another line of compelling evidence for As^{3+} in newberyite. Also, the presence of As^{3+} in synthetic newberyite may be evaluated by other analytical techniques such as atomic fluorescence spectroscopy.

Struvite and newberyite can both sequester significant amounts of arsenic and, therefore, as increasingly important green fertilizers represent a significant source of contamination, if

recovered from wastewaters with removal of arsenic. Further research is needed to develop effective processes to minimize arsenic (and other heavy metals and metalloids) in green fertilizers such as struvite and newberyite recovered from wastewaters. The fact that newberyite is a common decomposition product of struvite makes data on arsenic speciation important in understanding the mobility and fate of arsenic in the former when it is used a fertilizer. In this context, systematic experiments to investigate the behavior of arsenic during the transformation from struvite to newberyite in both laboratory and “natural" environments are interesting. Another area for further research is that newberyite may be a useful material for the retention and removal of arsenic under acidic and ultra-acidic conditions.

APPENDIX

All thesis data (PXRD, EPR, SEM, ICPMS and synchrotron XRF and XAFS) as well as data analyses (input and output files) have been compiled in electronic formats in two CDs, which are available upon request from me (Jinru Lin) or Professor Yuanming Pan.